Alma Mater Studiorum · University of Bologna

School of Science
Department of Physics and Astronomy
Master Degree in Physics

Electromagnetic shower identification in the SAND Calorimeter of the DUNE Near Detector

Supervisor:

Dr. Gabriele Sirri

Submitted by:

Irene Cagnoli

Co-supervisors:

Dr. Matteo Tenti
Dr. Francesco Poppi

Academic Year 2020/2021

Abstract

The Deep Underground Neutrino Experiment (DUNE) is a next generation, long-baseline accelerator experiment designed to significantly contribute to the study of neutrino oscillations with unprecedented level of sensitivity. It envisages to observe neutrinos from a high intensity wide-band neutrino beam with a Near Detector (ND) system at the Fermi National Accelerator Laboratory and a Far Detector (FD) at $\sim$ 1300 km from the beam source at Sanford Laboratory, in South Dakota. The System for on-Axis Neutrino Detection (SAND) is one of the three detectors of the ND complex which provides continuous on-axis beam monitoring and performs various physics measurements.

This work concerns a study on the electromagnetic calorimeter (ECAL) capabilities of the SAND detector to perform electromagnetic showers and muon tracks discrimination. In particular, a new clustering algorithm to reconstruct events in the ECAL not exploiting at all Monte Carlo truth has been developed and studied for the first time. A multivariate analysis, based on machine-learning techniques, has been implemented to perform a classification of the clusters reconstructed by the clustering algorithm and study the capabilities in electromagnetic showers and muon tracks discrimination. The classification analysis is operated in two separated steps: (a) the multivariate methods are trained and validated using a dedicated dataset obtained by simulating particle guns of electrons and muons originated close to the ECAL; (b) the selected optimal classifiers are tested with simulated neutrino interactions in the SAND detector considering the case of a ν_μ-dominated beam in neutrino mode. Finally, the calorimeter performance in discriminating electromagnetic showers from muons is preliminary evaluated in terms of the product of efficiency times the signal purity.

Contents

Introduction **2**

1 Neutrino Physics **4**
- 1.1 Neutrinos in the Standard Model . . . 4
- 1.2 Neutrino mass . . . 8
- 1.3 Neutrino mixing and oscillation . . . 13
  - 1.3.1 Oscillation in vacuum . . . 13
  - 1.3.2 Oscillation in matter . . . 17
  - 1.3.3 Neutrino oscillation experiments . . . 19
- 1.4 Open questions of neutrino physics . . . 29

2 Dune Experiment **30**
- 2.1 The LBNF neutrino beam . . . 32
- 2.2 The Far Detector . . . 34
  - 2.2.1 The FD design . . . 34
  - 2.2.2 FD simulation and expected event rate . . . 39
  - 2.2.3 DUNE Prototypes . . . 41
- 2.3 The Near Detector . . . 42
  - 2.3.1 The need for the ND . . . 43
  - 2.3.2 The requirements for the ND and the physics program . . . 44
  - 2.3.3 The ND design . . . 48
- 2.4 Primary goals of the DUNE experiment . . . 50
  - 2.4.1 Standard neutrino oscillation physics program . . . 50
  - 2.4.2 Search for proton decay . . . 54
  - 2.4.3 Supernova neutrino bursts . . . 56

3 System for on-Axis Neutrino Detection **58**
- 3.1 The superconductive magnet . . . 59
- 3.2 The electromagnetic calorimeter . . . 59
  - 3.2.1 Reconstruction of time, position and energy . . . 63
- 3.3 The tracking system . . . 64

3.4 The active liquid argon target 68
3.5 Physics program 69

4 Event Reconstruction in the calorimeter and e.m. shower identification 73

4.1 Event simulation chain 73
    4.1.1 Digitization 76
    4.1.2 Event reconstruction using Monte Carlo truth information . 79
4.2 A new ECAL cluster reconstruction 82
4.3 Track/shower discrimination 85
    4.3.1 Training with dedicated particle beams 85
    4.3.2 Application to neutrino interactions 91

Conclusions 101

Bibliography 104

Introduction

This master thesis aims to study the performances of the electromagnetic calorimeter of the SAND apparatus in the DUNE Near Detector complex for the reconstruction of neutrino interaction events. In particular, this work focuses on the capabilities of the SAND calorimeter in electromagnetic shower identification.

Neutrino physics, introduced in chap.(1), is of central importance in modern physics considering that precision measurements of the parameters that rule the neutrino oscillations can help answering some pending questions about their nature and pave the way for new physics.

DUNE is a neutrino oscillation long-baseline accelerator experiment with the main purpose of measuring the CP violation term in the lepton sector and determining the neutrino mass ordering. A dedicated description on the design and scientific goals of the experiment is reported in chap.(2). DUNE will consist of two-sites neutrino detectors exposed to an intense neutrino beam: the Near Detector (ND) installed at Fermilab and the Far Detector (FD) located at Sanford Lab in South Dakota, at a distance of ∼1300 km from the neutrino beam source. The FD will consist of four modular, Liquid Argon Time-Projection Chambers with a total fiducial mass of roughly 40 kt. The FD will allow to measure the oscillated neutrino flux by detecting and reconstructing neutrino interactions over a wide range of energies. The ND will serve to measure and monitor the unoscillated beam and constrain systematic uncertainties [1].

The ND complex consists of three detectors: i) a Liquid Argon Time Projection Chamber (ND-LAr), ii) a magnetized Gas Argon Time Projection Chamber (ND-GAr), iii) the System for on-Axis Neutrino Detection (SAND). SAND is the only component permanently on the beam axis. As such it is a crucial component of the ND complex capable to monitor the beam changes with the required sensitivity, constrain systematics, and provide a rich neutrino physics program. The ND-LAr and ND-GAr are moved sideways 50% of the time to perform off-axis measurements.

The SAND detector, described in detail in chap.(3), is largely based on the reuse of the electromagnetic calorimeter (ECAL) and of the superconducting magnet from the KLOE experiment. The ECAL is a sampling calorimeter, made of lead layers and scintillating fibers, with a coverage of $\sim 98\%$ of 4π. The overall calorimeter is composed of a barrel and two endcaps divided into modules, 88 in total, for a total of 2440 segments (*cells*) read out at each side by photo sensors [2]. The SAND inner magnetic volume will contain a target/tracking system based on straw tube planes interleaved with thin carbon and hydrocarbon targets. An active LAr target in upstream position inside the magnetic volume is also foreseen. The study of neutrino interactions in Ar will contribute to constrain the systematic uncertainty in the oscillation data analysis [3].

In this work, neutrino interactions have been generated using GENIE [4]. The geometry of SAND has been implemented using the official DUNE *dunendggd* package [5]. The particle propagation and the related detector response are simulated using the *edep-sim* package [6].

A new clustering algorithm has been implemented for the SAND calorimeter, inspired to the reconstruction procedure already implemented in KLOE but adapted to the SAND framework. The clustering algorithm is used to group neighboring hit cells into clusters that are associated to a track or a shower. Clusters merging and splitting operations are also applied to improve the performances of the algorithm. The energy associated to a cluster is obtained by the sum of the energies from all contributing cells. The cluster position and time are determined as energy weighted averages over the cluster cells.

The validation of the clustering algorithm is operated in two steps. Firstly, test simulations are performed based on particle guns of electrons or muons, placed just in front of the calorimeter at a fixed direction. A multivariate analysis is performed to discriminate the signal and background samples, also using machine-learning techniques like Neural Networks and Boosted Decision Trees. The classification performances are evaluated in terms of background (muons) rejection power and signal (e.m. showers) efficiency.

The clustering algorithm is then applied to reconstruct tracks and e.m. showers from neutrino interactions. The performance for electromagnetic shower identification is evaluated in terms of the product between purity and signal efficiency.

The overview of the software tools used for simulations and the description of the analysis performed for this thesis are reported in chap.(4).

To summarize, in this work a new clustering algorithm for the SAND electromagnetic calorimeter is developed and implemented, a multivariate analysis based on machine-learning techniques is implemented and the performance for electron shower identification is evaluated.

Chapter 1

Neutrino Physics

1.1 Neutrinos in the Standard Model

The Standard Model (SM) is a gauge theory based on the local symmetry group $SU(3)_C \times SU(2)_L \times U(1)_Y$ which describes the electromagnetic, weak and strong interactions in the framework of quantum field theory. Where C denotes color, L stand for left-handed chirality and Y for weak hypercharge.

The particle content of the SM includes the spin-$\frac{1}{2}$ quarks and leptons, spin-1 gauge bosons and spin-0 Higgs boson. Among these, the neutrino particles are electrically neutral and colourless fermions which interact only via weak and gravitational interactions. Three neutrino flavors exist in nature (ν_e, ν_μ, ν_τ) and they are distinguished by the flavor of charged lepton to which they couple.

In the SM, neutrinos are seen as massless particles interacting with matter only via the exchange of the heavy virtual $W^\pm$ and Z bosons. The $W^\pm$ bosons mediate the Charged Current (CC) interactions and the Z boson is responsible for the neutral current (NC) interactions.

The Lagrangian that determines neutrino interactions is the electroweak part of the SM Lagrangian. Hence, to study these elusive particles it is sufficient to consider only the $SU(2)_L \times U(1)_Y$ part of the SM symmetry group. This can be possible since the symmetry under the color group $SU(3)_C$ is unbroken and there is no mixing between the $SU(3)_C$ and $SU(2)_L \times U(1)_Y$ sectors.

Before analyzing the electroweak Lagrangian, it should be considered that in the SM the neutrinos are theorized to be massless. This assumption was inferred from the fact that the mass eigenstates couldn't be resolved experimentally and in the past there was no indication of the existence of neutrino mass. This hypothesis was consistent with the evidence [7] that neutrinos produced in CC interactions are fully left-handed polarized, while antineutrinos are found to be fully right-handed polarized [8, 9]. For this reason, in the SM, neutrino fields have only the left-handed components and the antineutrino fields have only the right-handed components. In fact, the Dirac equation for a fermion field ψ can be equivalently expressed in Weyl components by two coupled equations of motions

$$i\gamma^\mu \partial_\mu \psi_L = m\psi_R, \tag{1.1.1}$$

$$i\gamma^\mu \partial_\mu \psi_R = m\psi_L, \tag{1.1.2}$$

since any fermion field ψ can be represented in the form of the sum of chiral left-handed and chiral right-handed components, i.e.

$$\psi = \psi_L + \psi_R = \frac{1-\gamma^5}{2}\psi + \frac{1+\gamma^5}{2}\psi. \tag{1.1.3}$$

In the massless case, the two eq.(1.1.1) and eq.(1.1.2) decouple and the massless fermion can be described by a two-component Weyl spinor. Therefore, the neutrino is always left-handed, the antineutrino is always right handed and they are distinct and independent from each other.

In the electroweak theory the left-handed and right-handed fermions transform differently under SU(2) group transformations. Thus, to study the electroweak Lagrangian of leptons the left-handed chiral components of the fermion fields are grouped into weak isospin doublets.

$$L_e = \begin{pmatrix} \nu_{eL} \\ e_L \end{pmatrix} \quad L_\mu = \begin{pmatrix} \nu_{\mu L} \\ \mu_L \end{pmatrix} \quad L_\tau = \begin{pmatrix} \nu_{\tau L} \\ \tau_L \end{pmatrix}. \tag{1.1.4}$$

While, the right-handed components of the lepton fields are

$$R_e = e_R \quad R_\mu = \mu_R \quad R_\tau = \tau_R, \tag{1.1.5}$$

which are assumed to be weak isospin singlets. By the Gell-Mann-Nishijima relation

$$\mathcal{Q} = I_3 + \frac{1}{2}Y, \tag{1.1.6}$$

where I_3 is the third component of the weak isospin, the weak hypercharges of the left-handed and right-handed components are

$$\begin{aligned} Y_L &= -1, \\ Y_R &= -2. \end{aligned} \tag{1.1.7}$$

According to the gauge invariance principle, in the SM Lagrangian, all terms respect the local symmetry. To have local gauge invariance under $SU(2)_L \times U(1)_Y$ transformations, it is necessary to introduce the gauge covariant derivative D_μ, defined as

$$D_\mu = \partial_\mu + ig\boldsymbol{b}_\mu \cdot \boldsymbol{I} + \frac{1}{2}ig' A_\mu Y\ ; \tag{1.1.8}$$

where g is the coupling constant and $\boldsymbol{b}^\mu = (b_1^\mu, b_2^\mu, b_3^\mu)$ are the three gauge boson fields associated with the three weak isospin generators $\boldsymbol{I} = (I_1, I_2, I_3)$ of the $SU(2)_L$ group. While, g' is the coupling constant and A^μ the gauge boson field associated with the hypercharge generator Y of the $U(1)_Y$ group. The covariant derivatives of the fields become

$$\big(\partial_\mu + ig\boldsymbol{b}_\mu \cdot \boldsymbol{I} + \frac{1}{2}ig' A_\mu Y\big) L_\alpha \quad \alpha = e, \mu, \tau; \tag{1.1.9}$$

$$\big(\partial_\mu + \frac{1}{2}ig' A_\mu Y\big) R_\alpha \quad \alpha = e, \mu, \tau. \tag{1.1.10}$$

Then, the Lagrangian which describes the kinetic terms for the fermion fields and the interactions between the fermionic and the gauge fields can be written as

$$\mathcal{L}_{lep} = \sum_{\alpha=e,\mu,\tau} \overline{R}_\alpha i\gamma^\mu \big(\partial_\mu + \frac{1}{2}ig' A_\mu Y\big) R_\alpha + \sum_{\alpha=e,\mu,\tau} \overline{L}_\alpha i\gamma^\mu \big(\partial_\mu + ig\boldsymbol{b}_\mu \cdot \boldsymbol{I} + \frac{1}{2}ig' A_\mu Y\big) L_\alpha \tag{1.1.11}$$

The kinetic terms and self-coupling of the gauge bosons are

$$\mathcal{L}_{gauge} = -\frac{1}{4} F_{\mu\nu}^k F^{k\,\mu\nu} - \frac{1}{4} f_{\mu\nu} f^{\mu\nu}, \tag{1.1.12}$$

with $F_{\mu\nu}^k = \partial_\mu b_\nu^k - \partial_\nu b_\mu^k - g\epsilon_{ijk} b_\mu^i b_\nu^j$ which is the field strength tensor for the $SU(2)_L$ gauge field and $f_{\mu\nu} = \partial_\mu A_\nu - \partial_\nu A_\mu$ is the one for the $U(1)_Y$ gauge field [9, 10].

Then, the fermions and gauge bosons masses are generated through the Higgs mechanism implemented by introducing the Higgs doublet

$$\Phi = \begin{pmatrix} \Phi^+(x) \\ \Phi^0(x) \end{pmatrix}, \tag{1.1.13}$$

where $\Phi^+(x)$ and $\Phi^0(x)$ are respectively a charged and a neutral complex scalar fields. The Higgs field Lagrangian which describes the kinematics and the potential of the boson that generates the Spontaneiously Symmetry Breaking (SSB) is

$$\mathcal{L}_H = (D_\mu \Phi)^\dagger (D^\mu \Phi) - \mu^2 \Phi^\dagger \Phi - |\lambda| (\Phi^\dagger \Phi)^2 \tag{1.1.14}$$

The electroweak SM Lagrangian for leptons also includes the Yukawa term which defines the couplings of the Higgs doublet with the fermion fields from which the fermion masses are generated:

$$\mathcal{L}_Y = \sum_{\alpha=e,\mu,\tau} -y_\alpha \big[\overline{R}_\alpha (\Phi^\dagger L_\alpha) + (\overline{L}_\alpha \Phi) R_\alpha\big]. \tag{1.1.15}$$

After SSB, the $SU(2)L$ and $U(1)_Y$ symmetries are broken, but the symmetry $U(1)_{EM}$ generated by the electric charge operator is preserved. Also, the vacuum expectation value of the scalar field acquires a value different from zero and the Higgs field can be expanded as

$$\Phi = \frac{1}{\sqrt{2}} \begin{pmatrix} 0 \\ v + H \end{pmatrix}, \tag{1.1.16}$$

with $v = \sqrt{-\mu^2/|\lambda|}$ and H the massive Higgs scalar. The Yukawa term in the Lagrangian becomes

$$\mathcal{L}_Y = -(1+\frac{H}{v})[m_e(\overline{e}_R e_L + \overline{e}_L e_R) + m_\mu(\overline{\mu}_R \mu_L + \overline{\mu}_L \mu_R) + m_\tau(\overline{\tau}_R \tau_L + \overline{\tau}_L \tau_R)], \tag{1.1.17}$$

where the charged leptons have acquired a mass

$$m_\alpha = \frac{y_\alpha v}{\sqrt{2}} \quad \alpha = e, \mu, \tau \; . \tag{1.1.18}$$

As said before, only the left-handed neutrino fields enter into the Lagrangian of the original SM. Due to this restriction, neutrinos do not couple to the Higgs boson, a Yukawa interaction can not be built and it is not possible to generate neutrino masses through the Higgs mechanism: the original SM was built for massless neutrinos [8, 10].

From $\mathcal{L}_{lep}$ the weak CC and NC neutrino interactions terms have the form

$$\mathcal{L}_{CC} = -\frac{g}{\sqrt{2}} \sum_{\alpha=e,\mu,\tau} \left(\overline{\nu}_{\alpha L} \, \gamma^\mu \, \alpha_L^- \, W_\mu^+ + \overline{\alpha}_L^- \, \gamma^\mu \, \nu_{\alpha L} \, W_\mu^- \right), \tag{1.1.19}$$

$$\mathcal{L}_{NC} = -\frac{g}{2\cos\theta_W} \sum_{\alpha=e,\mu,\tau} \overline{\nu}_{\alpha L} \, \gamma^\mu \, \nu_{\alpha L} \, Z_\mu; \tag{1.1.20}$$

where θ_W is the weak mixing angle, which is used to parametrize the mixing of the neutral gauge bosons in the electroweak theory. Eq.(1.1.19) and eq.(1.1.20) describe all neutrino interactions. In CC interactions the neutrino is absorbed or emitted in association with a charged lepton. In these interactions it is possible to determine the flavor and also to distinguish if a neutrino or an antineutrino has interacted by observing the charged lepton to which it is coupled. While, in NC interactions, in which the associated charged lepton is not produced, the flavor of the interacting neutrino can not be reconstructed.

Nonetheless, by studying the NC interactions the number of neutrino generations has been ascertained. In fact, eq.(1.1.20) determines the partial decay width of the Z boson into neutrino states, which affects the observable total width of the Z resonance. From the total decay width measurements of the Z boson at LEP, it was determined the number of the neutrino flavors which couple to the neutral boson and interact according to the $SU(2)_L \times U(1)_Y$ model. In figure 1.1

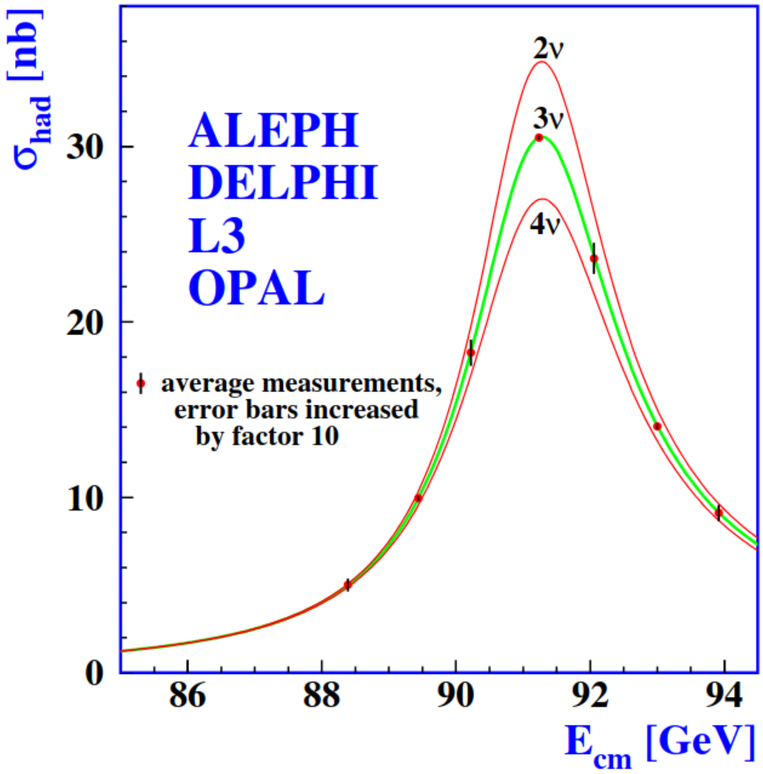

Figure 1.1: Hadron production cross section measurements of the Z resonance. The curves represent the SM expectations for two, three and four neutrino generations with standard model couplings and negligible masses.

the measurements of the hadron production cross section for the Z resonance and the predictions of the SM for two, three and four neutrino generations are shown [11, 12]. The current best estimate is:

$$N_\nu = 2.984 \pm 0.008 \,. \tag{1.1.21}$$

1.2 Neutrino mass

Even if the SM has demonstrated huge successes in providing experimental predictions, it leaves some phenomena unexplained. Among these, the experimental evidence of neutrino oscillation have shown that neutrinos do have mass. The existence of this phenomenon requires a theory beyond the Standard Model (BSM) in order to introduce a corresponding mass term for these particles. In fact, the recent discovery of neutrino oscillations implies that the differences of the neutrino mass-squared are not null and also the states of flavor neutrino are superpositions of definite masses states. However, measurements of neutrino oscillations do not constrain the overall mass scale and their determination is a difficult and challenging problem which is still not solved. Furthermore, the reason why neutrinos are many orders of magnitude lighter than other SM particles is not known and the mechanism that gives them mass remains uncertain [9].

There are different possibilities to introduce a neutrino mass term. Assuming the neutrino to be a Dirac particle, the mass term can be constructed by adding the right-handed component in the electroweak theory. Thus, a four-component spinor is used for the description of the massive neutrino and there would be a Yukawa Lagrangian of the form

$$\mathcal{L}_{Y-D} = \sum_{\alpha=e,\mu\tau} -y_{\nu\alpha}\big[(\overline{L}_\alpha\overline{\Phi})R_{\nu_\alpha} + \overline{R}_{\nu_\alpha}(\overline{\Phi}^\dagger L_\alpha)\big] \tag{1.2.1}$$

After SSB, the neutrino mass term would be

$$\mathcal{L}_{m_\nu} = \sum_{\alpha=e,\mu\tau} -m^D_{\nu_\alpha}\big[\overline{\nu}_{\alpha L}\,\nu_{\alpha R} + \overline{\nu}_{\alpha R}\,\nu_{\alpha L}\big], \tag{1.2.2}$$

where $m^D_{\nu_\alpha}$ is the Dirac mass term given by

$$m^D_{\nu_\alpha} = \frac{y_{\nu_\alpha} v}{\sqrt{2}}. \tag{1.2.3}$$

Therefore, if neutrinos are Dirac particles their mass terms are generated with the Higgs mechanism and they conserve the total lepton number. In this case, neutrinos and antineutrinos have the same mass and differ by the conserved total lepton number which takes the values $L(\nu) = +1$ and $L(\overline{\nu}) = -1$. The right-handed fields are called *sterile*, since they do not enter into the standard charged and neutral currents; while the left-handed flavor fields are called *active* since they participate in weak interactions. Since there are no constraints on the Yukawa couplings, the theory cannot predict the values of neutrino masses (and in general of all SM particles). However, to account the experimental upper limits determined for the neutrino masses the Yukawa couplings must be very small. The masses limits are at most at the eV-scale, this means that if $m_\nu \lesssim 1$ eV the coupling should be $y_\nu \lesssim 10^{-11}$ [8, 9].

However, the nature of neutrinos is not known and they can be Majorana particles. In this case the mass term can be constructed without using a four-component spinor for the description of the neutrino field. For Majorana neutrinos the left ν_L and right ν_R chiral components satisfy the Dirac equation of motion (see eq.(1.1.1) and eq.(1.1.2)) and an additional requirement, known as the Majorana condition. This condition implies that the left and right chiral components are not independent and it can be demonstrated that the two coupled equations of motions become two ways of writing the same equation. The Majorana relation between ν_R and ν_L is

$$\nu_R = \mathcal{C}\overline{\nu}_L^T, \tag{1.2.4}$$

where $\mathcal{C}$ is the charge conjugation matrix. The term $\mathcal{C}\overline{\nu}_L^T$ is equal to the charged conjugate field ν_L^C apart from an arbitrary phase factor, which can be set to zero. By rewriting the field using the above equation

$$\nu = \nu_L + \nu_R = \nu_L + \mathcal{C}\overline{\nu}_L^T = \nu_L + \nu_L^C, \tag{1.2.5}$$

it can be seen that the Majorana condition for the fermion field implies that there is no distinction between particle and antiparticle and the massive field can be described by using only a two-component spinor [8]. In fact, from eq.(1.1.1) and eq.(1.2.4) the Majorana equation for the left chiral field is obtained

$$i\gamma^\mu \partial_\mu \nu_L = m\, \mathcal{C}\overline{\nu}_L^T. \tag{1.2.6}$$

According to eq.(1.2.5) the Majorana condition can be also written as

$$\nu = \nu^C. \tag{1.2.7}$$

Notice that this condition can be imposed only for neutral fermion fields, because the electromagnetic current vanishes for a Majorana field

$$\overline{\nu}\gamma^\mu\nu = \overline{\nu}^C\gamma^\mu\nu^C = -\nu^T\mathcal{C}^\dagger\gamma^\mu\mathcal{C}\overline{\nu}^T = \overline{\nu}\mathcal{C}(\gamma^\mu)^T\mathcal{C}^\dagger\nu = -\overline{\nu}\gamma^\mu\nu = 0. \tag{1.2.8}$$

The most general mass term of this type has the form

$$\mathcal{L} = -\frac{1}{2}\sum_{\alpha=e,\mu,\tau} m_{\nu_\alpha}^M [\overline{\nu}_{\alpha L}\, \nu_{\alpha L}^C + \overline{\nu}_{\alpha L}^C\, \nu_{\alpha L}]\,. \tag{1.2.9}$$

Since there is no distinction between neutrino and antineutrino, in the case of the Majorana mass term the lepton number is not conserved and this term would lead to processes that violate lepton number by two units $\Delta L_{tot} = \pm 2$. Thus, for Majorana neutrinos the lepton number can not be defined.

In order to distinguish if neutrinos are Dirac or Majorana particles, it is necessary to study processes that would provide an experimental evidence that reveals the nature of neutrino masses. Thus, the observation of processes in which the total lepton number is violated, like the neutrinoless double beta decay ($0\nu\beta\beta$ decay) of nuclei, would yield a proof that neutrinos are Majorana particles [10].

To study the $0\nu\beta\beta$ decay only elements for which a single β decay is not allowed but double beta decay is possible are considered. This beacuse a single β decay would be energetically convenient with respect to a $\beta\beta$ decay which is very rare;

therefore, the $\beta\beta$ decay would not be observed. Hence, let us consider even-even nucleus (A, Z) with a mass $M_{A,Z}$ and the odd-odd nucleus with the same atomic number $(A, Z+1)$ with a larger mass $M_{A,Z+1}$. The β decay is not allowed due to energy constraint. However, if there is the even-even nucleus $(A, Z+2)$ with mass smaller than the nucleus (A, Z) the $\beta\beta$ decay can occur:

$$(A, Z) \rightarrow (A, Z+2) + 2e^- + 2\overline{\nu}_e. \tag{1.2.10}$$

The double beta decay has been observed in various nuclei, confirming itself as one of the rarest processes ever observed, with average half-life between $10^{18} - 10^{20}$ years. The $0\nu\beta\beta$ decay can occur only if the neutrino is a massive Majorana particle. In this case, there is the possibility that one of the two antineutrinos (which are both right-handed when created at the leptonic vertex) can change its helicity, with a relative amplitude proportional to m_{ν_e}/E_{ν_e}, and then it is absorbed by the other neutrino, yielding a final state characterized only by $2e^-$ and the nucleus. This process violates the lepton number conservation by two units.

For the search of neutrinoless double beta decay new experiments are employing different experimental methods for the observation of $0\nu\beta\beta$ decay, for example CUORE and GERDA experiments. The CUORE experiment is composed by a cryogenic detector, which uses bolometry techniques to measure the thermal deposit of the electrons in the $\beta\beta$ decay. Instead, the GERDA experiment, uses Germanium detectors to search for the decay in the nucleus of ^{76}Ge isotope.

The $0\nu\beta\beta$ decays give also a possibility to indirectly measure the effective Majorana mass: the half-life of the decay depends on the product of the effective Majorana mass and the nuclear matrix element. Thus, by measuring the half-life and having an accurate knowledge of the nuclear matrix element, the mass can be determined. In fact, for the experiments searching for this decay it is outlined to reach a sensitivity to the effective Majorana mass of a few 10^{-2} eV [10].

In addition to $0\nu\beta\beta$ decay experiments, there are different experimental approaches to measure the absolute masses of neutrinos, which are still not known and their determination is an extremely challenging and active field. For example, cosmological observations can provide constraints on upper bounds on the sum of neutrino masses. In fact, neutrino properties have potentially detectable effects on cosmological data. Hence, studying cosmological observations, upper limits and constraints on neutrino properties can be imposed. For instance, the anisotropies of the CMB power spectrum are strongly affected by the sum of neutrino masses. Thus, by analyzing the spectra of CMB anisotropies it is possible to indirectly infer the sum. However, results are highly model dependent.

Futhermore, measuring the end-point of the β decay spectrum is another way to obtain information about the neutrino mass. The tritium beta decay is the favored reaction

$$^3H \rightarrow {}^3He + e^- + \overline{\nu}_e, \tag{1.2.11}$$

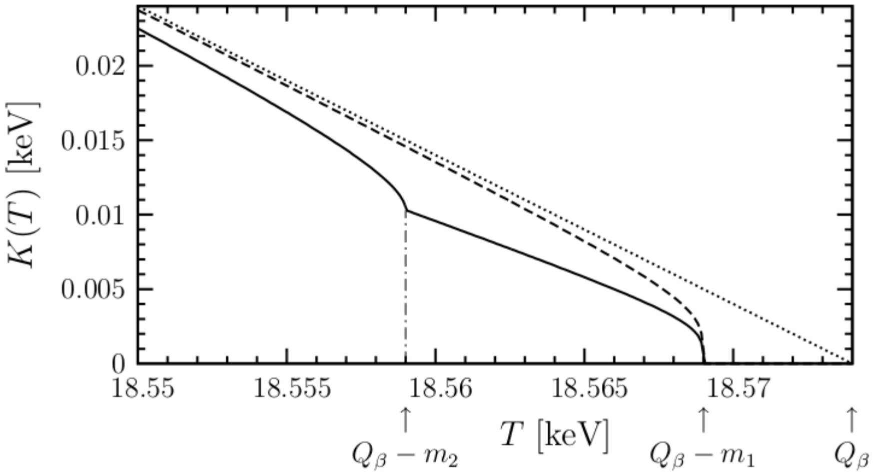

Figure 1.2: Kurie plot for ^3H beta decay. The dotted line represents the linear Kurie function for $m_{\nu_e} = 0$. The dashed line shows the Kurie function for $m_{\nu_e} = 5$ eV. The solid line depicts the Kurie function for two-neutrino mixing with $m_1 = 5$ eV, $m_2 = 15$ eV and $\theta_{12} = \pi/4$ [8].

bacause it is characterized by a small Q-value $Q \simeq 18.57$ keV and it is a superallowed transition. Assuming no neutrino mixing, the differential decay rate is given by

$$\frac{d\Gamma}{dT} = \frac{(V_{ud}\,G_F)^2}{2\pi^3}|\mathcal{M}|^2 F(E) p_e E_e K^2(T), \tag{1.2.12}$$

where V_{ud} is the element of the CKM matrix, G_F is the Fermi constant, $|\mathcal{M}|$ is the nuclear matrix element, $F(E)$ is the Fermi function which describes the electromagnetic interaction felt by the produced electron with the nucleus, p_e and E_e are the electron momentum and energy and $K^2(T)$ is the Kurie function. To measure the neutrino mass it is convinient to study the end-point of the Kurie plot, shown in figure 1.2, which represents the Kurie function

$$K(T) = \left[(Q_\beta - T)\sqrt{(Q_\beta - T)^2 - m_{\nu_e}}\right]^{1/2} \tag{1.2.13}$$

as function of the electron kinematic energy T. If $m_{\nu_e} = 0$ the Kurie function is linear and the eq.(1.2.13) becomes $K(T)|_{m_{\nu_e}=0} = Q_\beta - T$. While, if the electron neutrino is massive, it would imply a deviation from linearity of the Kurie function (dashed line in figure 1.2). Thus, to measure the neutrino mass, experiments should precisely measure the shift in the Kurie plot at the end-point of the electron spectrum [8]. Considering also the neutrino mixing, the Kurie function becomes

$$K(T) = \left[(Q_\beta - T)\sum_{i=1}^{3}|U_{ei}|^2\sqrt{(Q_\beta - T)^2 - m_i^2}\right]^{1/2}, \tag{1.2.14}$$

where m_i are the three mass eigenstates and U_{ei} are elements of the neutrino mixing matrix, that will be discussed in section (1.3.1). In this case, the Kurie function differs from a linear function for

- a shift of the end-point of the electron spectrum,
- kinks in correspondence of the electron kinetic energies such that $T = Q_\beta - m_i$ (excepting for the mass of the lightest neutrino).

The Karlsruhe Tritium Neutrino Experiment (KATRIN) experiment is currently running to perform a precise measurement of the m_{ν_e} studing the tritium beta decay. It has an estimated sensitivity of $m_{\nu_e}^{eff} \sim 0.2$ eV. Recent results of this experiment sets an upper limit of $m_{\nu_e} < 1.1$ eV [12].

1.3 Neutrino mixing and oscillation

The neutrino mixing concerns massive neutrinos and it means that weak eigenstates $|\nu_\alpha\rangle$ do not correspond to the mass eigenstates $|\nu_i\rangle$, but they can be expressed as a linear combination of them. The mixing relation can be written as

$$|\nu_\alpha\rangle = \sum_i U^*_{\alpha i} |\nu_i\rangle \,, \tag{1.3.1}$$

where U is called mixing matrix and it satisfies the unitary condition.

The neutrino oscillation is a quantum mechanical phenomenon which is due to the neutrino mixing. In fact, the mixing and the non-null mass imply that if a neutrino with a momentum $\vec{p}$ is produced in a pure flavor state $|\nu_\alpha\rangle$, at a sufficiently large distance the probability to find it with a different flavor is different from zero [12]. Thus, the neutrino oscillation is a phenomenon in which neutrinos undergo transitions between different flavors as they propagate and it is generated by the interference of different massive neutrinos [8].

1.3.1 Oscillation in vacuum

Consider a neutrino produced in a CC weak interaction, with flavor α and momentum $\vec{p}$. The neutrino is created at time $t = 0$ in a pure flavor state $|\nu_\alpha\rangle$ described by eq.(1.3.1), where the number of active neutrinos of definite flavor is three (ν_e, ν_μ, ν_τ); while the number of the massive neutrino ν_i can be an arbitrary value ≥ 3. Hence, additional neutrinos in the flavor basis would be sterile and do not weakly interact. In the context of three generation mixing only three massive neutrinos are considered. In this context, if there are only three Dirac neutrinos (ν_1, ν_2 and ν_3), the mixing matrix is a 3×3 unitary matrix that depends on four parameters, which are three angles (θ_{12}, θ_{13}, θ_{23}) and one charge-parity (CP) symmetry violation phase (δ_{CP}). Using these parameters the mixing matrix, which is called Pontecorvo-Maki-Nakagawa-Sakata (PMNS) matrix, can be expressed as

$$U = \begin{pmatrix} 1 & 0 & 0 \\ 0 & c_{23} & s_{23} \\ 0 & -s_{23} & c_{23} \end{pmatrix} \times \begin{pmatrix} c_{13} & 0 & s_{13}e^{-i\delta_{CP}} \\ 0 & 1 & 0 \\ -s_{13}e^{i\delta_{CP}} & 0 & c_{13} \end{pmatrix} \times \begin{pmatrix} c_{12} & s_{12} & 0 \\ -s_{12} & c_{12} & 0 \\ 0 & 0 & 1 \end{pmatrix}, \quad (1.3.2)$$

where $c_{ij} = \cos\theta_{ij}$ and $s_{ij} = \sin\theta_{ij}$. In the case of three Majorana neutrinos it depends on six parameters, three angles and three phases (δ_{CP}, η_1, η_2). In this context the mixing matrix is given by

$$U' = U \times \begin{pmatrix} e^{i\eta_1} & 0 & 0 \\ 0 & e^{i\eta_2} & 0 \\ 0 & 0 & 1 \end{pmatrix}. \quad (1.3.3)$$

From eq.(1.1.19) and eq.(1.3.1) can be obtained the leptonic charged current rewritten in mass basis

$$j^{\mu}_{W,L} = 2 \sum_{\alpha=e,\mu,\tau} \overline{\nu}_{\alpha L}\, \gamma^{\mu}\, \alpha_L = 2 \sum_{\alpha=e,\mu,\tau} \sum_i U^*_{\alpha i}\, \overline{\nu}_{iL}\, \gamma^{\mu}\, \alpha_L. \quad (1.3.4)$$

It can be seen that the neutrino generated at the leptonic charged vertex is given by a coherent superposition of massive neutrinos eigenstates. This is due to the fact that if the energies and momenta of the particles which are involved in the neutrino production process are not measured with a sufficient degree of accuracy to resolve the different masses it is not possible the determination of the massive neutrino that is emitted [8].

The mass eigenstates $|\nu_i\rangle$ are the eigenstates of the Hamiltonian

$$\mathcal{H}_{vacuum} |\nu_i\rangle = E_i |\nu_i\rangle, \quad (1.3.5)$$

with $E_i = \sqrt{\vec{p}^2 + m_i^2}$; hence, they are described by plane waves

$$|\nu_i(t)\rangle = e^{-iE_i t} |\nu_i\rangle. \quad (1.3.6)$$

The mass eigenstates evolve in time with different frequencies; thus, the superposition changes in time and a pure flavor $|\nu_\alpha\rangle$ at time $t = 0$ becomes a flavor mixture at $t > 0$.

In fact, the flavor state at time t and after a distance L travelled in vacuum is described by

$$|\nu_\alpha(t)\rangle = \sum_i U^*_{\alpha i} e^{-iE_i t} |\nu_i\rangle. \quad (1.3.7)$$

By applying the unitarity property of the mixing matrix, the eq.(1.3.4) can be inverted

$$|\nu_i\rangle = \sum_{\alpha} U_{\alpha i} \, |\nu_\alpha\rangle \, , \tag{1.3.8}$$

and replacing eq.(1.3.8) in eq.(1.3.7), it becomes

$$|\nu_\alpha(t)\rangle = \sum_{\beta=e,\mu,\tau} \left(\sum_i U^*_{\alpha i} e^{-iE_i t} U_{\beta i} \right) |\nu_\beta\rangle \, . \tag{1.3.9}$$

Then, the oscillation amplitude of this neutrino, produced at time $t = 0$ with flavor α, which undergoes to a CC interaction at time $t > 0$ producing a charged lepton of flavor β is

$$A_{\nu_\alpha \to \nu_\beta}(t) = \langle \nu_\beta | \nu_\alpha(t) \rangle = \sum_i U^*_{\alpha i} U_{\beta i} \, e^{-iE_i t}. \tag{1.3.10}$$

The oscillation probability is

$$P_{\nu_\alpha \to \nu_\beta}(t) = |A_{\nu_\alpha \to \nu_\beta}(t)|^2 = \sum_{i,j} U^*_{\alpha i} U_{\beta i} U_{\alpha j} U^*_{\beta j} \, e^{-i(E_i - E_j)t}. \tag{1.3.11}$$

Let's take into account that detectable neutrinos in oscillations experiments are ultrarelativistic, because their masses are constrained below ~1 eV, but only neutrinos with energies larger than ~100 keV can be detected, due to the experimental energy thresholds in the processes of neutrino detection. For example, in solar neutrino experiments that used gallium (e.g. GALLEX [13], SAGE [14]), the threshold for the reaction $\nu_e + ^{71}\text{Ga} \rightarrow ^{71}\text{Ge} + e^-$ is $E_{th} = 0.233$ MeV [15]. For ultrarelativistic neutrinos the energy can be approximated as $E_i \simeq E + \frac{m_i^2}{2E}$ with $E = |\vec{p}|$. Hence,

$$E_i - E_j \simeq \frac{\Delta m^2_{ij}}{2E}, \tag{1.3.12}$$

where Δm^2_{ij} is the mass-squared difference. Then, approximating $t = L/c$ (in natural units) for localized fields, where L is the source-detector distance, the oscillation probability becomes

$$P_{\nu_\alpha \to \nu_\beta}(L, E) = \sum_{i,j} U^*_{\alpha i} U_{\beta i} U_{\alpha j} U^*_{\beta j} \exp\left(- i \frac{\Delta m^2_{ij} L}{2E} \right). \tag{1.3.13}$$

The probability depends on the distance travelled L, the neutrino energy E, which are parameters that can be tuned in the experiments in order to be sensitive to the oscillation phenomenon. Moreover, it depends also on the mass-squared difference and on the quartic products of the mixing matrix elements. This means that the study of neutrino oscillations do not yield information about the absolute values of the neutrino masses neither about their nature (Dirac or Majorana). In fact, a term $U^*_{\alpha i}U_{\beta i}U_{\alpha j}U^*_{\beta j}$ is invariant under rephasing transformations like $U_{\alpha i} \to e^{i\psi_\alpha}U_{\alpha i}e^{i\Phi_i}$. Thus, the quartic products do not depend on the phases of the mixing matrix.

Similarly to the case of neutrinos, it can be obtained the antineutrino oscillation probability

$$P_{\overline{\nu}_\alpha \to \overline{\nu}_\beta}(L,E) = \sum_{i,j} U_{\alpha i}U^*_{\beta i}U^*_{\alpha j}U_{\beta j} \exp\left(-i\frac{\Delta m^2_{ij}L}{2E}\right), \tag{1.3.14}$$

with the difference that the elements of the mixing matrix are the complex conjugated with respect to the neutrino case. The channels $\nu_\alpha \to \nu_\beta$ and $\overline{\nu}_\alpha \to \overline{\nu}_\beta$ are related by a CP transformation, which correspond to the interchange between particles and antiparticles with also an helicity reversion. If CP invariance is conserved the oscillation probabilities of neutrinos (eq.(1.3.13)) and antineutrinos (eq.(1.3.14)) should correspond. The probability in eq.(1.3.13) can be rewritten by separating the real and imaginary parts of the quartic products,

$$\begin{aligned} P_{\nu_\alpha \to \nu_\beta}(L,E) = \delta_{\alpha\beta} &- 4\sum_{i>j} \mathcal{R}e[U^*_{\alpha i}U_{\beta i}U_{\alpha j}U^*_{\beta j}] \sin^2\left(\frac{\Delta m^2_{ij}L}{4E}\right) \\ &+ 2\sum_{i>j} \mathcal{I}m[U^*_{\alpha i}U_{\beta i}U_{\alpha j}U^*_{\beta j}] \sin\left(\frac{\Delta m^2_{ij}L}{2E}\right). \end{aligned} \tag{1.3.15}$$

Notice that the real part in eq.(1.3.15) is CP conserving, whereas the imaginary term violates the CP invariance since it has opposite sign for neutrinos and antineutrinos: only this term contributes to the CP asymmetry [12]. Thus, the CP violation can be quantified in terms of the Jarlskog invariant, defined as

$$J_{\alpha\beta} = \mathcal{I}m[U_{\mu 3}U_{e2}U^*_{\mu 2}U^*_{e3}] = \frac{1}{8}\sin(2\theta_{12})\sin(2\theta_{23})\sin(2\theta_{13})\cos(\theta_{13})\sin(\delta_{CP}) \tag{1.3.16}$$

In the case in which $\alpha \neq \beta$ the oscillation probability is said *transition probability*; while for $\alpha = \beta$ it is said *survival probability*, and in this case eq.(1.3.15) has not the imaginary part [8].

In the case of three neutrino mixing there are only two of the three squared-mass differences that are independent,

$$\Delta m^2_{21} \equiv m^2_2 - m^2_1, \qquad \Delta m^2_{31} \equiv m^2_3 - m^2_1, \qquad \Delta m^2_{32} \equiv m^2_3 - m^2_2, \tag{1.3.17}$$

since

$$\Delta m^2_{32} + \Delta m^2_{21} - \Delta m^2_{31} = 0. \tag{1.3.18}$$

From neutrino oscillation experiments it is realized that one mass-squared difference (solar Δm_{sol}) is much smaller than the other one (atmospheric Δm_{atm}). However, analyses of oscillation data [16] have been able to determine the sign of Δm_{sol} but not the one of Δm_{atm} and the current measured values are $\Delta m_{sol} \sim 7.5 \cdot 10^{-5} eV^2$ and $\Delta m_{atm} \sim 2.5 \cdot 10^{-3} eV^2$. Choosing the numbers labeling the massive states such that $\Delta m^2_{sol} = \Delta m^2_{21}$ and $\Delta m^2_{atm} = |\Delta m^2_{31}|$, two types of orderings for the spectrum of neutrino masses are possible: the *normal ordering* (NO), in which the two lightest neutrinos are separated by the smallest mass-squared difference Δm^2_{21} and the third one is much heavier ($m_1 < m_2 \ll m_3$); the *inverted ordering* (IO), in which the smallest neutrino is separated from the other two by the largest mass-squared difference $|\Delta m^2_{31}|$ ($m_3 \ll m_1 < m_2$) [8, 15]. In figure 1.3 the two possible orderings are shown.

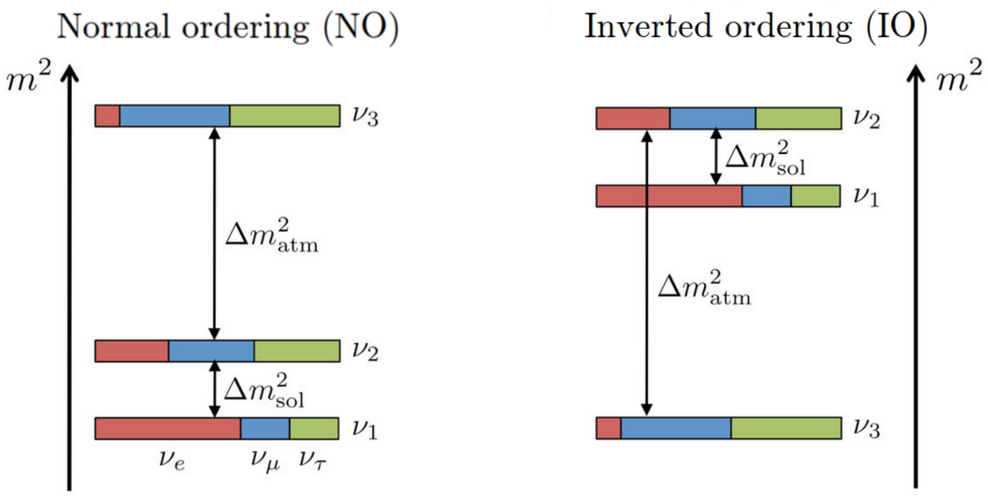

Figure 1.3: Schemes of the two possible mass orderings in the case of three generation mixing: the normal ordering (right) and the inverted ordering (left) [17].

1.3.2 Oscillation in matter

In the case neutrinos propagate through matter, the oscillation probability is further modified with respect to the propagation in vacuum, because they are affected by coherent elastic scattering with particles in the medium and in particular ν_e have different interaction channels with matter with respect to ν_μ and ν_τ. Also incoherent inelastic scatterings can occur but the probability of incoherent scattering is small and it can be safely neglected [8, 12].

Consider the propagation of ν_e, ν_μ and ν_τ in a dense medium with electrons, protons and neutrons. All neutrino flavors are affected by coherent forward elastic weak NC interactions that can occur with any fermion of the medium. The contribution of the NC scatterings can be introduced by an effective potential in the total neutrino Hamiltonian in matter. The NC potential of any flavor neutrino ν_α that interacts with particles in the medium is given by

$$V_{NC} = \frac{\sqrt{2}}{2} G_F \big[-n_e (1 - 4\sin^2\theta_W) + n_p (1 - 4\sin^2\theta_W) - n_n \big], \tag{1.3.19}$$

where G_F is the Fermi constant, n_e, n_p and n_n are correspectively the electron, proton and neutron number densities and θ_W is the Weinberg angle. Assuming the propagation in a neutral medium the contributions from electrons and protons cancel each other and the NC potential simplifies to

$$V_{NC} = -\frac{\sqrt{2}}{2} G_F n_n. \tag{1.3.20}$$

However, this contribution is equivalent for all neutrino flavors and it generates an overall phase shift which is irrelevant for the mixing of neutrinos. Electron neutrinos can also be affected by coherent weak CC interactions with electrons in the medium. Thus, the total Hamiltonian has an extra potential term that accounts for the $\nu_e - e$ elastic scattering of the form

$$V_{CC} = \sqrt{2} G_F n_e, \tag{1.3.21}$$

where n_e is the electron density. Since in most of the media neither μ nor τ particles are present the effective CC potential for ν_μ and ν_τ is null. Thus, the contribution due to CC scatterings generates a phase shift that is relevant for the flavor transitions. In fact, consider an ultrarelativistic left-handed neutrino with flavor α and momentum $\vec{p}$ described by eq.(1.3.1). The neutrino mass states are the eigenstates of the vacuum Hamiltonian, as already shown in eq.(1.3.5). The total Hamiltonian in matter is given by

$$\mathcal{H} = \mathcal{H}_{vacuum} + \mathcal{H}_{MSW}. \tag{1.3.22}$$

The matter Hamiltonian $\mathcal{H}_{MSW}$ that acts on flavor states is

$$\mathcal{H}_{MSW} = \pm 2 G_F n_e(\vec{x}) \begin{pmatrix} 1 & 0 & 0 \\ 0 & 0 & 0 \\ 0 & 0 & 0 \end{pmatrix} \qquad \begin{cases} + & for\ \nu \\ - & for\ \overline{\nu} \end{cases}, \tag{1.3.23}$$

where $\vec{x}$ is the position of the neutrino. Acting on the flavor state

$$\mathcal{H}_{MSW} \left|\nu_\alpha\right\rangle = V_\alpha \left|\nu_\alpha\right\rangle = V_{CC} \delta_{\alpha e} + V_{NC}, \tag{1.3.24}$$

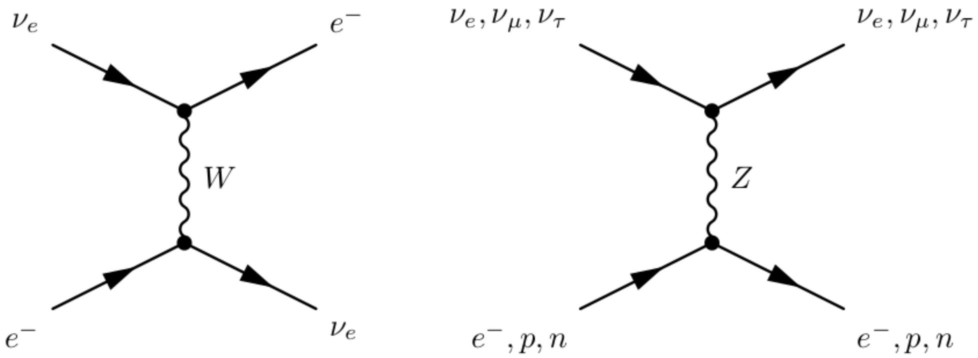

Figure 1.4: Feynman diagrams of the coherent forward weak CC and NC scattering processes, which correspondingly occur through the exchange of the W boson and through the Z boson [8].

where V_α is the effective potential felt by the ultrarelativistic flavor neutrino. Since the flavor transition amplitude is determined by the evolution equation of the flavor state $|\nu_\alpha\rangle$ obtained using the total Hamiltonian in matter, the flavor neutrino propagating in a medium with electronic density $n_e(\vec{x})$ undergoes to oscillation transitions according to the total Hamiltonian, composed by a term due to oscillations in vacuum and another one due to matter effects. Thus, neutrinos that propagates in matter can undergo to coherent forward NC scatterings and electron neutrinos can also have CC scatterings with electrons in the medium. These interactions with matter can be introduced by an effective potential that depends on the density of the matter, and this effect is called Mikheyev-Smirnov-Wolfenstein (MSW) effect. The Feynman diagrams of the coherentforward weak CC and NC scattering processes are reported in figure 1.4.

1.3.3 Neutrino oscillation experiments

Neutrino oscillations have been studied using different detection techniques and neutrino sources. Neutrino experiments can measure flavor transitions in two different observation modes. Assuming to know the neutrino beam flavor composition at source,

- in *Appearance mode*, the experiment detects at a certain distance the appearance of a different neutrino flavor not initially present in the beam;
- in *Disappearance mode*, the experiment studies the survival probability and measures at a certain distance the flux of neutrinos with the same flavor they were produced at source.

The different sources that can be used to observe neutrino oscillations are the Sun, Earth's atmosphere, accelerators and nuclear reactors.

Moreover, accelerator and reactor experiments can be classified depending on the average value of L/E, since it determines the possible range of mass-squared differences experiments are sensitive to (see eq.(1.3.13)). Thus, suitable values of the neutrino energy E and the source-detector distance L should be chosen for the design of accelerator and reactor experiments in order to have an optimized ratio that allow to study the mass splittings.

Short-Baseline experiments (SBL).

- Reactor SBL uses fluxes of $\overline{\nu}_e$ produced by β^- decays of heavy nuclei (e.g. ^{235}U, ^{238}U, ^{239}Pu). The energy of the emitted antineutrinos is of the order of few MeV. The distance between the source and detection points is about several tens of meters. Hence, the covered range is $L/E \lesssim 10$ m/MeV corresponding to a sensitivity of $\Delta m^2 \gtrsim 0.1$ eV^2.

- Accelerator SBL study neutrino beams generated by a proton beam impinging on a target and producing also pions, kaons and muons that lately decay creating neutrinos. Depending on the energy of the proton beam the neutrinos energy can vary. Thus, the ratio L/E can change on the base of the beam energy.

$$\begin{aligned} &L/E \lesssim 10^{-2} m/MeV \qquad \Delta m^2 \gtrsim 10^2 eV^2 \\ &L/E \lesssim 1m/MeV - 1km/GeV \qquad \Delta m^2 \gtrsim 1eV^2 \end{aligned} \tag{1.3.25}$$

Long-Baseline experiments (LBL).

LBL use similar sources to SBL ones but the source-detector distance is larger of two-three orders of magnitude.

- Reactor LBL have $L \sim 1$km. Thus, the covered range is $L/E \lesssim 10^3$ m/MeV corresponding to a sensitivity of $\Delta m^2 \gtrsim 10^{-3}$ eV^2.

- Accelerator LBL are characterized by a source-detector distance about $10^2 - 10^3$ km, yielding to a covered range of $L/E \lesssim 10^3$ km/GeV corresponding to a sensitivity of $\Delta m^2 \gtrsim 10^{-3}$ eV^2.

Very Long-Baseline experiments (VLB).

- Reactor VLB have a source-detector distance of the order of 100 km and $L/E \lesssim 10^5$ m/MeV corresponding to $\Delta m^2 \gtrsim 10^{-5}$ eV^2.

- In accelerator VLB the distance between the source and detection points is about several thousands of km, comparable with the Earth's diameter. The covered range and the sensitivity are $L/E \lesssim 10^4$ km/GeV and $\Delta m^2 \gtrsim 10^{-4}$ eV^2.

Solar neutrinos

Solar neutrinos experiments, with long-baseline reactor experiments, are sensitive to Δm^2_{21} and $\sin^2\theta_{12}$.

Solar neutrino experiments observe neutrinos produced by thermonuclear fusion reactions in the Sun core. According to the Standard Solar Model (SSM) the electron neutrinos are produced in nuclear fusion processes of *pp* and CNO chains [8]. The majority of neutrinos are generated by *pp* reactions that can be summarized as $4p \rightarrow^4\text{He} + 2e^+ + 2\nu_e$ and the predicted spectrum of neutrino fluxes predicted by SMM is reported in figure 1.5. The total expected flux of *pp* solar neutrinos on Earth is about $6 \cdot 10^{10}$ cm^{-2} s^{-1} with a mean energy of $\langle E_\nu \rangle \simeq 0.42$ MeV.

Before the neutrino oscillation discovery, pioneering solar neutrino experiments observed a significantly smaller neutrino flux than the theoretical prediction (done without considering the oscillation phenomenon). This discrepancy is known as the solar neutrino problem.

Important experiments were the Davis's experiment at Homestake mine (S. Dakota), GALLEX/GNO at Gran Sasso (Italy), SAGE at Baksan (Russia) and Kamiokande (Japan). The Homestake Chlorine experiment observed the ^{7}Be and ^{8}B ν_e fluxes exploiting the reaction $\nu_e +^{37}\text{Cl} \rightarrow e^- +^{37}\text{Ar}$ which has an energy threshold of 814 keV. The experiment observed a flux that was almost 1/3 of the one expected (assuming no neutrino oscillations) [10]. The Radiochemical GALLEX/GNO and SAGE experiments detected neutrinos through the observation of the reaction $\nu_e +^{71}\text{Ga} \rightarrow e^- +^{71}\text{Ge}$ which has an energy threshold of 233 keV. This technique allow to detect *pp* and ^{7}Be neutrinos. Also these experiments measured a deficiency in the solar neutrino flux respect to the theoretical predictions. The Kamiokande experiment was a 3000 tons water Cherenkov detector that observed solar neutrinos elastic scatterings with an energy threshold of 6.5 MeV. This experiment was sensitive to all flavors of ^{8}B neutrinos and it measured smaller numbers of observed solar neutrinos compared to the expectations [12].

The resolutive measurements for the solar neutrino problem came from the Sudbury Neutrino Observatory (SNO) experiment in Canada. The SNO experiment consisted of a spherical vessel containing 1000 tons of heavy water (D_2O) and surrounded by an H_2O shield. The Cherenkov light was detected by an array of PMTs. This experiment could study three different reactions: elastic scattering with an electron, CC interaction $\nu_e + d \rightarrow e^- + p + p$ and NC interaction $\nu_\alpha + d \rightarrow \nu_\alpha + p + n$. The elastic scattering is sensitive to all neutrino flavors but mainly to ν_e; while NC reaction is sensitive to all flavors with equal cross sections; the CC interaction only to ν_e. This experiment provide the solution of the solar neutrino problem, because with CCevents it was possible to measure the flux of electron neutrinos, while, with NC events was determined the the total flux given

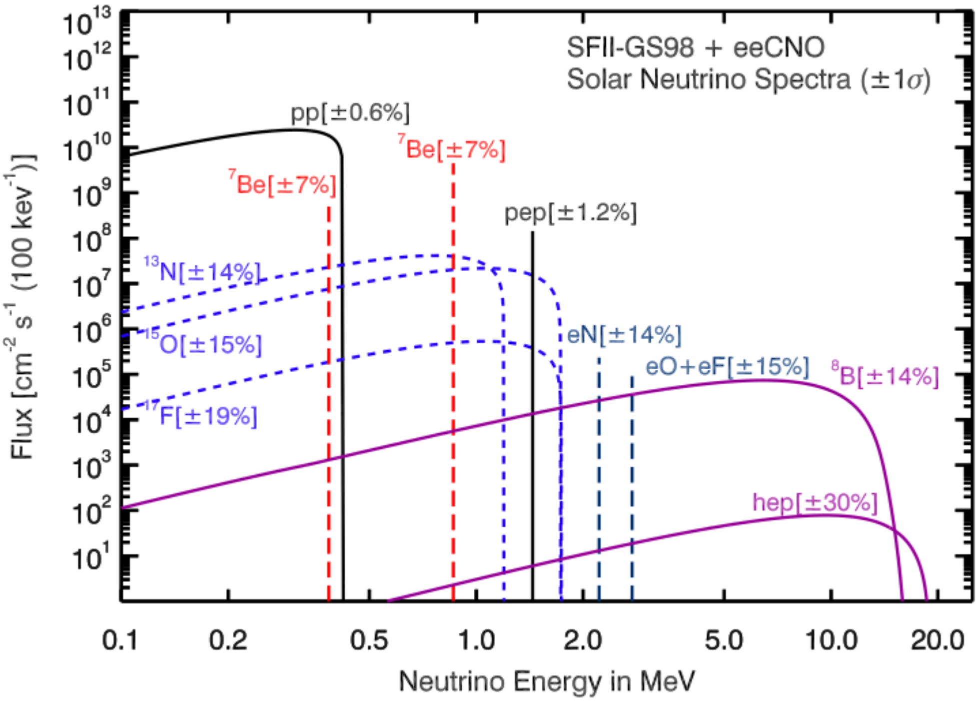

Figure 1.5: Predicted spectrum of solar neutrino energies [12].

by the sum of the fluxes of all flavors. The results demonstrated that the ν_e from the Sun to the Earth oscillate into ν_μ and ν_τ [12].

Moreover, solar neutrinos are affected to matter effects while they propagate through the Sun. In fact, assuming neutrino oscillations, also matter effects must be taken into account to explain the ν_e rates observed by the solar neutrino experiments and the reason why different deficiencies of ν_e were measured for different energy thresholds. Matter effects also provide the determination of the sign of the mass-squared difference Δm^2_{sol}. The parameters values obtained by analyzing solar neutrino data are

$$\Delta m^2_{sol} \sim 7.5 \cdot 10^{-5} eV^2 \qquad \sin^2\theta_{sol} \sim 0.3. \tag{1.3.26}$$

Atmospheric neutrinos

The atmospheric neutrino oscillation experiments, with accelerator neutrinos experiments, have constrained the values of $\Delta m^2_{31(32)}$ and $\sin^2 2\theta_{31(32)}$.

Atmospheric neutrinos are produced due to the interactions of cosmic rays (CR) with nucleons in the upper Earth's atmosphere. These interactions generate hadrons cascades in which also pions and kaons are produced. Neutrinos are generated from the decay chains of pions and kaons (e.g. $\pi^+ \to \mu^+\nu_\mu$ followed by

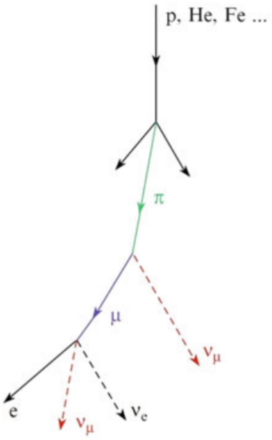

Figure 1.6: schematic example of an atmospheric neutrino production CR chain. [18].

$\mu^+ \to e^+\nu_e\overline{\nu_\mu}$). A schematic example of the atmospheric neutrino production is reported in figure 1.6.

Considering the dominant production mode, at low energies (~1 GeV) the ratio between the two flavors is expected to be

$$\frac{\nu_\mu + \overline{\nu}_\mu}{\nu_e + \overline{\nu}_e} \simeq 2, \tag{1.3.27}$$

since most of the muons decay before reaching the Earth surface; while for higher energies some muons do not decay and the ratio increases.

Atmospheric neutrinos can also be distinguished between upward-going neutrinos, which are produced in the other side of the Earth and come through the Earth after traveling a length of $\sim 10^4$ km, and downward-going neutrinos, which are produced above the observation site and travel ~ 10 km in the atmosphere.

Atmospheric neutrinos were studied by using different types of detectors: water Cherenkov detectors, for example the Super-Kamiokande experiment, liquid scintillator detectors such as the MACRO experiment, and iron tracking calorimeters, for instance the Soudan experiment.

The detection principle of water Cherenkov detectors is based on the collection of the optical photons produced by the Cherenkov effect of relativistic particles crossing the detector. The light is observed by Photo-Multiplier Tubes (PMTs) and to reconstruct the event, the number of photons and their arrival times are used to infer the energy and the direction of the crossing particle. The identification of charged leptons is essential to study the neutrino CC interactions. Thus, it's very important the discrimination between muons and electrons and the distinction is based on the information from Cherenkov ring patterns. In fact, $e^\pm$ and γ particles undergo to electromagnetic (e.m.) showers and Coulomb scatterings such that the event is characterized by a diffuse and fuzzy ring; while, a μ-like particle lose energy emitting Cherenkov light resulting in a more sharp ring event.

The MACRO experiment at Gran Sasso consisted of a large area multipurpose apparatus located underground, under an average rock overburden of ~ 3700 mwe.[1] The detector, shown in figure 1.7, had a modular structure, the bottom part was composed by layers of streamer tubes interleaved with planes of passive absorbers and liquid scintillators; the upper part contained the electronics and it was covered by a layer of scintillators and four planes of streamer tubes. The tracking was performed using the hits in streamer tubes, the time-of-flight information was provided by the scintillation system and allowed to identify upward-going events with respect to the down-going ones [19]. MACRO studied the flux of ν_μ observing different atmospheric neutrino interaction topologies. *Up throughgoing muons* events from muon neutrino interaction in the rock below the detector with the resulting muon crossing the whole apparatus; *upgoing stopping muons* from ν_μ interactions in the rock below yielding upgoing muon tracks contained in the detector; *partially contained upgoing muons* from muon neutrino interaction inside the detector and an upgoing muon track; *semicontained downgoing muons* from ν_μ interactions in the detector and muon induced downgoing tracks

Initially, anomalies in the flux ratio $\nu_\mu/\nu_e = (\nu_\mu + \overline{\nu}_\mu)/(\nu_e + \overline{\nu}_e)$ with respect to the expectations were observed from experiments on atmospheric neutrinos. These anomalies were then found to be dependent on the zenith angle, thus on the length traveled by neutrinos. In 1998, SuperKamiokande and MACRO, using different experimental techniques, simultaneously presented the evidence for atmospheric neutrino oscillations and the observed deviations from no-oscillation predictions pointed to the $\nu_\mu \to \nu_\tau$ oscillation scenario. Assuming no oscillations, at neutrino energies $E \geq 0.9$ GeV the fluxes of upward-going and downward-going neutrinos are expected to be symmetric (at lower energies the fluxes are affected by the geomagnetic cutoff) [10]. However, these experiments observed a significant deficit of upward-going muon neutrino flux. While, the e-like data was roughly in agreement with the no-oscillation assumption. The zenith angular distributions observed by SuperKamiokande are shown in figure 1.8. Later, also other experiments as Soudan 2 observed these anomalies. This experiment was an iron tracking calorimeter operating as a time projection chamber. The calorimeter's active elements were plastic drift tubes filled with a mixture of argon-CO_2 gas and encased in a honeycomb matrix of steel plates. Good imaging and particle identification could be performed yielding to a good determination of the energy and direction

---

[1] meter water equivalent (mwe). A laboratory at 1 kmwe is shielded from cosmic rays similarly as a laboratory 1 km below the surface of a body water. On average 1 kmwe= 10^5 g cm^{-2} of rock [18].

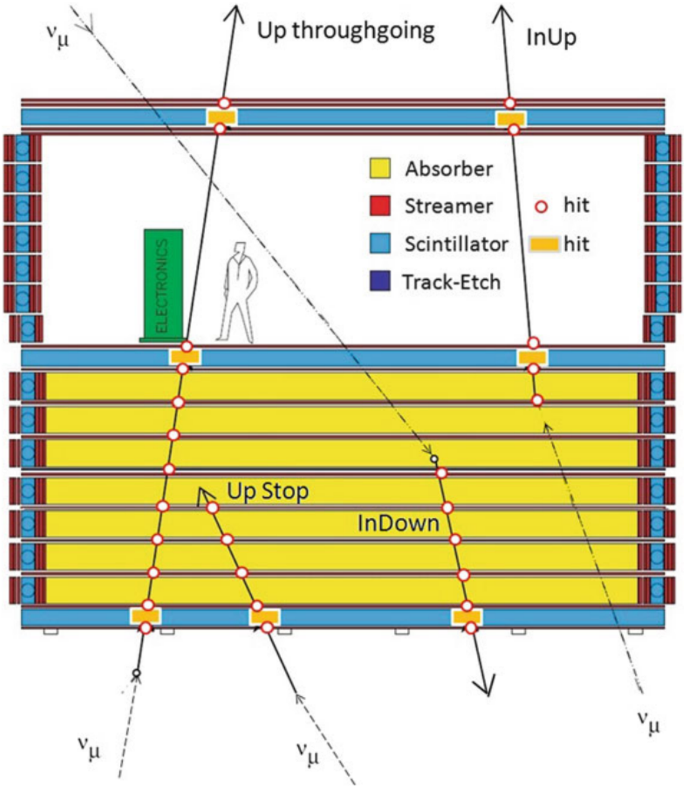

Figure 1.7: Schematic view of the MACRO detector [18].

of neutrinos [20].

The atmospheric neutrino anomaly could be explained by the disappearance of muon neutrinos due to oscillations between ν_μ and ν_τ. The observation of ν_τ CC interactions are experimentally difficult due to the high energy threshold for the interaction (E> 3.5 GeV) and the short life time of the charged lepton τ. Inspite of the experimental difficulties, the discovery of $\nu_\mu \to \nu_\tau$ oscillations in appearance mode with a significance larger than 5σ were reported by OPERA in 2012 [12, 21].

Analyzing the atmospheric neutrinos data, the corresponding oscillation parameters are found to be

$$\Delta m^2_{atm} \sim 2.5 \cdot 10^{-3} eV^2 \qquad \theta_{atm} \sim 45^\circ. \tag{1.3.28}$$

Accelerator neutrinos

Neutrino beams at accelerators are obtained by a proton beam impinging upon a nuclear target producing mesons. Among secondary particles, pions and kaons are focused with the so called magnetic horns into a beam, towards the desired direction before they decay into neutrinos. Other mesons and muons are stopped

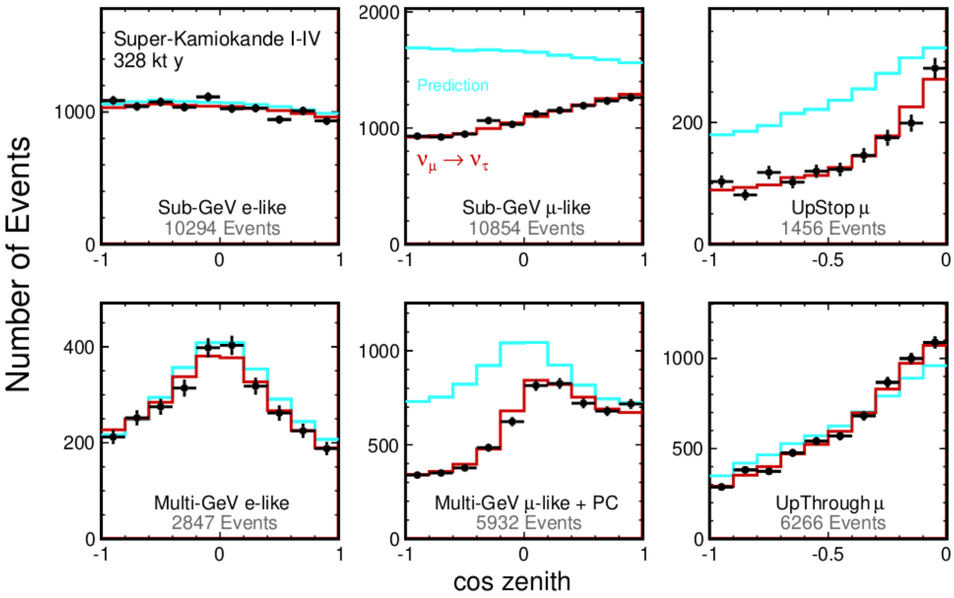

Figure 1.8: SuperKamiokande results: experimental data, MC predictions with neutrino oscillations and MC predictions in the non oscillation hypothesys are reported as function of the zenith angle. Electron and nuon events are shown. Blue histograms represent the MC predictions without neutrino oscillations, red ones show two-neutrino oscillation MC curve [12].

in the beam dump and soil. Conventional neutrino beams mainly contain muon neutrinos or antineutrinos, since pions are the most abundant products of the proton-target collisions. Moreover, regulating the magnetic horns, the dominant component of the beam can be choosen to be of neutrinos or antineutrinos. However, beam contaminations are possible. For example, chosing to have a ν_μ beam, most of the neutrinos come from the decay $\pi^+ \to \mu^+\nu_\mu$. Beam contaminations come from subsequent muon decay $\mu^+ \to e^+\nu_e\overline{\mu}$, pion decay $\pi^+ \to e^+\nu_e$ and kaon decay into $e^+\pi^0\nu_e$. Due to beam contaminations, many LBL experiments are constitued by two detectors, a near detector and a far detector. The near detector provide high statistics characterization of the neutrino beam close to the source and information about the flux, the energy spectrum and interaction cross sections in order to reduce the systematic uncertainties due to neutrino flux and ν-nucleus interactions. The far detector studies the flux of neutrinos and their possible flavor oscillation after travelling the experiment baseline [12].

The first LBL experiment was K2K with a total baseline of 250 km. It used a muon neutrino beam with $\langle E_\nu \rangle \sim 1.3$ GeV, produced by the KEK proton synchroton, directed towards the SuperKamiokande detector. The near detector, 300 m far from the source, was 1 kt water Cherenkov detector combined with a set of fine-grained deterctors. This experiment confirmed the atmospheric neutrino observations that reported muon neutrino disappearance.

MINOS was another accelerator experiment that used a beam from FNAL (Fermi National Accelerator Laboratory), directed towards the far detector in Soudan mine. The baseline was of 735 km and both the near and the far detectors were iron-scintillator tracking calorimeters with a toroidal magnetic field. Also this experiment confirmed the muon neutrino disappearance and it measured atmospheric neutrino oscillation parameters [22].

Moreover, as mentioned before, the OPERA experiment with the CNGS (CERN to Gran Sasso) beam confirmed the oscillation of atmospherinc ν_μ into ν_τ. It was characterized by a baseline of 732 km with a beam of energy of 17 GeV produced at CERN. It has been the first experiment that observed $\nu_\mu \rightarrow \nu_e$ oscillations [21].

The T2K experiment is characterized by a high-intensity proton synchroton accelerator, a set of near detectors about 280 m from the neutrino source, the on-axis INGRID far detector (iron-scintillator tracking detector) and the SuperKamiokande detector which performs off-axis neutrino measurements with an angle of 2.5°. This experiment, with a baseline of 295 km makes use of neutrino beam with a peak energy of 0.6 GeV. It has been the first experiment to observe $\nu_\mu \rightarrow \nu_e$ oscillations.

The NOνA experiment is an off-axis neutrino experiment with a beam with a peak around 2 GeV. The NOνA far detector is located in Minnesota, 810 km far from the source, at an off-axis angle of 14.6 mrad; while the near detector is about 1 km from the source. Both are tracking calorimeters detectors. This experiment is committed to the observation of ν_μ ($\overline{\nu}_\mu$) disappearance and ν_e ($\overline{\nu}_e$) appearance.

Reactor neutrinos

Nuclear reactors are important sources of $\overline{\nu}_e$ produced in beta decays of heavy nuclei. The main neutron-rich nuclei used for the fission chain reactions are ^{235}U, ^{238}U, ^{239}Pu and ^{241}Pu. The electron antineutrino production rate and spectrum can be estimated using the information about the thermal power output and fuel composition as a function of time. However, the production of antineutrinos from fission reactions is isotropic; thus, the flux decreases rapidly with distance from the source. The detection of reactor antineutrinos is based on the inverse beta decay process $\overline{\nu}_e + p \rightarrow e^+ + n$. This reaction is characterized by a prompt energy released by the positron annihilating with a surrounding electron producing two photons that can be detected in scintillator detectors. The neutron capture on nucleus after thermalization produce a delayed energy release with respect to the prompt signal. Hence, the inverse neutron decay process can be detected looking for the coincidence of these two signals.

The KamLAND experiment takes advantage of 55 reactors located at an aver-

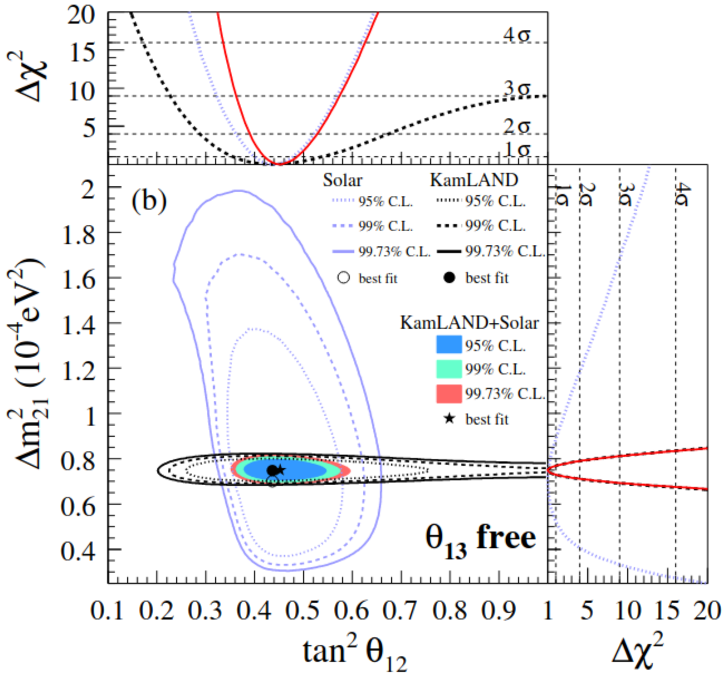

Figure 1.9: Allowed regions in the $(\tan^2\theta_{12}, \Delta m^2_{21})$ plane for three generation mixing analysis using solar and KamLAND data. The side planes show the $\Delta\chi^2$ profiles [23].

age distance of 180 km from the Kamioka mine in which is situated the KamLAND detector. The detector consists of 1 kt of high-purity liquid scintillator contained in a 13 m diameter spherical balloon of transparent nylon. The $\overline{\nu}_e$ spectrum is estimated from the measurements of beta decays spectra from fission of uranium and plutonium and the average energy $\langle E_{\overline{\nu}_e}\rangle \simeq 3.6$ MeV. Thus, this experiment is optimized to study neutrino oscillations related to the solar mass-squared difference. KamLAND first results in 2002 showed the $\overline{\nu}_e$ disappearance at the 99.95% confidence level (CL) and confirmed the value of the mixing angle found by solar neutrino experiments. Moreover, this experiment has a good energy resolution but it doesn't see many events; on the other hand, solar neutrino experiments have a large statistical power but a poor energy resolution. Thus, from a joint analysis of the data of KamLAND and solar neutrino experiments it was possible to constrain a small allowed region for the values of the Δm^2_{12} and $\sin^2\theta_{12}$ oscillation parameters, as shown in figure 1.9.

Three nuclear reactor experiments have been realized to measure the value of $\sin^2\theta_{13}$ from the disappearance of $\overline{\nu}_e$: Double Chooz (France), Daya Bay (China) and RENO (Korea). These three experiments have proved a non-zero value of θ_{13}

and a significant contribution come by Daya Bay experiment which has measured a value of $\sin^2 2\theta_{13} = 0.084 \pm 0.005$ [24].

1.4 Open questions of neutrino physics

The pioneer stage of investigation of neutrino masses, mixing and oscillations is almost concluded, and modern experiments are pursuing for a new high precision measurements era. Thanks to the many recent results, neutrino oscillations phenomenon has been well-established as a quantum mechanical phenomenon and in the last decades neutrino experiments allowed the estimation of some oscillation parameters. However, even if neutrino physics is now entering in a new precision era, there are some open questions that must be addressed:

- What are the absolute values of the neutrino masses?
- What is the correct ordering of the neutrino masses? What is the sign of Δm^2_{31}?
- Are neutrinos Majorana or Dirac particles?
- Is θ_{23} maximal?
- Is the CP symmetry violated in the lepton sector? What is(are) the value(s) of the CP phase(s)?
- What is the origin of neutrino masses and flavor mixing?
- Is the number of massive neutrinos equal to the number of the flavor neutrinos (three) or larger than three?

Many neutrino experiments of the next generation with artificial neutrino sources have started or will start in the near future the investigation of the neutrino pending questions to which there are still no answers [10].

Chapter 2

Dune Experiment

The Deep Underground Neutrino Experiment (DUNE) is an international world-class experiment which will enable to address to some of the open questions in particle physics. DUNE primarily aims to study long-baseline neutrino oscillations, neutrino astrophysics and to search for nucleon decay. It is under development in U.S. and it will consist of three main components [1]:

- the high intensity, wide band (anti)neutrino source generated at the Long-Baseline Neutrino Facility (LBNF) at the Fermi National Accelerator Laboratory (Fermilab) in Illinois,
- the Near Detector (ND) complex installed 574 m far from the neutrino source,
- the Far Detector (FD) located 1.5 km underground at Sanford Underground Research Facility (SURF) in South Dakota, that will consist of four modular, Liquid Argon Time-Projection Chambers (LArTPC) with a total mass of 70 kt.

The total baseline that separates the neutrino source from the FD is of 1285 km (measured along the travel direction through the Earth). In figure 2.1 is shown a schematic layout of the experiment.

The scientific goals of the DUNE experiment are categorized according to different priorities and are grouped into primary objectives and secondary ones [1, 25, 26]. In particular, the primary objectives of the experiment, that will be further described in section 2.4, are the followings:

- the precision measurements of oscillation parameters, in particular the observation of CP violation and the definitive determination of neutrino mass ordering, in the three-flavor mixing picture;

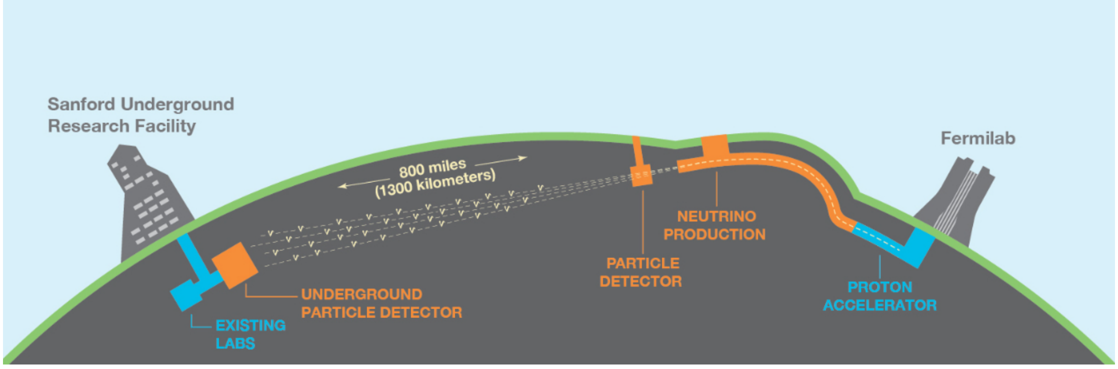

Figure 2.1: Schematic view of DUNE experiment with the LBNF beamline and the ND at Fermilab in Illinois and the FD in South Dakota [3].

- the collection and the analysis of the neutrino flux from a core collapse SuperNova (SN) within our galaxy, phenomenon that is likely to happen during the lifetime of the DUNE experiment;
- the search for proton decay in different decay modes.

The scientific program of the DUNE experiment includes additional objectives to the driving goals introduced above. In fact, the capabilities required for the primary goals of the DUNE physics program also open the opportunities to

- investigate additional BSM signatures related to accelerator-based neutrino oscillation measurements, such as sterile neutrinos, non-standard interactions (NSIs), non-unitarity of the PMNS matrix, violation of the Lorentz symmetry, violation of the Charge-Parity-Time reversal symmetry (CPT);
- measure neutrino oscillation phenomena using atmospheric neutrinos;
- measure neutrino flavor transitions and study solar physics using solar neutrinos;
- search for Dark Matter (DM): light-mass DM particles could be detected via NC-like interactions with electrons or nucleons in the ND, while boosted DM search can be performed using the FD;
- perform a rich neutrino interaction physics program which includes precision measurements of neutrino cross-sections, nuclear effects and the structure of nucleons;
- measure astrophysical and geophysical phenomena using medium and low-energy neutrinos.

2.1 The LBNF neutrino beam

The LBNF beamline facility, reported in figure 2.2, will produce the very high power and intense neutrino beam that will be generated from a megawatt-class proton accelerator at Fermilab and will be directed at the DUNE far detector in South Dakota. In order to optimize the oscillation physics potential for a baseline of 1300 km, the facility will provide wide-band, high purity ν_μ ($\overline{\nu}_\mu$) beam with a flux having a peak at ∼2.5 GeV and ranging between 0.5 and 5 GeV, in order to cover the first and the second oscillation maxima, expected at ∼2.4 and ∼0.8 GeV for the DUNE experiment [25].

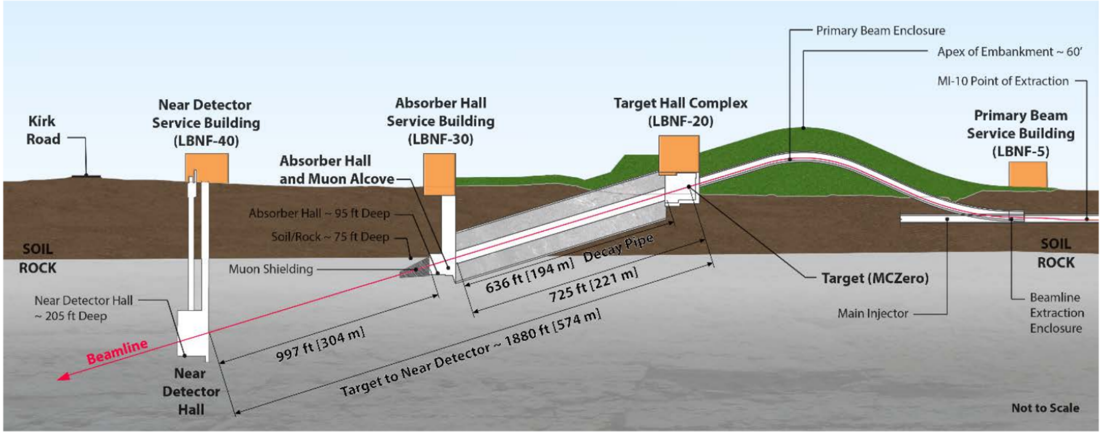

Figure 2.2: The DUNE neutrino beamline longitudinal section [27].

The neutrino beam will be obtained from a primary proton beam, in the energy range of 60-120 GeV, extracted from the Main Injector's (MI) MI-10 straight section using a single-turn extraction. For 60-120 GeV operation, considering the Proton Improvement Plan II (PIP-II) upgrade expected for Fermilab accelerator complex, the single turn extraction will deliver $7.5{\cdot}10^{13}$ protons in one cycle (0.7 s - 1.2 s) to the LBNF target in 10 μs, resulting in a beam power of 1.2 MW. It is planned also a further upgrade to achieve a beam power of 2.4 MW by 2030.

Thus, the proton beam is send though the extraction and transport components over a man-made hill. The beam transport is expected to take place with negligible power losses. At the top of the hill, which is 18.3 m above the ground, the beam is bent downwards, toward a target located in the LBNF Target Hall [25].

Almost the 85% of the protons interact with a graphite-beryllium target. The charged mesons produced, mainly pions and kaons, are sign selected and focused by a set of magnetic horns into a decay pipe, 194 m long and 4 m in diameter, directed towards the FD. The horns' inner conductors have a double parabolic shape and can be operated at currents of the order of hundreds kA.

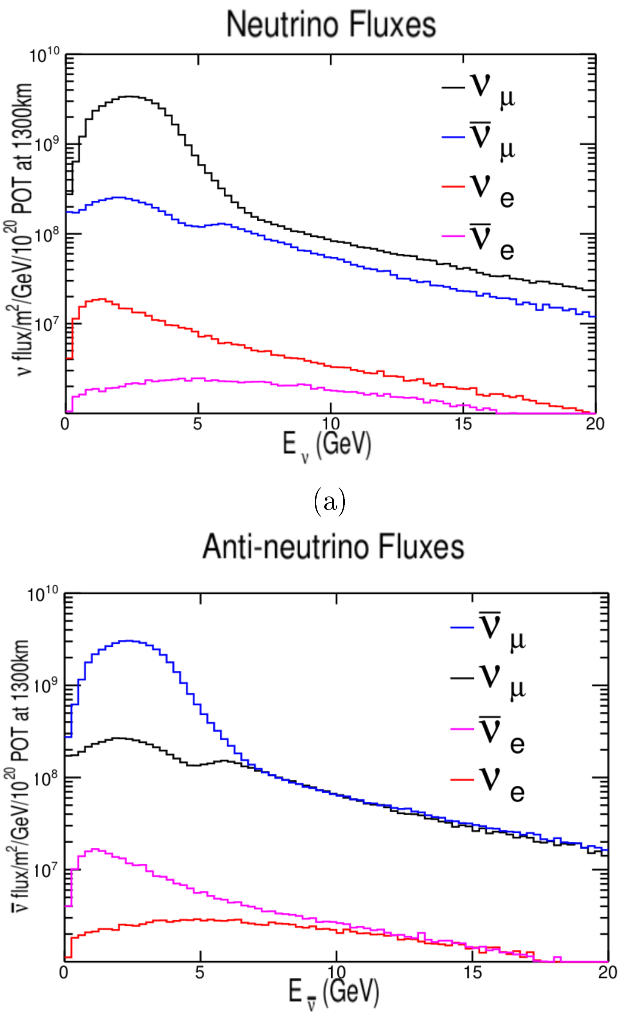

(a)

(b)

Figure 2.3: Geant4 simulation of the LBNF beamline for the neutrino beam fluxes (a) and antineutrino beam fluxes (b). The horn current is assumed to be 200 kA, the target to be located 35 cm in front of the horn 1, the decay pipe to be 204 m long and 4 m in diameter and air-filled [25].

The magnetic focusing horns can be used with two different opposite polarities, in Forward Horn Current (FHC) or Reverse Horn Current (RHC) configurations, focusing either positive or negative hadrons and creating high purity (more than 90% in the oscillation region) ν_μ or $\overline{\nu}_\mu$ beams, respectively [25]. Neutrinos are obtained from mesons decays occurring along the pipe. The mesons in the pipe decay into muons and neutrinos. At the end of the pipe, an absorber is used to remove any residual hadronic particles. The absorber is composed by aluminium and steel water-cooled blocks and the outer part consists of steel and concrete shielding cooled by forced-air [28].

In figure 2.3 are shown the neutrino flux components simulated using Geant4 for both horn polarities. As it can be seen in the figure, each beam polarity is characterized by

- a $< 10\%$ "wrong-sign" contamination ($\overline{\nu}_\mu$ in ν_μ-dominated beam or ν_μ in $\overline{\nu}_\mu$-dominated beam) due to wrong-sign hadrons that propagate down the center of the focusing horns and decay;
- a $\leq 1\%$ contamination of ν_e and $\overline{\nu}_e$, in the signal region of the ν_e appearance, due to the decays of kaons and of tertiary muons from pion decays.

Uncertainties on the neutrino fluxes comes mainly from uncertainties in hadrons originated off the target and uncertainties in the beam parameters, for example horn currents and horn and target position [26].

2.2 The Far Detector

The DUNE FD will be located in South Dakota at SURF, 1285 km far from the neutrino production point and 1.5 km underground, in a facility that consists of three caverns: north and south detector caverns and a central utility cavern for the detector's supplementary system. In figure 2.4 the cavern layout for the far detector is shown.

2.2.1 The FD design

The FD will be a modular liquid argon time-projection chamber with a total mass of roughly 70 kt of liquid argon (LAr) that will serve as target for the neutrino interactions. It will consist of four LArTPC detector modules, each with a fiducial mass of at least 10 kt, that will be enclosed in a cryostat containing 17.5 kt of LAr [1]. The LArTPCs enable high precision identification of neutrino flavors and to reconstruct neutrino interactions with excellent event imaging capabilities. Currently, two different LArTPC technologies are considered for the DUNE FD: i) the single-phase (SP) that will be used for the first two LArTPC modules and ii) the dual-phase (DP), proposed for one of the other modules. The technology for the forth module, called "module of opportunity" is not yet defined.

In figure 2.5 a 58.2 m long SP LArTPC module is shown. The module is characterized by two cathode planes and three wire readout anode planes. The anode planes collect the ionization and scintillation charge generated by a charged particle interacting the LAr volume. These planes are composed by Anode Plane

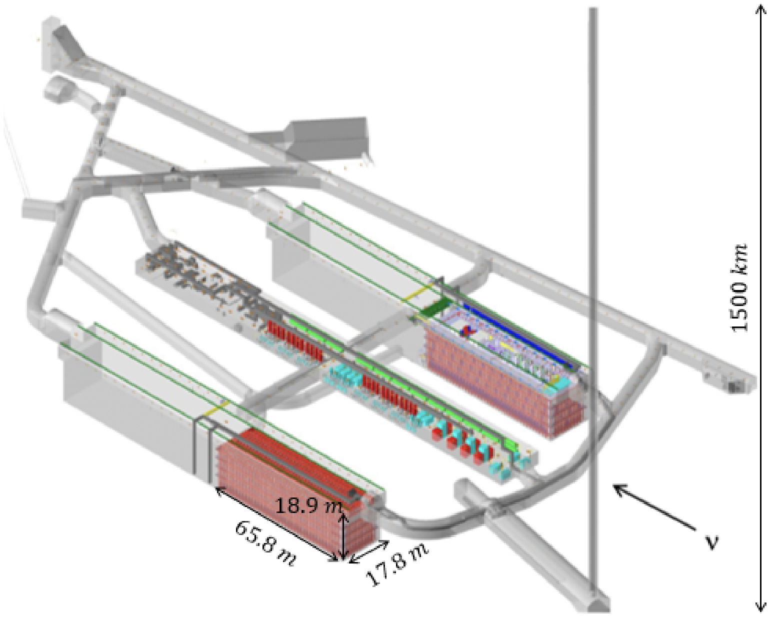

Figure 2.4: DUNE FD overview with the cryostats for the first two LArTPC modules (red) [1].

Assemblies (APAs), which are 6 m high and 2.3 m wide, and each anode wall has a total of 50 APA stacked two by two. As illustrated in figure 2.6, each APA has three layers of active wires on both the two sides and an additional shielding layer around them. Between the layers a relative voltage is chosen in order to have the first two layers (U and V) to be transparent to the drifting electrons that will be collected by the final layer (X). The spacing of the wires that form the layers, approximately 5 mm, defines the spacial resolution of the APA. The front-end readout electronics are attached at the bottom end of the bottom APA of the anode wall and at the top end of the top APA. Given that no signal amplification is provided inside the cryostat, very low noise electronics is required to have a readout with suitable signal-to-noise (S/N) ratio. In addition, inside the APA the Photon Detection system (PD) is installed to collect scintillation photons [1].

In SP technology, all the detector components in the cryostat are immersed in liquid and when charged particles traverse the LAr volume ionization electrons and scintillation photons are produced. The ionization charge drifts horizontally in a constant electric field of 500 V/cm, corresponding to a cathode voltage of 180 kV, towards vertical readout anode planes. The maximum drift length is 3.5 m. Two of the position coordinates are provided by the location of the fired wires, the third spatial dimension is obtained by the drift time [1]. The scintillation photons are produced due to LAr excitation, approximately $2.4 \cdot 10^4$ PE/MeV.

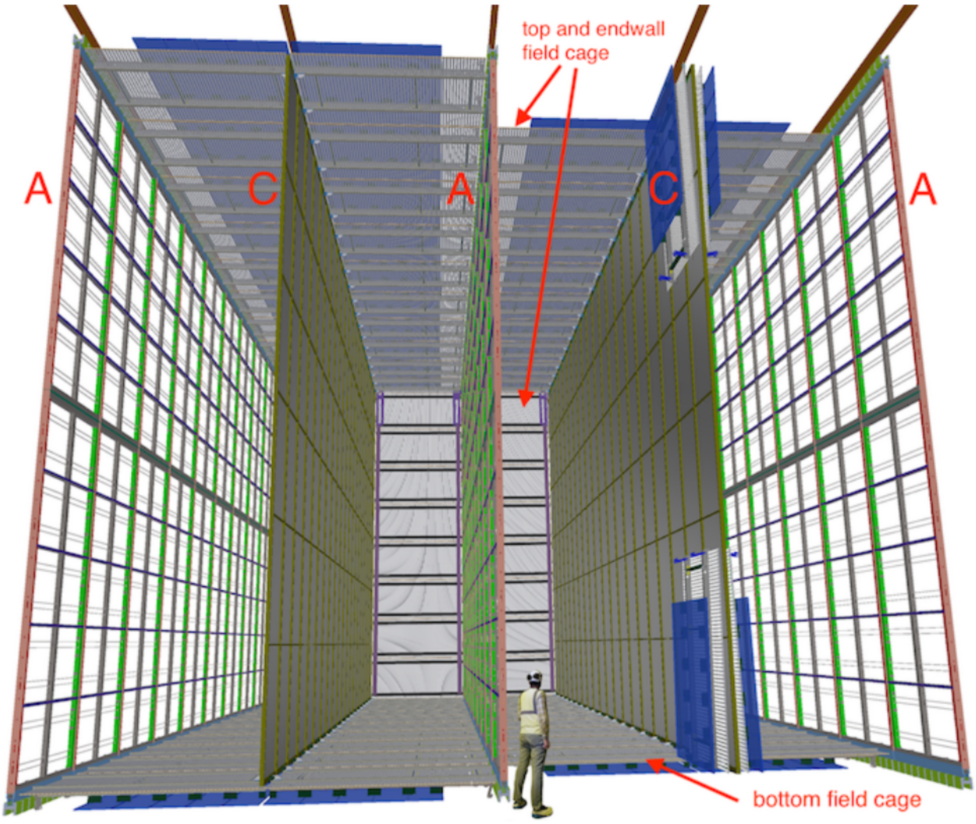

Figure 2.5: Schematic view of a DUNE FD single-phase module. Anode (A) and cathode (C) planes are alternated and the LArTPC is divided into four independent drift volumes. The field cage surrounds the drift regions between the anode and cathode planes [1].

Being fast signal with respect to the drift time, the scintillation light is collected by the PD system and provides the initial start time of the event, representing the time when ionization electrons begin to drift. The general operating principle of a SP module is reported in figure 2.7. The SP module design provides sub-centimeter granularity for all charged particles originated from interactions of solar and supernova neutrinos ($\mathcal{O}(1\ \mathrm{MeV})$) up to more energetic interactions of neutrinos from the LBNF beam ($\mathcal{O}(1\ \mathrm{GeV})$) [1].

In figure 2.8 a DP LArTPC module is reported: not all the detector elements are immersed in liquid, but some components operate in gaseous argon above the liquid. The anode is at the top of the module, in the gas volume; while, the cathode is placed at the bottom with an array of PDs underneath it. The DP module is designed as a single active volume, this would reduce the quantity of non-active

Figure 2.6: A schematic view of an APA (top). A single APA for the ProtoDUNE-SP (bottom) [1].

material in LAr, but due to a longer drift length a higher voltage is required on the cathode with respect to the SP module. The DP technology is based on an operating principle, shown in figure 2.9, similar to the SP LArTPCs. The charged particles passing through the active volume ionize the argon and also produce scintillation light. The ionization charges are drift vertically in LAr toward the anode by a high electric field of 500 V/cm, corresponding to a cathode HV of 600 kV. Before ionization electrons deposit their charge on the anode, they reach an extraction grid where an electric field, stronger than the drift field, extracts the electrons from the liquid up to the gas phase. In the argon gas, large electron multipliers (LEMs) devices amplify the electrons in avalanches before they reach the horizontal anode that provides the x and y coordinate of the event. The amplification in the gas phase increases the S/N ratio by at least a factor of ten, allowing to reach a finer readout granularity and significantly improve the quality of the event reconstruction [26]. The anode consists of two sets of gold-plated copper strips, and together with LEM and the extraction grid they form a three-layered

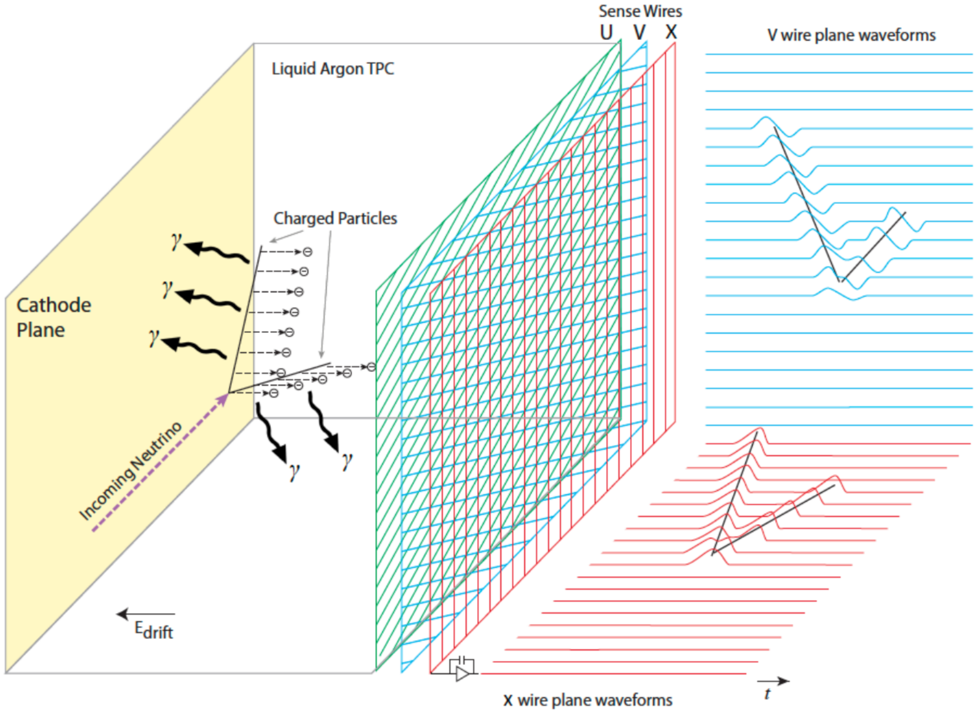

Figure 2.7: The general operating principle of the single-phase LArTPC. Ionization electrons produced in a neutrino interaction drift horizontally under the electric field in the LAr. The ionization charges are collected on the anode, which is made up of the U, V and X sense wires. The photon signal will provide the initial start time of the event. The time projections in two dimensions are represented in the right-hand side [1].

sandwiches, connected horizontally into 9 m^2 modular detection units. These composite units allow to have an adjustable charge gain and two independent, orthogonal readout position measurements [1]. The scintillation light is recorded by an array of photomultiplier tubes (PMTs) at the bottom of the cryostat below the cathode. The PMTs are coated with a wavelength-shifting material to have the light shifted closer to the visible spectrum. The time and pulse of the incident photons are measured and used to reconstruct the event.

Both the SP and DP designs are characterized by a field cage that surrounds the active volumes and ensures the uniformity of the electric field to 1% within that volume. In addition, the performance of both the technologies is highly dependent on the LAr purity and the low noise level of the readout electronics. The LAr purity needs to be high enough to have as low as possible the charge attenuation over the longest drift lengths in the modules, while the very low noise level is necessary to be able to clearly distinguish the signal from the drifting electrons

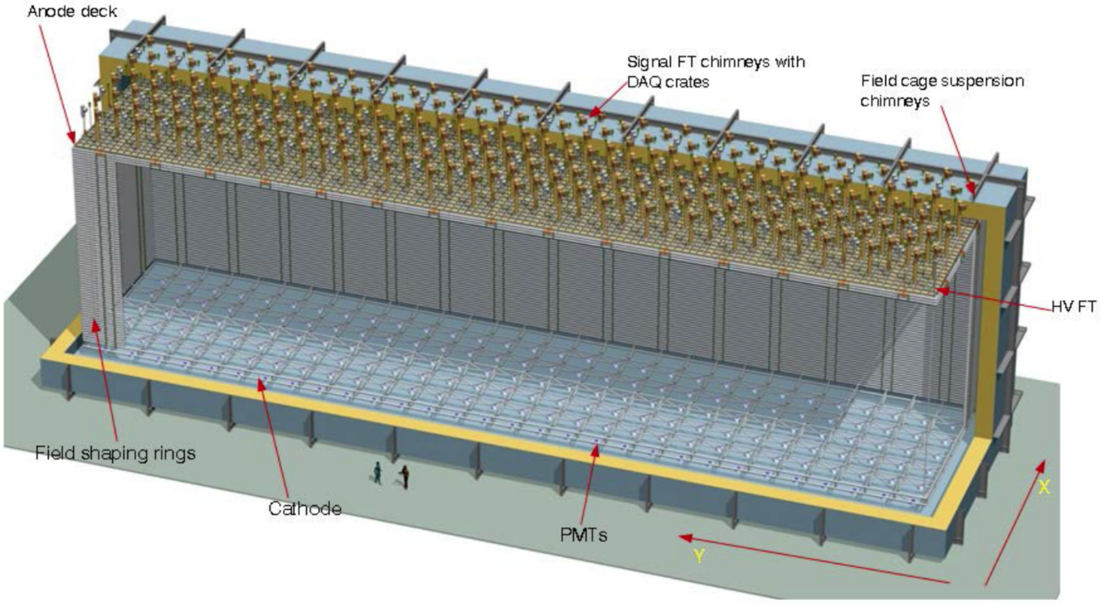

Figure 2.8: Schematic view of a DUNE FD dual-phase module [1].

over the baseline electronics [26].

2.2.2 FD simulation and expected event rate

A FD full simulation, reconstruction and event selection have been performed to analyze the FD reconstruction performances [29]. For this study, since there is not a finalized design of all the four FD modules, single-phase LArTPC technology is assumed for all of them. A full simulation chain is developed using the neutrino flux from a GEANT4-based [30] simulation of the LBNF beamline, the version 2.12.10 of GENIE [4] neutrino interaction generator, and a GEANT4-based detector simulation, which provides particles propagation, detector response and readout of the ionization electrons and scintillation photons. Then, the raw detector signals are processed and reconstruction algorithms are applied. A complete description on the event simulation and reconstruction can be found in [26].

The event classification is performed through the implementation of a convolutional visual neural network based on image recognition techniques. The energy of the neutrino in CC events is estimated by adding the reconstructed lepton and hadronic energies from reconstructed particles produced in neutrino interaction. If the event is identified as CC ν_μ, the neutrino energy is computed as the sum of the longest reconstructed track energy and the hadronic energy. Where the latter is derived from the energy associated to hits not included in the longest track. If

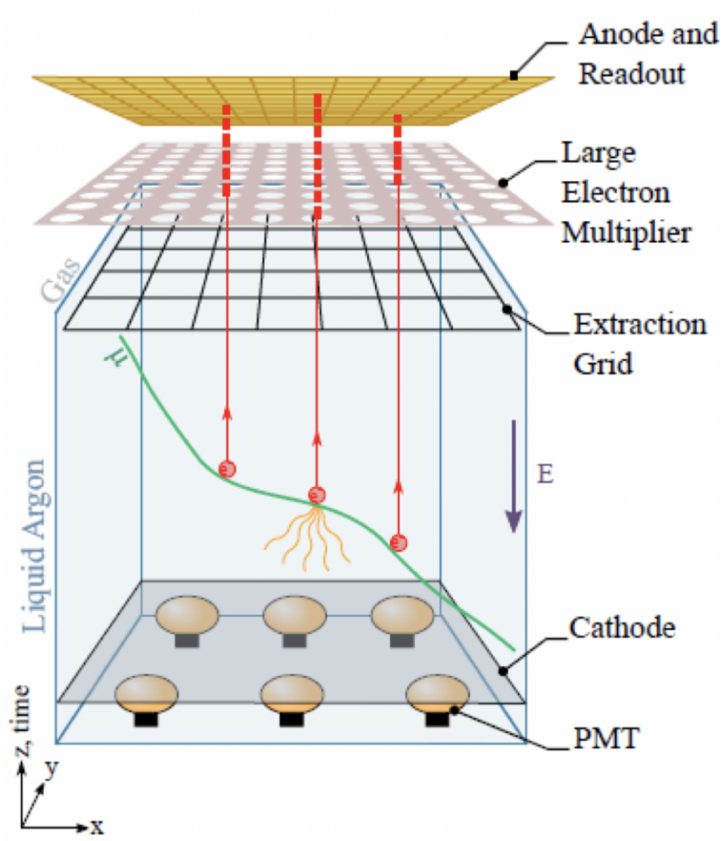

Figure 2.9: The general operating principle of the dual-phase LArTPC. Ionization electrons produced in a neutrino interaction drift vertically under the electric field in the LAr. The ionization charges are transferred into a layer of argon gas above the liquid, where the charge is deposited on the anode. The scintillation photons are collected at the bottom by PMTs [1].

the event is identified as CC ν_e, the neutrino energy is estimated as the sum of the energy of the reconstructed electromagnetic shower with the highest energy and the hadronic energy. In both cases additional simulation-based corrections are applied for missing energy.

Reconstructed energy distribution of ν_e and $\overline{\nu}_e$ CC-like events and ν_μ and $\overline{\nu}_\mu$ CC-like events, selected by the convolutional neural network algorithm, are computed for different δ_{CP} true values and are reported in figures 2.10 and 2.11, respectively. For both the figures, the distributions are obtained assuming $1.1{\cdot}10^{21}$ protons on target per year, 3.5 years of exposure to a neutrino-beam in FHC mode (plots on the right) and 3.5 years of running with an antineutrino-beam in RHC mode (plots on the left) [29]. As shown in figure 2.10, the backgrounds to appear-

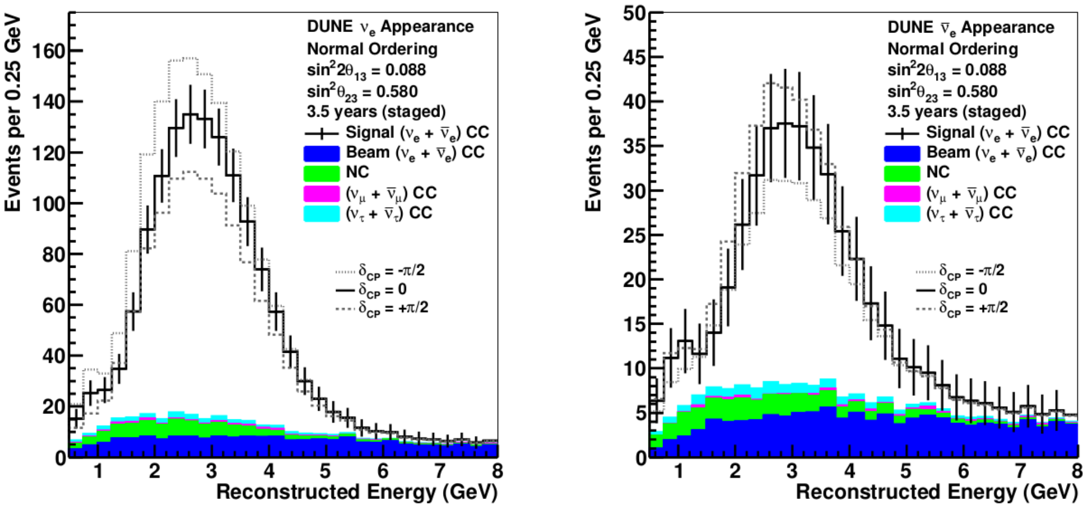

Figure 2.10: Reconstructed ν_e and $\overline{\nu}_e$ disappearance spectra for CC-like events assuming 3.5 years of exposure to a neutrino-beam obtained in FHC mode and 3.5 years of exposure to an antineutrino-beam in RHC mode. Normal mass ordering is assumed. Curves for $\delta_{CP} = -\pi/2, 0, \pi/2$ are plotted [29].

ance event rates are due to CC interactions of ν_e and $\overline{\nu}_e$ intrinsic contaminations of the beam, misidentified NC interactions, misidentified ν_μ and $\overline{\nu}_\mu$ CC interactions and ν_τ and $\overline{\nu}_\tau$ CC interactions. While, as it can be seen in figure 2.11, the backgrounds to disappearance event rates are due to wrong-sign muon (anti)neutrino CC interactions and NC interactions.

2.2.3 DUNE Prototypes

The DUNE collaboration has constructed at CERN two large prototypes detectors, ProtoDUNE-SP and ProtoDUNE-DP in order to validate the design with detector performance, to demonstrate long-term operational stability and to confirm the choice of the materials [26]. The prototypes have a reduced size with respect to the planned FD modules, but they operate with components of the same size to those designed for the DUNE FD. Both the ProtoDUNE-SP and ProtoDUNE-DP cryostats have been installed in the CERN Neutrino Platform in CERN's North Area.

The ProtoDUNE-SP collected data of hadron beam and cosmic rays during the fall of 2018 and it continues to operate on cosmic rays data. A reconstructed event of a test-beam π^+ interacting inside ProtoDune-SP is shown in figure 2.12. The ProtoDUNE-DP started to operate in semptember 2019.

The ProtoDUNE-SP detector has an active volume of $7.2 \times 6.0 \times 6.9$ m^3 with a

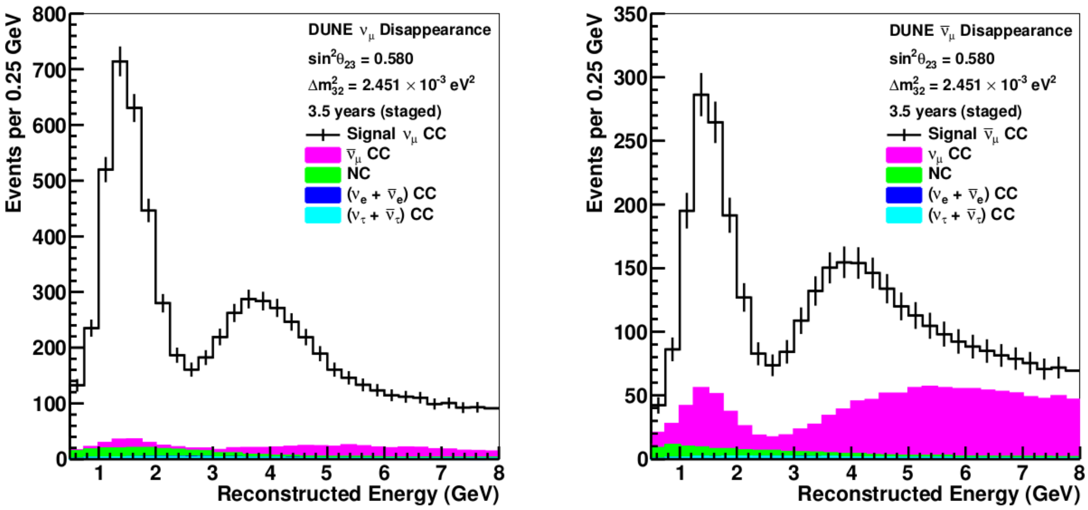

Figure 2.11: Reconstructed ν_μ and $\overline{\nu}_\mu$ disappearance spectra for CC-like events assuming 3.5 years of exposure to a neutrino-beam obtained in FHC mode and 3.5 years of exposure to an antineutrino-beam in RHC mode. Normal mass ordering is assumed [29].

maximum drift length of 3.5 m equal to the future full SP module. The used hadron beam delivers charged pions, kaons, protons, muons and electrons with momenta between 0.3 GeV/c and 7 GeV/c. The beam run provided a high quality data for detector performance characterization, in which were included noise and gain measurements, dE/dx calibration for muons, protons, pions and electrons, drift electron lifetime measurements, and photon detection noise, signal sensitivity and time resolution measurements. First results [32] on ProtoDUNE-SP performances demonstrate the excellent capability and effectiveness of the SP design suited for the DUNE FD purposes.

2.3 The Near Detector

The DUNE near detector will be located 574 m far from the target and 62 m underground in the DUNE ND hall, shown in figure 2.13. The ND complex has three primary detector components: a Liquid Argon Time Projection Chamber (ND-LAr) also referred as ArgonCube, a magnetized Gas Argon Time Projection Chamber (ND-GAr) called the multi-purpose detector (MPD), and the System for on-Axis Neutrino Detection (SAND). According to the DUNE Precision Reaction-Independent Spectrum Measurement (DUNE-PRISM) program, the ND-LAr and ND-GAr can be moved sideways to perform off-axis measurements. The capabil-

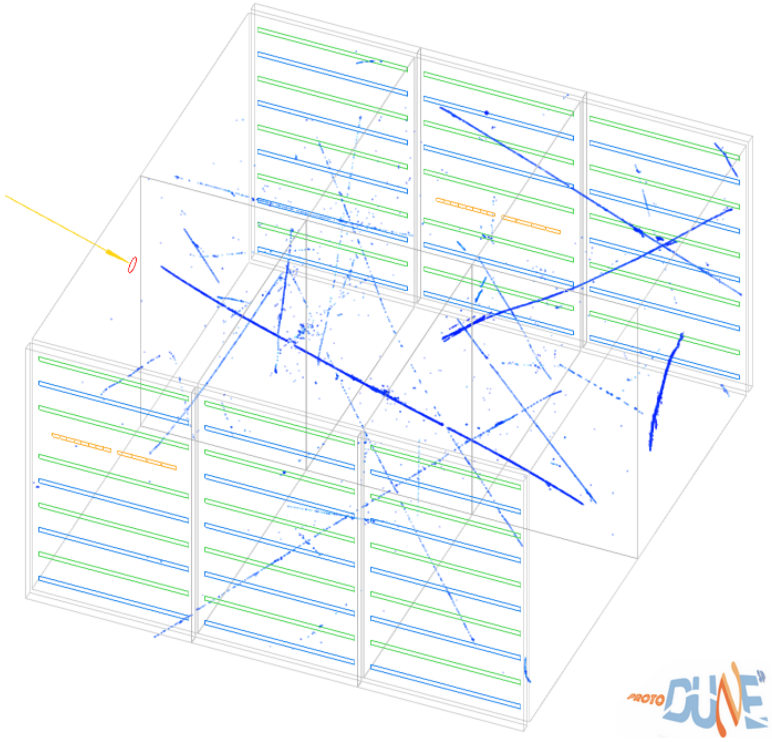

Figure 2.12: Reconstructed event of a test-beam π^+ interaction inside ProtoDUNE in coincidence with cosmic ray muons interactions. Beam direction is indicated by the yellow arrow [31].

ity to move off-axis will allow to study neutrino interactions with different energy spectra at different off-axis locations. It is planned that these two detector components will spend the 50% of the time off-axis, while SAND is the only component permanently on the beam axis, located in a dedicated alcove in the ND hall, to monitor the beam changes with the required sensitivity, constrain systematics and provide a rich neutrino physics program.

The total neutrino event rate expected at the ND is ~ 0.14 events/ton/spill and the total number of ν_μ CC events/year/ton $\cong 1.6 \cdot 10^6$. These values are obtained assuming approximately $7.5 \cdot 10^{13}$ protons extracted every 1.2 s at 120 GeV proton energy and a corresponding protons-on-target (POT) per year of $1.1 \cdot 10^{21}$ POT/year for an accelerator complex efficiency of 57% [27].

2.3.1 The need for the ND

Late LBL experiments exploit a near detector close the beam source in order to measure the unoscillated neutrino spectrum parameters. Assuming the three neu-

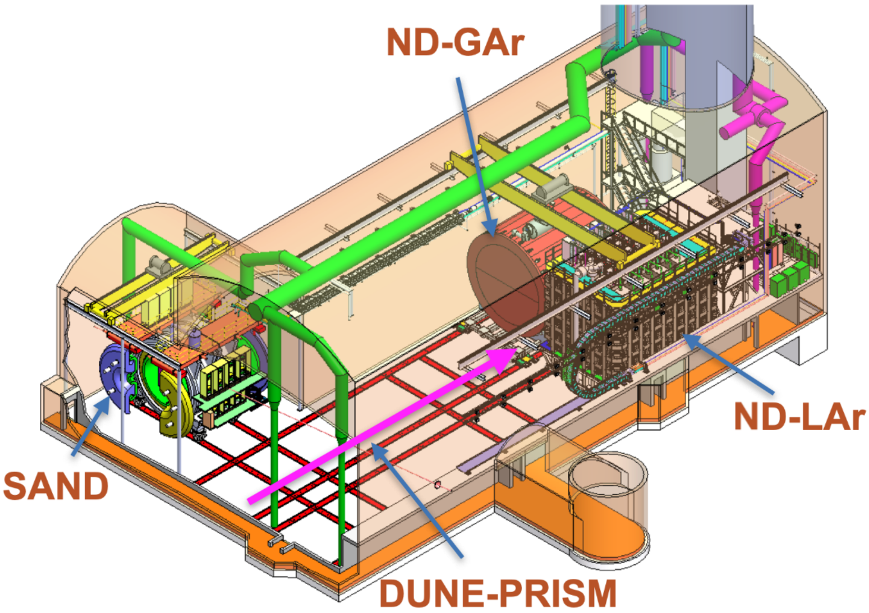

Figure 2.13: Schematic view of the ND hall with the three detector components. The ND-LAr and ND-GAr are in the off-axis configuration [3].

trino model, the near detector provides a measurement of the initial unoscillated interaction rate, while the neutrino interaction rate after oscillations is measured at the far detector. A comparison between the observed event spectrum at the FD and the spectrum estimate based on the ND measurements enables the extraction of oscillation probabilities and the estimation of the oscillation parameters [3]. Thus, the DUNE ND will measure the initial unoscillated ν_e, ν_μ, $\overline{\nu}_e$ and $\overline{\nu}_\mu$ energy spectra from which the spectra at the FD is predicted.

Moreover, the ND is required to understand and constrain many systematic uncertainties, for example due to imperfect modeling of neutrino-nucleus cross-sections, nuclear smearing and beam flux. The ND should also estimate the impact of these systematic effects on the oscillation analysis [27].

On top this, DUNE ND serve as experiment's control, it will also operate for its own physics program, performing precision measurements of neutrino cross-sections and searching for additional BSM signatures, such as sterile neutrinos, NSIs and light-mass DM particles.

2.3.2 The requirements for the ND and the physics program

The ND complex plays a crucial role for the DUNE experiment since it must be able to provide detailed constraints for all the systematic uncertainties relevant for the neutrino oscillation program. In order to enable the DUNE experiment to achieve its primary goals, in particular the precision measurements of oscillation parameters including the undiscovered CP-violating phase, the ND must satisfy the key requirements that follow [3].

- Predict the neutrino energy spectrum at the FD. As primary requirement in the context of neutrino oscillation measurement, the ND must estimate the expected number of neutrinos of each flavor and their reconstructed energy at the FD as function of the oscillation parameters. The systematic uncertainties associated to these predictions must be small enough to achieve the required 5σ sensitivity to CP violation after ten years of exposure.
- Monitor the beam, to detect spectral variations. The on-axis neutrino flux must be continuously monitored to detect representative changes in the beam line.
- Measure the neutrino energy in CC interactions.
- Measure the neutrino fluxes as function of the energy and flavor. This would allow to measure the neutrino cross-sections, to constrain the beam model and to extrapolate the neutrino spectra to the FD.
- Measure interactions in argon. The use of a target nucleus similar to the FD, based upon LAr technology, would allow to reduce (anti)neutrino-nucleus cross-sections and detector systematic uncertainties.
- Constrain neutrino cross-section model.

At the ND and FD, the neutrino interaction rate will be determined as function of the reconstructed neutrino energy. Different convoluted elements contribute to the event rate measurement which can be formalized as

$$\frac{dN^{FD}_{\nu_x}}{dE_{rec}}(E_{rec}) = \int \Phi^{FD}_{\nu_\mu}(E_\nu)P_{\nu_\mu\rightarrow\nu_x}(E_\nu)\sigma^{Ar}_{\nu_x}(E_\nu)R_{phys}(E_\nu, E_{vis})R_{det}(E_{vis}, E_{rec})dE_\nu \tag{2.3.1}$$

$$\frac{dN^{ND}_{\nu_x}}{dE_{rec}}(E_{rec}) = \int \Phi^{ND}_{\nu_x}(E_\nu)\sigma^{m}_{\nu_x}(E_\nu)R_{phys}(E_\nu, E_{vis})R_{det}(E_{vis}, E_{rec})dE_\nu \tag{2.3.2}$$

where

- $x = e,\ \mu$;
- m is the target material (e.g., H, C or Ar)
- E_ν is the true energy of neutrino;

- E_{rec} is the reconstructed energy of the neutrino;
- E_{vis} is the total energy of the visible final state particles;
- $R_{phys}(E_\nu, E_{vis})$ is the physics response function which accounts for the nuclear smearing that affects the visible final state particles;
- $R_{det}(E_{vis}, E_{rec})$ is the detector response function;
- $\sigma_x^m(E_\nu)$ is the neutrino interaction cross section;
- $\Phi_{\nu_x}^{FD,ND}$ is the incoming neutrino flux;
- $P_{\nu_\mu \to \nu_x}$ is the oscillation probability.

The event rate for antineutrinos can be similarly formalized. Terms in eq.(2.3.1) and eq.(2.3.2) are folded together and it is not possible to decouple them by using a single detector or nuclear target, but an unfold procedure must be applied. Therefore, the ND has to provide data with enough redundancy and resolution that allows the deconvolution of the different effects which interplay in eq.(2.3.2) and to reduce the systematic uncertainties.

The comparison between observations at the ND and the FD is preformed using a simulation that convolves models of neutrino flux, neutrino interactions, nuclear smearing and detector response. However, the oscillation analysis should not largely depend on MC models corrections, that can introduce biases, and the constraints on the individual factors folded in eq.(2.3.1) and eq.(2.3.2) should primarily rely on in-situ data. For example, the ND environment is characterized by much higher event rates than the FD one. To correct these differences beam simulations based on Monte Carlo (MC) are used. However, uncertainties arise due to inaccuracies in the simulation of the proton beam, target geometry, hadron production, the focusing of the horns, the decay of the hadrons and the material in the beamline [25]. Thus, the beam modeling should rely on beam simulations, but also on-axis and off-axis flux measurements in order to be performed as well as possible.

Precise flux measurements of the different neutrino flavors (ν_μ, $\overline{\nu}_\mu$, ν_e and $\overline{\nu}_e$) can be performed analyzing different complementary physics processes on different nuclear targets. In particular,

- the flux normalization and spectrum can be provided from neutrino scattering on atomic electrons;

- the flux of ν_μ and $\overline{\nu}_\mu$ as function of the neutrino energy can be constrained by studying the *low-ν* scattering process[1];
- the ratio of $\overline{\nu}_\mu/\nu_\mu$ fluxes can be determined from coherent neutrino scattering;
- the ratio of ν_e/ν_μ fluxes from $\nu(\overline{\nu})$ CC interactions [1].

For this purpose the SAND detector is well suited having a low density spectrometer based on a Straw Tube Tracker (STT), an electromagnetic calorimeter and an active LAr target. Its components allow to perform precise measurements of (anti)neutrino interactions on hydrogen and other nuclear targets different from argon. For example:

- using elastic scattering $\nu e \to \nu e$, the absolute ν_μ flux can be derived;
- the relative ν_μ flux for $E_\nu < 0.5$ GeV can be obtained from $\nu p \to \mu^- p \pi^+$ on hydrogen;
- the ratio of $\overline{\nu}_\mu/\nu_\mu$ fluxes can be determined from coherent π^-/π^+ on carbon;
- the ratio of ν_e/ν_μ and $\overline{\nu}_e/\overline{\nu}_\mu$ fluxes are provided from $\nu(\overline{\nu})$ CC interactions in hydrogen [27].

The detector response can be provided by the ND-LArTPC detector which is characterized by a similar Ar target nucleus and analogous technology to the FD. This allow to measure neutrino events in a similar way and to reduce detector and nuclear effects systematics in the extrapolation of flux constraints to the FD.

Moreover, the ND-LArTPC and ND-GArTPC can sample data at different off-axis positions and for increasing off-axis angles the flux spectrum narrows and the mean energy decreases, as shown in figure 2.14. This allow the two detector components to sample different neutrino beam spectra, hence to analyse different neutrino energy distributions. This can favor the deconvolution of beam and cross section models. In addition, the data taken at different off-axis angles gives sensitivity to different parts of the neutrino cross-sections, i.e. to different dominating neutrino interactions. Thus, performing measurements with different spectral exposures using the same beam can enable to constrain the neutrino interaction model. However, a constant on-axis monitor is needed to safeguard that the changes detected in the off-axis fluxes are due to the different off-axis positions and not due to beam changes [3, 1].

---

[1] *Low-ν* scattering processes are events characterized by a low energy transfer to the nucleus, in which case the cross-section is approximately constant with energy and the event rate is proportional to the flux.

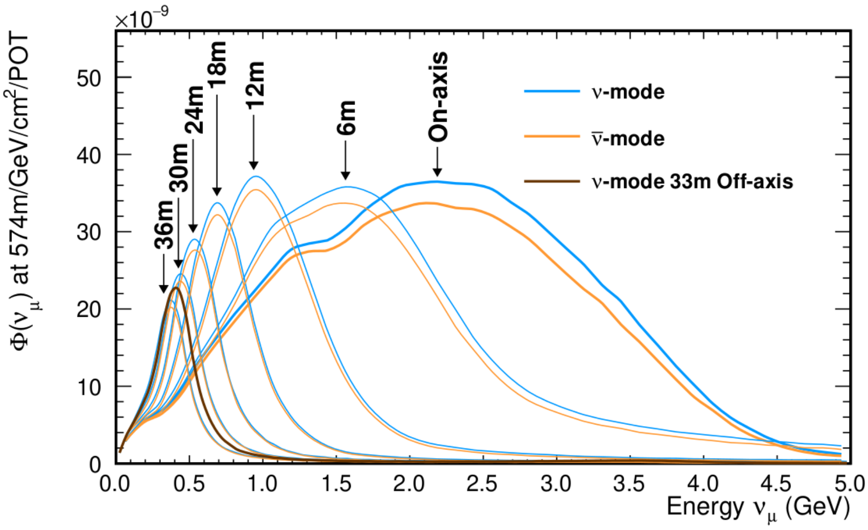

Figure 2.14: Neutrino energy spectra for different detector off-axis positions, assuming the ND 574 m far from the production target [1].

An important source of uncertainty that arises in neutrino interaction models is nuclear smearing. The nuclear effects influence and alter both the initial interaction with the nucleon (cross-sections on free nucleons have large systematics) and the final state particles. This introduces systematic uncertainties for the reconstruction of the (anti)neutrino energy. The argon target is a relatively heavy nucleus which introduces non negligible nuclear smearing. In this context, the SAND detector, which makes use of argon and lighter targets, such as C (graphite) and H (hydrogen) within the tracking system, will allow to study nuclear smearing due to different nuclei and constrain models on nuclear effects [3]. By means of different nuclear targets, SAND will also allow to disentangle the physics response function to the detector one [27].

2.3.3 The ND design

The components of the ND complex address to individual and common functions concerning the multiple missions of the ND that drive the design of these detector components. As introduced before (section 2.3), the ND-LArTPC and the ND-GArTPC detectors can be moved sideway up to 33 m to take off-axis data, while, the SAND detector will stay permanently on the beam axis.

The ND-LArTPC

ArgonCube will consist of 35 separated LArTPC modules that will perform ν-Ar interactions identification using optical timing. Each TPC module is characterized by high voltage cathode, a light collection system, a pixel based charge readout and a field cage optimized to minimize the inactive material between modules. All the modules are immersed in liquid argon and contained within a common cryostat, which is placed on a mobile PRISM platform together with the cryogenics equipment. The ND-LArTPC volume dimension has been chosen to provide good containment of hadrons resulting from neutrino interactions. Using a similar LArTPC technology to the FD, ArgonCube provides the position and energy measurements using the corresponding scintillation light and ionization electrons produced by charged particles passing through the LAr active volume [3]. Since mainly muon (anti)neutrinos of few-GeV energy are expected from the LBNF neutrino beam, at the ND-LArTPC the muon momentum measure is critical. However, the acceptance for muons of the ND-LAr as a standalone detector falls for measured momenta higher than ~ 0.7 GeV/c since they will not be contained in the LAr volume. Hence, a magnetic spectrometer is needed downstream of the ArgonCube to provide this measure. The ND-GArTPC will suite to this purpose with an excellent tracking resolution for muons provided by a lower density medium.

The ND-GArTPC

The ND-GArTPC detector consists of a High-Pressure gaseous argon TPC (HPgTPC) surrounded by an electromagnetic calorimeter, both within a 0.5 T magnetic field provided by a superconductive magnet, and a muon detection system. The HPgTPC is composed by a cylinder filled with an argon-CH4 mixture gas, at a pressure of 10 bar, with a high voltage electrode located at the center of the TPC which provides the electric field for ionization charges to drift towards the end plates of the cylinder, where the signal is amplified for the readout by pad planes. With suitable instrumentation also scintillation light can be used to provide the initial start time of the event. The muon system is still in a very preliminary phase of the design.

ND-GAr will allow to extend the capabilities to measure charged particles energies to lower values with respect to LArTPC and to improve particle identification performances, taking advantage of its deflection in the magnetic field [3].

The SAND detector

A continuous on-axis beam monitoring will be provided by the SAND detector, which is largely based on the reuse of the electromagnetic calorimeter (ECAL) and of the superconducting magnet from the KLOE experiment. The ECAL is a sampling calorimeter, made of lead layers and scintillating fibers and it is composed of a barrel and two endcaps. The SAND inner magnetic volume will contain a target/tracking system based on straw tube planes interleaved with thin carbon and hydrocarbon targets. An active LAr target is also planned in upstream position inside the magnetic volume to study neutrino interactions in Ar that will contribute to constrain the systematic uncertainty in the oscillation data analysis [3]. A more detailed description of the SAND detector can be found in chapter 3.

2.4 Primary goals of the DUNE experiment

2.4.1 Standard neutrino oscillation physics program

The DUNE experiment aims to measure with unprecedented precision the three-flavor neutrino model parameters which govern long-baseline neutrino oscillations using the intense LBNF ν_μ-dominated beam, produced with forward horn current (FHC) polarity, and $\overline{\nu}_\mu$-dominated beam, obtained with reverse horn current (RHC) polarity (see section 2.1).

As described in section 1.3.1 the three-flavor paradigm is an extension of the SM introduced to reconcile theory with observations according to which three neutrino mass eigenstates (ν_1, ν_2, ν_3) are assumed to exist and they are related with the three flavor eigenstates (ν_e, ν_μ, ν_τ) through the mixing matrix:

$$\begin{pmatrix} \nu_e \\ \nu_\mu \\ \nu_\tau \end{pmatrix} = \begin{pmatrix} U_{e1} & U_{e2} & U_{e3} \\ U_{\mu 1} & U_{\mu 2} & U_{\mu 3} \\ U_{\tau 1} & U_{\tau 2} & U_{\tau 3} \end{pmatrix} \quad \begin{pmatrix} \nu_1 \\ \nu_2 \\ \nu_3 \end{pmatrix}. \tag{2.4.1}$$

If neutrinos are assumed to be Dirac particles, the mixing matrix in eq.(2.4.1) becomes the one already seen in eq.(1.3.2) and it can be parametrized by four parameters defined as

$$\begin{aligned} \sin^2\theta_{12} &\equiv \frac{|U_{e2}|^2}{1-|U_{e3}|^2}, \\ \sin^2\theta_{23} &\equiv \frac{|U_{\mu 3}|^2}{1-|U_{e3}|^2}, \\ \sin^2\theta_{13} &\equiv |U_{e3}|^2, \\ \delta_{CP} &\equiv -\arg(U_{e3}). \end{aligned} \tag{2.4.2}$$

The main task is to validate the three-flavor massive neutrino model by reaching enough sensitivity to perform unambiguous measurements of δ_{CP} and mass ordering, and to obtain refined measurements of the oscillation parameters. The definitive mass ordering determination would be provided by a measure of Δm^2_{31} with its sign. Moreover, a particular consideration concerns the observation of CP violation in lepton sector, since it could take part in the explaination of the baryon and anti-baryon asymmetry in the Universe. In fact, the violation of CP invariance is one of the necessary ingredients of any possible theory of baryogenesis. In particular, one hypothesized mechanism, called leptogenesis, could be able to relate and explain both the mass of neutrinos and the matter preponderance over antimatter in the early universe [26].

For this purpose, the DUNE experiment has been designed to be sensitive to the mixing angles θ_{13} and θ_{23}, the mass-squared difference Δm^2_{31} and the CP violating phase δ_{CP}. These parameters can be derived by the oscillation probabilities inferred from a coordinated analysis of the reconstructed ν_μ, $\overline{\nu}_\mu$, ν_e and $\overline{\nu}_e$ fluxes. In particular, the oscillation measurements of the disappearance channels $\nu_\mu \to \nu_\mu$ and $\overline{\nu}_\mu \to \overline{\nu}_\mu$ are sensitive to $|\Delta m^2_{31}|$ and $\sin^2 2\theta_{23}$, while measurements of the appearance channels $\nu_\mu \to \nu_e$ and $\overline{\nu}_\mu \to \overline{\nu}_e$ are sensitive to $\sin^2 2\theta_{13}$, $\sin^2\theta_{23}$, Δm^2_{31} and δ_{CP} [33]. Direct observation of ν_τ appearance is less taken in consideration because the threshold for τ production in ν_τ CC interactions is greater than the energies at which oscillation maxima occur [1].

From current data, the angle θ_{23} is known to be close to the maximal-mixing value $\pi/4$, but it is not defined whether its value is in the lower octant ($\theta_{23} < \pi/4$), in the upper octant ($\theta_{23} > \pi/4$) or equal to $\pi/4$. Since ν_μ disappearance measurement is sensitive to $\sin^2 2\theta_{23}$ and ν_e appearance one to $\sin^2\theta_{23}$, by comparing these measurements the exact value of θ_{23} can be investigated by DUNE. In figure 2.15 is shown the sensitivity to determining the θ_{23} octant as function of the true value of $\sin^2\theta_{23}$ [26].

As far as θ_{13}, the measure of this angle will be performed by DUNE through ν_e and $\overline{\nu}_e$ appearance. This would provide an independent measure of the mixing angle with respect to the measurements performed in reactor experiments, allowing a comparison between them [1].

If the CP invariance is violated, a neutrino-antineutrino asymmetry would be measurable from the appearance channels $\nu_\mu \to \nu_e$ and $\overline{\nu}_\mu \to \overline{\nu}_e$. Hence, these channels can be studied to infer the value of the CP violating phase. However, due propagation through matter, a neutrino-antineutrino asymmetry is introduced not only by CP violation but also by matter effects. For example, the electron neutrino appearance probability through matter in a constant density approximation is at

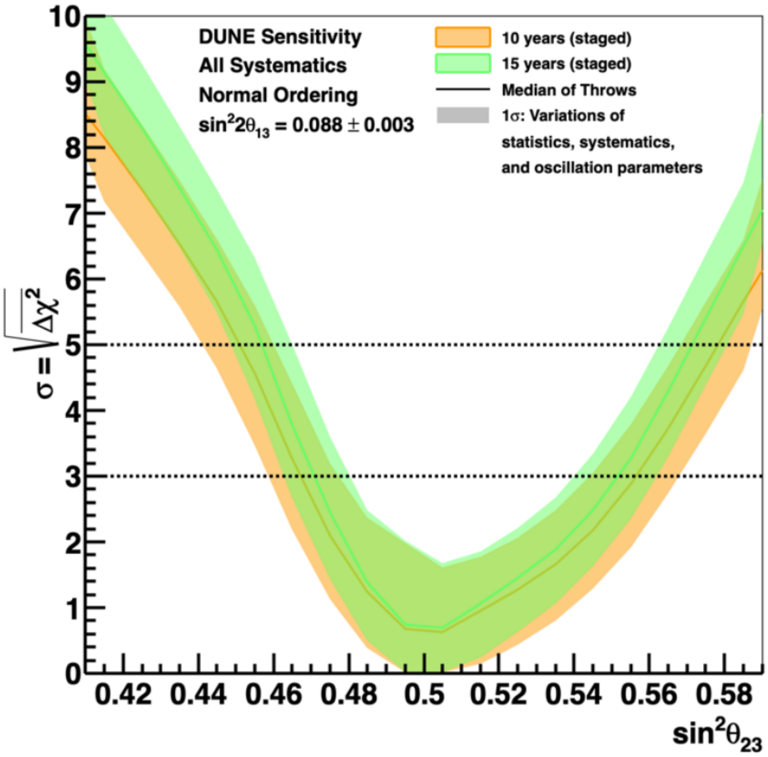

Figure 2.15: DUNE sensitivity to the θ_{23} octant as a function of the value of $\sin^2\theta_{23}$ assuming normal ordering, for different years of exposure: ten (orange) and fifteen (green). The solid lines represents the median sensitivity and the transparent bands cover 68% of fits in which are simulated statistical variations [1].

first order

$$\begin{aligned}P(\nu_\mu \to \nu_e) \simeq\ & \sin^2\theta_{23}\sin^2 2\theta_{13}\frac{\sin^2(\Delta_{31}-aL)}{(\Delta_{31}-aL)^2}\,\Delta_{31}^2\\ &+\sin 2\theta_{23}\sin 2\theta_{13}\sin 2\theta_{12}\frac{\sin(\Delta_{31}-aL)}{(\Delta_{31}-aL)}\Delta_{31}\frac{\sin(aL)}{(aL)}\Delta_{21}\, cos(\Delta_{31}+\delta_{CP})\\ &+\cos^2\theta_{23}\sin^2 2\theta_{12}\frac{\sin^2(aL)}{(aL)^2}\,\Delta_{21}^2,\end{aligned} \tag{2.4.3}$$

where $\Delta_{ij} = \Delta m^2_{ij}L/4E_\nu$, $a = G_F N_e/\sqrt{2}$, N_e is the electron number density in the Earth, L is the baseline in km and E_ν is the neutrino energy in GeV. Whereas, the corresponding appearance probability for electron antineutrinos has the δ_{CP} and a (representing the matter effects) terms that change sign. This means that for the DUNE experiment the neutrino-antineutrino asymmetry

$$\mathcal{A} = \frac{P(\nu_\alpha \to \nu_\beta) - P(\overline{\nu}_\alpha \to \overline{\nu}_\beta)}{P(\nu_\alpha \to \nu_\beta) + P(\overline{\nu}_\alpha \to \overline{\nu}_\beta)} \tag{2.4.4}$$

is the result of a contribution given by the CP violation and a contribution due to matter effects: $\mathcal{A} = \mathcal{A}_{CP} + \mathcal{A}_{matter}$. Moreover, as it can be seen from eq.(2.4.3) matter effect term a introduces a sensitivity to the sign of Δm^2_{31} whose determination would resolve the neutrino mass ordering. Thus, in order to measure the δ_{CP} phase and determine the neutrino mass ordering, CP violation effects must be disentangled from the matter effects.

The baseline length L and the neutrino beam energy E_ν are of great importance for an experiment to have the ability to disinguish between matter effects and CP violation contributions which have approximately the following dependencies

$$\begin{aligned} &\mathcal{A}_{CP} \propto L/E_\nu \\ &\mathcal{A}_{matter} \propto L \times E_\nu \, . \end{aligned} \tag{2.4.5}$$

In figure 2.16 oscillation probability asymmetries as function of the CP violating phase δ_{CP} at the first and second oscillation maxima are shown for different baseline values (290 km, 810 km, 1300 km, 2300 km). The solid lines refers to the normal ordering first (black) and second (red) oscillation nodes, while, dashed lines represents inverted ordering nodes. For short baselines, if the mass ordering is not known, the experimental measurement of the asymmetry at the first oscillation maximum would give ambiguous information about the CP violating phase. In fact, considering the plot for a baseline of 290 km, a possible asymmetry measurement at $\delta_{CP} = -\pi/2$ (inverted ordering) is degenerate with that at $\delta_{CP} \sim 0$ (normal ordering), as indicated by the green line. Differently, for baselines longer than ∼1200 km the matter asymmetry exceeds the maximal possible CP asymmetry, the experiment would be more sensitive to the neutrino mass ordering and the degeneracy can be resolved [25]. Thus, the DUNE baseline of ∼1300 km allow to disentangle between matter effect and CP asymmetries.

In figure 2.17 the electron neutrino and antineutrino appearance probabilities are shown as function of the neutrino energy at a baseline length $L = 1300$ km for $\delta_{CP} = -\pi/2$, 0, $\pi/2$, assuming normal ordering. It can be seen that the amplitude and the phase of the oscillation are affected by different values of the CP violating phase and the difference caused in the amplitude is larger at higher oscillation nodes that correspond to energies less than 1.5 GeV.

Therefore, relying on the arguments above, the DUNE experiment with a baseline of ∼1300 km and the ability to study the spectrum of oscillations over a wide range of energies will be able to search for CP violation and determine the mass ordering simultaneously in a single experiment.

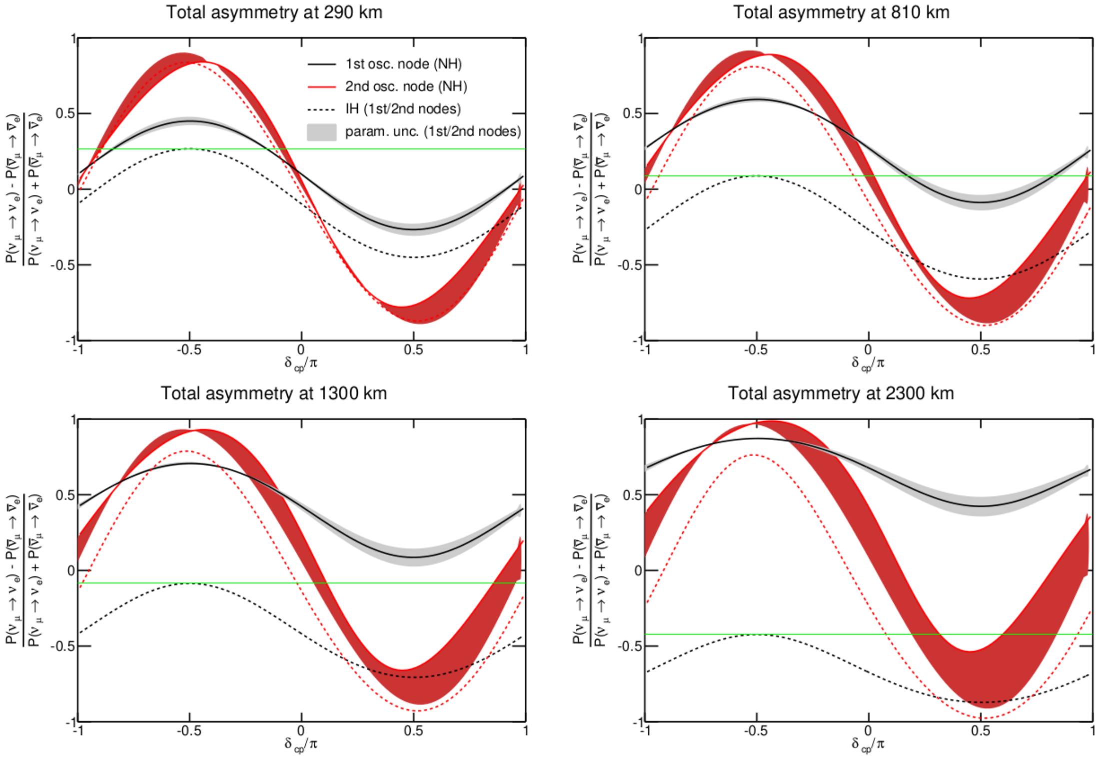

Figure 2.16: Oscillation asymmetries for the two probability oscillation maxima as a function of CP violating phase for different values of the baseline: 290 km, 810 km, 1300 km and 2300 km. Black lines indicate the first maximum, the red ones the second maximum. The solid lines represents the nodes for the normal ordering, the dashed ones refers to the nodes for inverted ordering [25].

In figure 2.18 are illustrated the DUNE significances for the CP violation and mass ordering determination as function of exposure in years. Over more than 75% of the possible δ_{CP} values range, it is expected to obtain a sensitivity of better than three standard deviations (3σ) after five years and better than 5σ after ten years. Moreover, DUNE is expected to determine the neutrino mass hierarchy after two/three years of running with a 5σ significance for 100% of δ_{CP} possible values.

2.4.2 Search for proton decay

The proton decay is a phenomenon expected by Grand unified theories (GUTs) that would explicitly break the Baryon number conservation. GUTs extend the SM by attempting to describe the three gauge fundamental interactions (strong, weak and electromagnetic) as different low energy manifestations of a single underlying

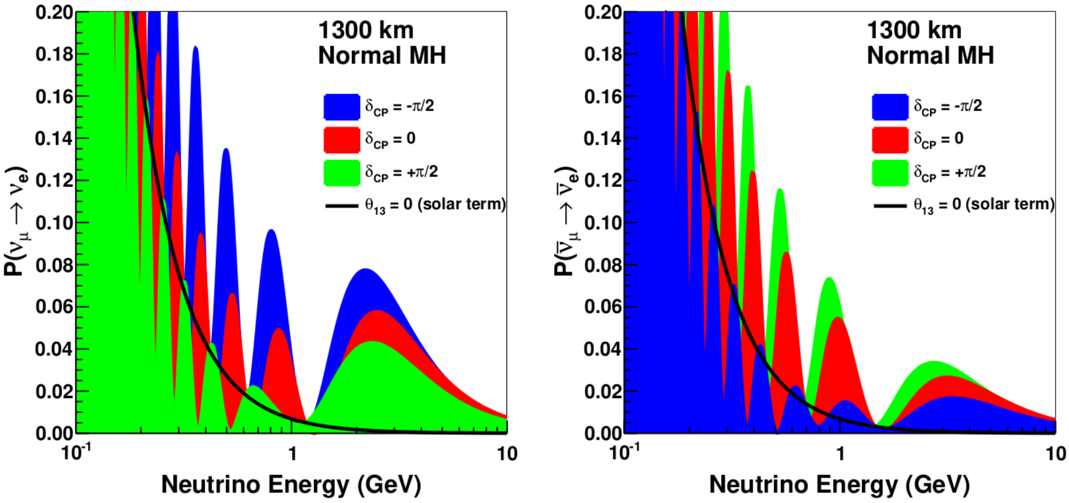

Figure 2.17: electron neutrino (left) and antineutrino (right) appearance probability, $P(\nu_\mu \to \nu_e)$ and $P(\overline{\nu}_\mu \to \overline{\nu}_e)$, as function of neutrino energy, at a baseline of 1300 km, for different values of $\delta_{CP} = -\pi/2$ (blue), 0 (red) and $\pi/2$ (green). Normal ordering is assumed. The black line refers to the oscillation probability for $\theta_{13} = 0$ [26].

gauge symmetry at very high energies ($> 10^{15}$ GeV). Different reasons encourage GUT models, such as gauge-coupling unification and their capability in solving the fine-tuning problem of the SM [34]. Observable effects of this unified symmetry are predicted at low energies and one of these is the nucleon decay.

Different experiments have searched for proton decay via different decay channels, among which two very important decay modes are $p \to e^+\pi^0$ and $p \to K^+\overline{\nu}$. Although, no evidence have been found and only lifetime limits have been set, most of them by the Super-Kamiokande experiment [35].

Aspects of the DUNE far detector optimized for neutrino oscillation physics are also suited for sensitive searches for nucleon decay: large sensitive mass, excellent imaging, calorimetric and particle identification abilities obtained thanks to the liquid argon time-projection camber (LArTPC) technology. These characteristics will allow the DUNE experiment to access and investigate the rates predicted by GUT models for key nucleon decay channels by reducing the backgrounds below the single-event level and improving the discovery sensitivity for the proton lifetime. The nucleon decay $p \to K^+\overline{\nu}$ is very interesting for the DUNE experiment since it will be able to reconstruct, identify and test for kinematic consistency kaon and its decay products, performing a precision measurement within the energy range of interest sufficient to reject backgrounds due to neutrino interactions and atmospheric muons. DUNE is expected to set 90% CL lower limit to $1.3{\cdot}10^{34}$ years

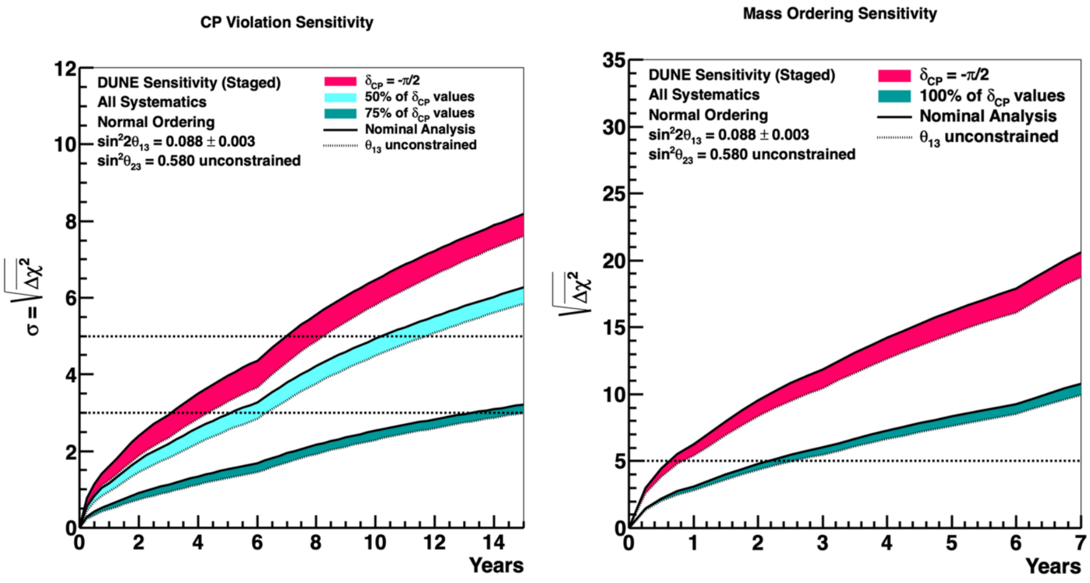

(a) (b)

Figure 2.18: DUNE significance of (a) the CP violation and (b) the neutrino mass ordering determinations as function of the years of running for different cases of δ_{CP}. Figure (a) shows CP violation sensitivity for δ_{CP} equal to $-\pi/2$ and in the 50% and 75% of the possible values range; figure (b) reports mass ordering sensitivity for δ_{CP} equal to $-\pi/2$ and for 100% of the possible true values range. Normal ordering is assumed. The width of the band represents the impact of an external constraint in $\sin^2 2\theta_{13}$ [26].

in proton lifetime divided by branching fraction for 400 kt·year exposure [26].

2.4.3 Supernova neutrino bursts

DUNE will be able to collect and analyze a possible neutrino signal from a SN within the Milky Way. The study of neutrino bursts emitted from the SN will allow to have an insight into explosion phenomenon and formation of the remnant neutron star or black hole.

The core-collapse SN starts because the gravitational pressure of the star is no longer opposed by radiation pressure. Due to the increasing pressure the infalling matter bounce and a shock wave is driven into the outer core, triggering the supernova explosion. The beginning of the collapse is characterized by a short, sharp neutronization (or break-out) burst mainly composed of ν_e and with a time duration of $\Delta t \sim \mathcal{O}(10\text{ ms})$. The burst is due to the shock front breaking through the neutrinosphere (region of the star in which the neutrinos are trapped before the propagation of the shock). The neutrino carry away most of the total energy liberated and the shock weakens. Then, during the *accretion phase*, after the core bounce, a remnant forms and it rapidly grows as matter falls onto the collapsed core. During this phase, lasting $\Delta t \sim \mathcal{O}(100\text{ ms})$, ν_e and $\overline{\nu}_e$ are produced. Then, in the *cooling phase* the core further loses most of its gravitational potential energy through neutrino-pair production of all three lepton flavors. This neutrino signal, produced during the cooling, lasts $\Delta t \sim \mathcal{O}(10\text{ s})$.

After the supernova explosion, depending on the mass of the progenitor star, the remnant can become a neutron star (if the progenitor mass is below $\sim 25\text{ M}_\odot$) or collapse into a black hole [18].

The exact mechanism of the supernova evolution and the crucial ingredients taking part to the explosion are still unclear and controversial. However, interesting information can be obtained studying neutrino signal, since the start of the collapse can be recognized by a short breakout burst and simulations suggest that the most of the gravitational potential energy is lost as neutrino kinetic energy. Thus, neutrinos play a fundamental role and they can be used to follow the evolution of the SN throughout its different phases.

The world current experiments that study SN neutrinos are primarily characterized by water Cherenkov or organic scintillator detectors which are most sensitive to $\overline{\nu}_e$ flavor. In this context, the DUNE experiment with LArTPC technology will have a particular sensitivity to ν_e via the CC absorption of ν_e on ^{40}Ar:

$$\nu_e + {}^{40}\text{Ar} \rightarrow e^- + {}^{40}\text{K}^* \; ; \tag{2.4.6}$$

providing a unique opportunity to study the neutronization bursts. Other relevant channels for the study of SN neutrinos are $\overline{\nu}_e$ CC interactions, elastic scattering on electrons and NC scattering on Ar nuclei [26].

From supernova models, several thousand of neutrino interactions over a time interval of up to few tens of seconds are expected in the DUNE FD due to SN explosion in the center of the Milky Way. The energy spectrum is expected to range around few tens of MeV up to about 30 MeV [1].

Chapter 3

System for on-Axis Neutrino Detection

The System for on-Axis Neutrino Detection is one of the three detector components of the DUNE near detector. It will continuously monitor the beam on-axis to produce a statistically significant neutrino beam spectrum measurement and detect spectral variations.

SAND is designed to be a multipurpose detector able to detect neutrino interactions on different target materials, including argon and hydrogen, performing precision tracking and calorimetry measurements. In the proposed design, a superconductive solenoidal magnet provides an axial magnetic field in which an electromagnetic calorimeter (ECAL), a tracking system and a liquid Argon target are immersed [3].

The SAND system will reuse the already existing magnet and the ECAL of the concluded KLOE experiment [36]. In figure 3.1 a view of the KLOE ECAL inside the magnet is reported. These two detector components have been used successfully for many years, until March 2018, in the KLOE detector. The concluded experiment was mainly dedicated to the study of the light mesons (kaons and η) decays and strong interactions in the low energy regime at the INFN National Laboratories of Frascati (LNF).

In this thesis the considered design makes use of Straw Tube Tracker (STT) planes interleaved with thin carbon and hydrocarbon layers. The outstanding features provided by this tracking design can significantly enhance the physics sensitivity of SAND and constrain the systematic uncertainties affecting the long-baseline analyses. The final design of the inner tracking system of SAND is still under study.

An active LAr target is also conceived in the upstream region of the ECAL inner volume. It will contribute for inter-calibration within other detectors and to constrain the systematic uncertainty in the oscillation data analysis.

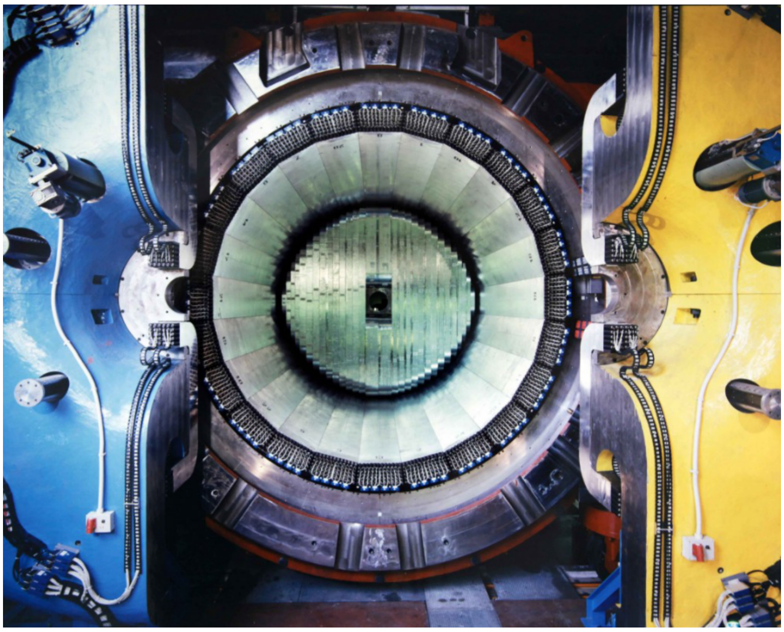

Figure 3.1: A view of the internal volume of the KLOE calorimeter with the near endcap open [36].

3.1 The superconductive magnet

The KLOE superconductive solenoid magnet and iron yoke were designed to produce 0.6 T axial magnetic field over a cylindrical volume (4.3 m long with a diameter of 4.8 m). The return yoke, which has a mass of 475 tons, contains a cryostat characterized by an outer diameter of 5.76 m, an inner diameter of 4.86 m and an overall length of 4.40 m. The coil is positioned inside the cryostat and it is operated at a nominal current of 2902 A [27]. Thermo-siphoning cycles perform the cooling of the coil: gaseous helium at 5.2 K is injected at 3 bar (absolute pressure) from the cryogenic plant and liquefied through Joule-Thompson valves into a liquid He reservoir in thermal contact with the coil. Liquid He is used to directly cool the current leads, while gaseous He at 70 K from the cryogenic plant is used to cool the radiation shields [3].

3.2 The electromagnetic calorimeter

The KLOE electromagnetic calorimeter is a sampling calorimeter made of lead layers and scintillating fibers and it provides a coverage of $\sim 98\%$ of 4π. It is composed of a barrel and two endcaps. The endcaps are divided into two halves to allow the opening of the structure and to access to the inner volume. A schematic

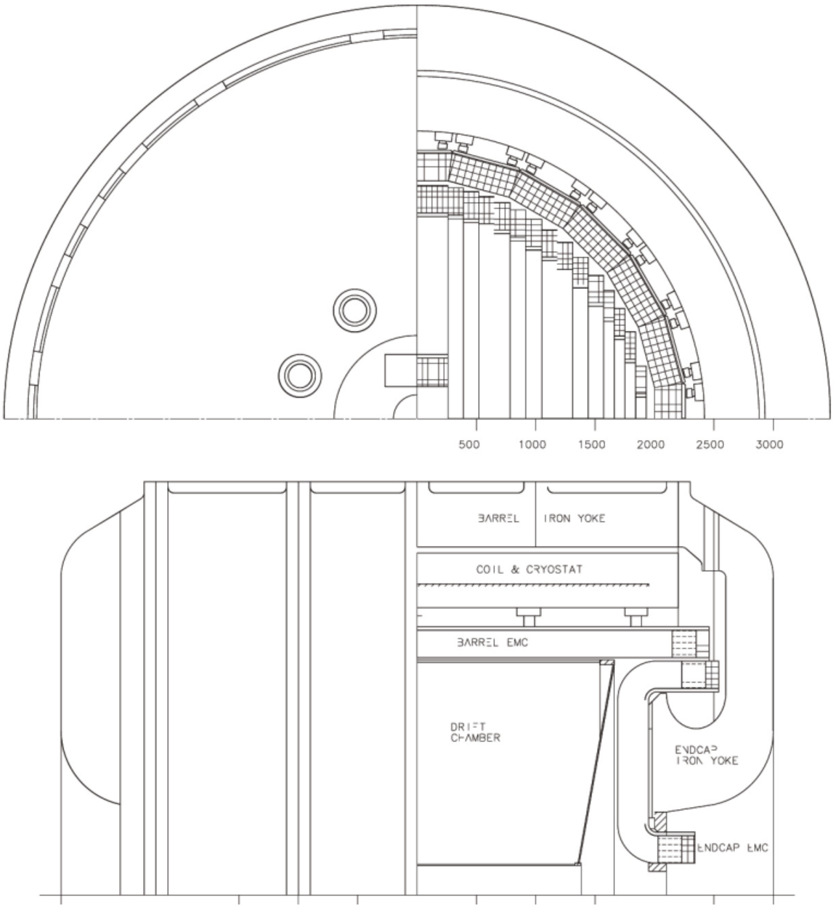

Figure 3.2: A front (top) and vertical (bottom) cross section views of the KLOE detector with the ECAL and the magnet [3].

layout of the KLOE calorimeter and magnet is reported in figure 3.2.

The barrel is almost cylindrical and it is divided into 24 modules which can be seen in figure 3.3. These modules are 4.3 m long, 23 cm thick and they have a trapezoidal cross-section characterized by two bases of 52 and 59 cm. The modules are attached to the coil cryostat inner wall and they are bent at the upper and lower ends to allow insertion into the barrel.

The endcaps are C-shaped in order to provide a better solid angle coverage. Each endcap consists of 32 modules 0.7-0.9 m long, 23 cm thick and with a rectangular cross section of variable width.

All the modules of the calorimeter are stacks of about 200 grooved lead foils (0.5 mm thick) alternating with 200 layers in which cladded scintillating fibers (1 mm diameter) are embedded. A schematic layout of an ECAL module is shown in figure 3.4. A special epoxy, not harmful to the fiber materials, is used to glue

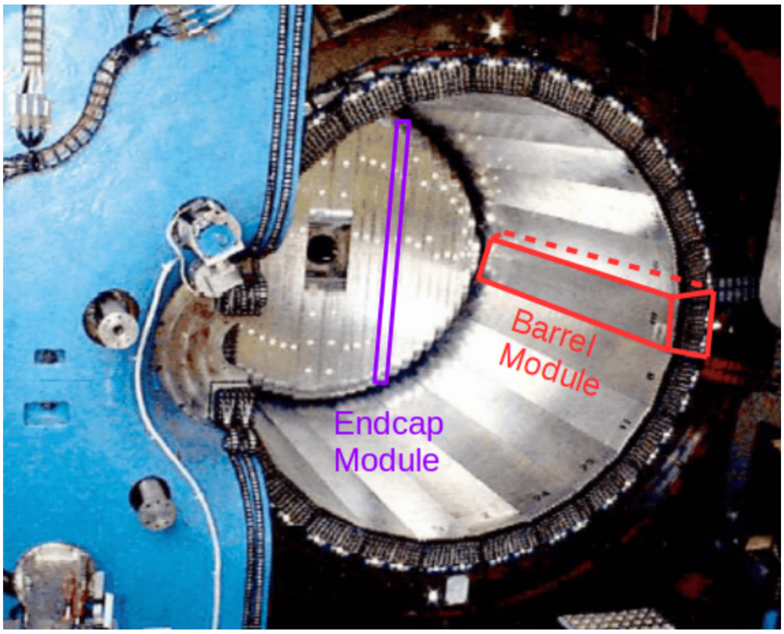

Figure 3.3: A KLOE calorimeter view with the far endcap closed and the near yoke pole piece and endcap open [3].

together the lead foils and the fibers. The volume proportion of lead:fiber:epoxy is 42:48:10, characterized by a high scintillator content, necessary to obtain a good energy resolution. In fact, the scintillating fibers offer several advantages, mainly a good light transmission over several meters, an excellent timing accuracy of sub-ns and a very good hermeticity [3]. Two different types of fibers have been used: Kuraray SCSF-81 fibers, manufactured in Japan, and Pol.Hi.Tech. 0046 fibers, manufactured in Italy, both emitting in the blue region. The former are characterized by higher light output and longer attenuation length and are used in the inner half of the ECAL modules; while, the Pol.Hi-tech. fibers are used for the rest. From tests performed on both types of fiber, the attenuation length results to be between 3-5 m and the light yield to be ∼1 PE/mm for a fiber crossed at 2 m distance from a photo-tube [2].

The average density of the ECAL is 5 g/cm^3, the radiation length is ∼1.5 cm, corresponding to an overall calorimeter thickness of ∼15 radiation lengths.

The readout is segmented in depth into 5 planes, each 4.4 cm deep, except for the outermost, which is 5.2 cm deep. Each plane is subdivided in the transverse direction to the fibers into 4.4 cm wide elements, except at the edges of the trapezoidal modules. This segmentation gives a total number of 2440 segments, called cells, a readout resolution of 1.3 cm ($4.4/\sqrt{12}$ cm) and a total granularity of the ECAL of $\sim 4.4 \times 4.4$ cm^2 [2].

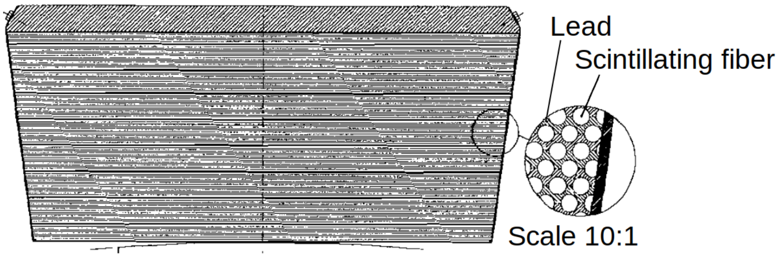

Figure 3.4: Lead and fiber schematic layout [37].

The light from fibers is viewed by photo sensors at both sides of the cells. Thus, each barrel module has 60 readout channels per side and the endcap ones have 10, 15 or 30 channels per side depending on their width. The total number of readout channels is equal to 4880 [2].

The light propagation at both ends of each module is via light guides, illustrated in figure 3.5, that match the almost square portions of the module end-faces to circular photo sensor windows. They are formed by an initial mixing section and terminate with a Wiston cone, providing an area concentration factor of about 4. Small light losses are expected in the large area reduction, since light propagates at small angles with respect to the fiber axis (~22° for light propagating in a plane containing the fiber axis). From KLOE measurements, the overall efficiency of the guides results to be $\sim 80\%$ [2].

Figure 3.5: Light guides at one end of the barrel modules [3].

3.2.1 Reconstruction of time, position and energy

As described before in section 3.2, the readout granularity of the calorimeter is determined by the light collection segmentation into 2440 cells which are read out by photo sensors at each end (in the following referred as sides A and B). The photo sensor readout provides an amplitude signal and a time signal. Thus, for each cell, two amplitude signals, S^A and S^B, and two time signals, t^A and t^B, are recorded. Where the amplitudes $S^{A,B}$ are expressed in ADC counts and $t^{A,B}$ are obtained from the times $T^{A,B}$ in TDC counts using the calibration constants $c^{A,B}$ (ns/TDC counts): $t^{A,B} = c^{A,B} \times T^{A,B}$. The measured scale factors at KLOE experiment were $c \sim 53$ ps/count with an uncertainty of $\leq 0.3\%$ [2].

The arrival time t and the impact point s along the fiber direction are reconstructed as

$$t = \frac{t^A + t^B}{2} - \frac{t_0^A + t_0^B}{2} - \frac{L}{2v} \qquad \text{[ns]} \tag{3.2.1}$$

$$s = \frac{v}{2}(t^A - t^B - t_0^a + t_0^b) \qquad \text{[cm]}, \tag{3.2.2}$$

where $t_0^{A,B}$ are the overall time offsets, L is the cell length (cm) and v is the light velocity (cm/ns) in the fiber [2, 38].

Considering the amplitude signals, the energy signal on each side of a cell i is given by

$$E_i^{A,B} = \frac{S_i^{A,B} - S_{0,i}^{A,B}}{S_{M,i}} \times k_E \qquad \text{[MeV]}, \tag{3.2.3}$$

where $S_{0,i}$ are the offsets of the amplitude scale, $S_{M,i}$ is the response in ADC counts of a minimum ionizing particle incident at the center of the calorimeter and k_E is the overall energy scale factor. During the running of the KLOE experiment k_E was determined studying Bhabha events, its value was ~ 40 MeV/S_M [2]. The signal $S_i^{A,B} - S_{0,i}^{A,B}$ of channel i is divided by $S_{M,i}$, in order to account for the photo sensor response, fiber light yield and electronics gain.

A correction factor $A_i^{A,B}$ is applied to the energy measurements taken at each side in order to take into account the attenuation along the fiber length. Then, the cell energy is obtained as the mean of the determinations at each end,

$$E_i = \frac{E_i^A A_i^A + E_i^B A_i^B}{2} \qquad \text{[MeV]}. \tag{3.2.4}$$

The calorimeter was calibrated with cosmic muons and photons from e^+e^- collisions before and during the KLOE running. Moreover, the calorimeter performances were tested during the commissioning and running phases of KLOE experiment and the energy and time resolutions were found to be [2]

$$\sigma_E/E = 5.7\%/\sqrt{E(\text{GeV})}, \tag{3.2.5}$$

$$\sigma_t = 54/\sqrt{E(\text{GeV})} \qquad [\text{ps}]. \tag{3.2.6}$$

The time resolution has been evaluated using different data samples characterized by $\Phi \to \eta\gamma$, $\Phi \to \pi^0\gamma$ and $e^+e^- \to e^+e^-\gamma$ events [39]. The energy response and resolution have been determined using $e^+e^- \to e^+e^-\gamma$ events, shown in figure 3.6. The response was found to be linear at better than 1% for $E_\gamma > 75$ MeV [2].

After installation in the ND hall at Fermilab, in situ checks on the ECAL will be taken using muon cosmic rays, stopping particles, neutral pions, etc. [3].

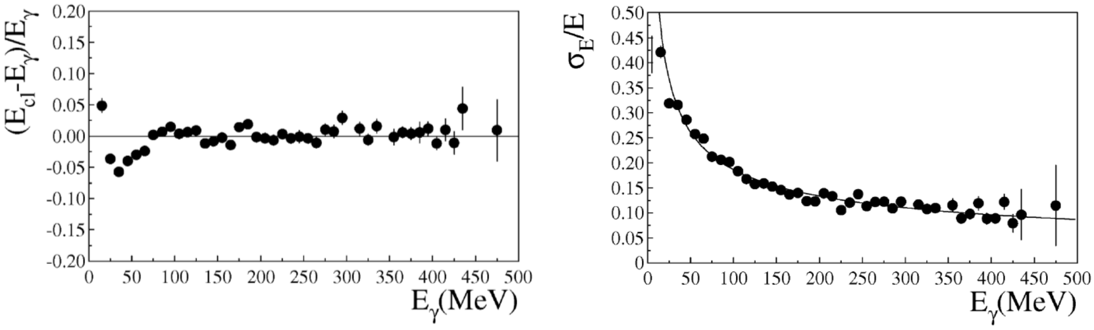

Figure 3.6: Energy linearity (left) and resolution (right) of the KLOE calorimeter obtained studying radiative Bhabha events during the running of the KLOE experiment [39].

3.3 The tracking system

Most of the magnetic inner volume inside the ECAL will be filled by STT modules, except for the upstream region, which will be instrumented with a LAr target (see section 3.4).

In the following, a description of the STT tracking system is reported, further details are outlined in ref.[27].

The tracking system will act as the target for the (anti)neutrino interactions and it will provide precise measurements of all charged particles momenta. In particular, according to the physics needs of the long-baseline oscillation analysis, the tracker is required to guarantee (a) low density and high track sampling to momentum, angular and space high resolutions; (b) small total thickness to minimize secondary interactions; (c) capability to accomodate different target materials to study and evaluate nuclear effects; (d) particle identification for $e^\pm$, $\pi^\pm$, $K^\pm$, p, $\mu^\pm$; (e) sufficiently large fiducial target mass.

The STT technology offers a unique tool that can fulfill these requirements. It is designed to provide a control of the configuration, chemical composition and mass

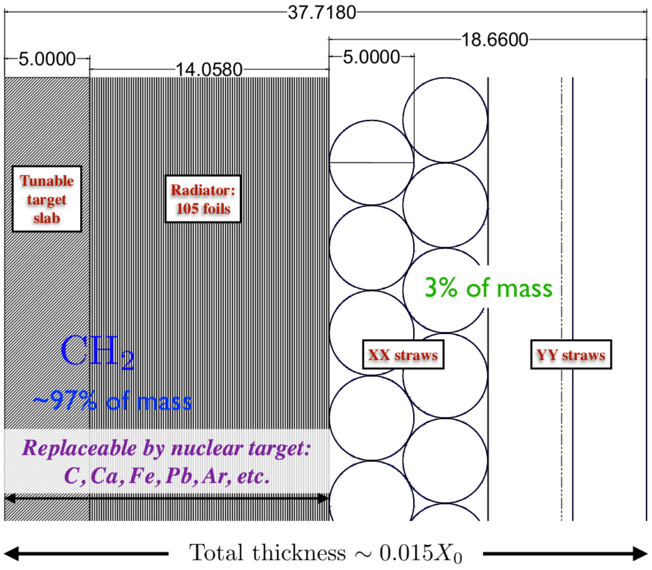

Figure 3.7: Schematic view of a STT module composed by three main elements (left to right): a tunable polypropylene CH_2 target slab, a radiator with 105 polypropylene foils, four straws layers XXYY. Lengths are in mm [27].

of the neutrino targets similar to what is achieved in electron scattering experiments. The neutrino targets are physically separated from the effective tracking system (the straws) which are of very low mass. Moreover, in order to achieve high resolution measurements, the target mass is spread out uniformly throughout the whole tracking volume and the average density is kept low enough to have a detector transparent to final state particles produced in neutrino interactions. Furthermore, the STT technology offers a general purpose facility that is fully tunable and its configuration can be varied and adapted during data taking.

The STT tracking system is designed to be a fully modular detector and each module can be operated and configured independently using different nuclear targets (e.g. C, Ca). The STT module technology is based on low-mass straws that consists of a tungsten wire, with a diameter of 20 μm and 20 nm gold coating, inside tubes with a diameter of 5 mm, mylar walls of 12 μm and Al coating of 70 nm. The tubes are filled with a gas mixture is Xe/CO_2 70/30 and operate with an internal pressure of about 1.9 atm.

The tracking system design considered in this thesis makes use of three types of STT modules. The first type have a polypropylene CH_2 target slab followed by a radiator and four straw layers XXYY, shown in figure 3.7. The slab is 5 mm thick and the radiator is composed of 105 polypropilene CH_2 foils 18 μm thick, separated from each other by 117 μm of air gaps. The radiator has a total thickness of 15.95 mm and its configuration is optimized to disentagle electrons from π using

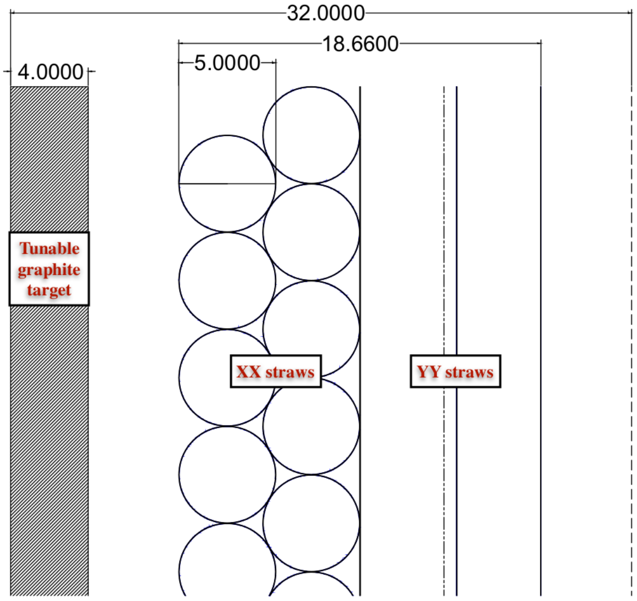

Figure 3.8: Schematic view of a STT module equipped with graphite target (left to right): a tunable graphite target, four straws layers XXYY. Lengths are in mm.

transition radiation. This type of STT module contains a total of 6.89 mm of CH_2 which corresponds to about 1.5% of the radiation length. Different module configurations can be obtained by removing the radiator and the slab, without affecting the functionality and mechanical stability, and integrating various nuclear targets, such as C, Ca, Fe, Pb, etc. In fact, the second module type is equipped with a graphite (pure C) target in front of four straw layers XXYY assembly, reported in figure 3.8. The thickness of the graphite target plate is equal to 4 mm: it has been chosen to match the same fraction of X_0 as the target of the first module type. Moreover, in order to ensure the same detector acceptance for CH_2 and C targets, these modules equipped with graphite are interleaved throughout the CH_2 modules. The third type, shown in figure 3.9, is the simplest one and it is composed by six straw layers XXYYXX glued together.

The complete STT assembly includes 78 STT modules with CH_2 slabs and radiators, 7 STT modules with graphite targets and 5 tracking modules with six layers of straws. Thus, the STT modules fill the magnetic volume, leaving the upstream region for the LAr target as shown in figure 3.10. The tracking modules with six straw layers are all placed in the downstream region of the inner volume except for one of them which is near to the LAr target. One module with graphite target is positioned in the volume center in order to have a symmetric configuration using the remaining modules. The remaining volume is filled with CH_2 modules

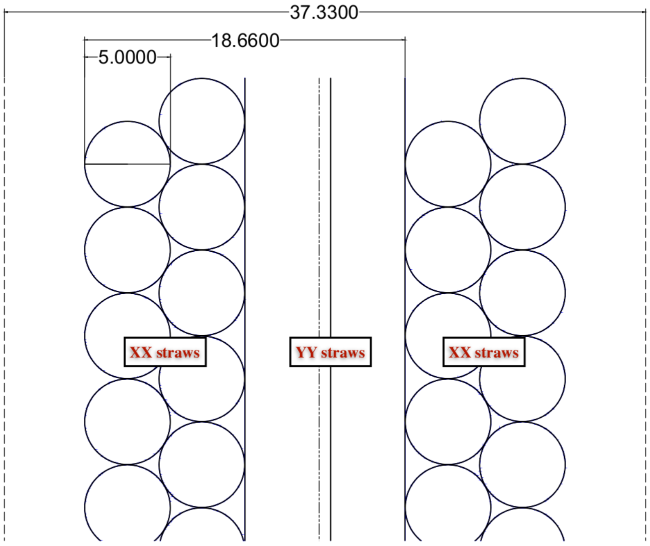

Figure 3.9: Schematic view of a STT module composed by six straws layers XXYYXX. Lengths are in mm.

with target slab and radiator interleaved with graphite target modules.

The total number of straws in the entire STT is 231834 and the straw layers represent less than 3% of the total detector mass, while, the passive targets account for up to 97%. The density depends on the module composition and for this STT design the average density is of 0.18 g/cm^3. The STT low-density and large volume allow the charged particles tracks to be relatively long. The radiation length is $X_0 \sim 2.6$ m and the total thickness of the STT is $\sim$1.34 X_0. Moreover, considering the z direction as the beam direction, the tracking sampling is of 0.15(0.36)% X_0 along the z direction (x, y directions).

The reference fiducial volume is defined as the inner region at a distance of 20 cm from the edges. The position resolution of a single hit is $\sim$0.2 mm in the x and y directions and the time resolution of a single hit is about 1 ns.

A complete detector simulation has been performed, based on GENIE and GEANT4, in order to study the influences of the target configurations in STT on the momentum resolution. The resulting momentum resolution is dominated by multiple scattering in the target materials and it is $\sim$3.1 % (5.9 % RMS) averaged over the momentum spectrum and the track lengths. Likewise the angular resolution is dominated by multiple scattering and it is $\sim$1.7 mrad (8.0 mrad RMS).

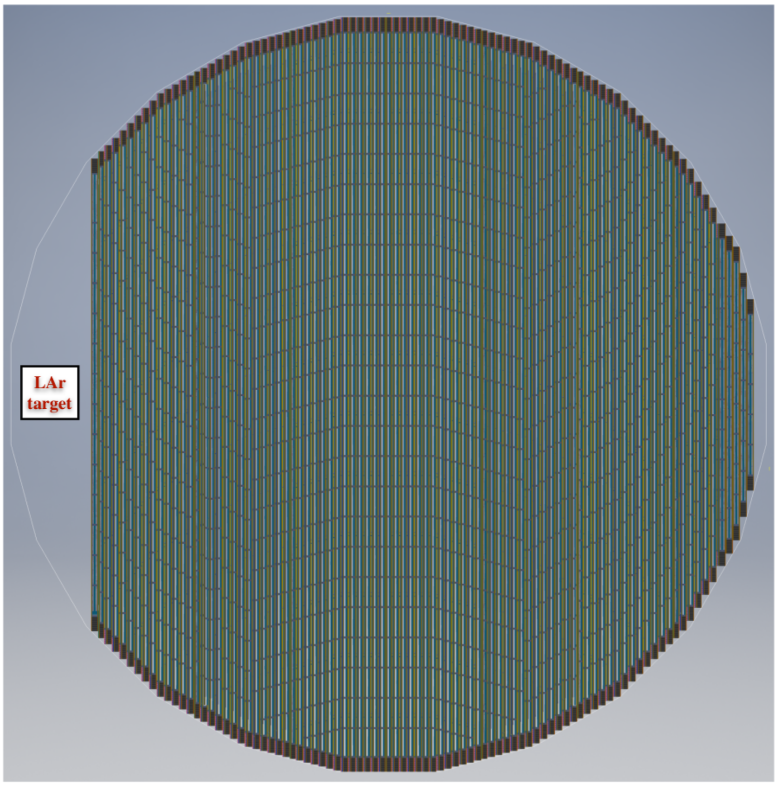

Figure 3.10: Engineering model of the STT assembly inside the inner magnetic volume within the electromagnetic calorimeter (not shown).

3.4 The active liquid argon target

An active liquid argon target is conceived in the upstream region of the inner magnetic volume, inside the ECAL. The LAr target will provide an Ar target permanently located on-axis and it will contribute for inter-calibration with the other ND detector components, while constraining the systematics in the oscillation data analysis. In particular, it will allow to evaluate nuclear effects by performing, together with the STT, measurements of neutrino interactions on argon, hydrogen and carbon within the same detector [3].

The LAr meniscus position, size and shape are still object of optimization and detailed studies are performed combined with the STT tracker to evaluate the reconstruction quality and the acceptance for different particles produced in the LAr target.

The cryostat walls, in which the LAr will be contained, are made of C-composite material and a thin aluminium foil is used to reinforce the internal surface. The thickness of the cryostat walls will be a small fraction of radiation length and the overall thickness of the LAr target ($\sim$1 X_0) is small enough to allow the outgoing particles to be analyzed by the downstream subdetectors, minimizing energy loss, shower production and multiple scattering [27, 3].

The reconstruction of charged particles passing through the LAr volume is based on an optical system that will collect scintillation light produced during particle propagation. The meniscus will be instrumented with arrays of SiPMs and covered by Hadamard masks optimized for event reconstruction in LAr [40].

3.5 Physics program

The SAND detector must be able to monitor the beam on-axis producing a statistically significant neutrino spectrum measurement over a relatively short time (one week) [3]. SAND measurements will be decisive to tune the beam model and control intended or unanticipated changes in the beam flux and spectra (e.g. target degradation). This information will be essential for the extraction of the FD expected spectra and also for the disentanglement of the causes that could have induced variations in the off-axis flux observed by ND-LAr and ND-GAr.

Dedicated analysis were performed to determine the sensitivity of SAND using combined data taken by the ECAL and STT and a significance of $\geq 3\sigma$ was obtained for the detection of most variations using a sample corresponding to one week of simulated data taking [27].

Flux measurements

The SAND detector will determine the absolute and relative fluxes of the different neutrino components of the beam studying the different interactions in the active volume. A precise measure of the fluxes $\Phi_{\nu(\overline{\nu})}$ is necessary to unfold the different terms that contribute to the event rate measurement at the ND, defined by eq.(2.3.2), and therefore for the FD oscillation analysis. The different interaction channels are the following: [27]

- elastic scattering $\nu e \rightarrow \nu e$ from which the absolute ν_μ flux is determined;
- $\nu p \rightarrow \mu^- p \pi^+$ on hydrogen with $E_\nu < 0.5$ GeV from which the relative ν_μ flux as function of neutrino energy is measured;
- quasi elastic scattering $\overline{\nu} p \rightarrow \mu^+ n$ on hydrogen with a Q-value $Q^2 \leq 0.05$ GeV^2, it allows to determine the absolute $\overline{\nu}_\mu$ flux;
- quasi elastic scattering $\overline{\nu} p \rightarrow \mu^+ n$ on hydrogen with $E_{\overline{\nu}} < 0.25$ GeV from which the relative $\overline{\nu}_\mu$ flux is determined;

- coherent interactions π^-/π^+ on C from which the ratio of $\overline{\nu}_\mu/\nu_\mu$ fluxes is found as function of neutrino energy within the same beam mode (FHC or RHC);
- $\nu(\overline{\nu})$ CC interactions on CH_2 targets, which provides the determination of ν_e/ν_μ and $\overline{\nu}_e/\overline{\nu}_\mu$ ratios as function of neutrino energy;
- $\nu(\overline{\nu})$ CC interactions on H from which are measured the ν_e/ν_μ and $\overline{\nu}_e/\overline{\nu}_\mu$ ratios;
- $\nu(\overline{\nu})$ CC interactions on H and CH_2 at low-ν, this allows the determination of parent $\mu/\pi/K$ distributions.

Constraints on the nuclear effects

As discussed in section 2.3.2, constraints on the nuclear effects in Ar can be obtained by a comparison between different neutrino-nucleus interaction topologies. $\nu(\overline{\nu})$-H interactions are of particular importance since (anti)neutrino scattering on hydrogen and ν-e elastic scattering are the only types of interactions free from nuclear effects. Thus, CC interactions on hydrogen provide insights on the structure of the free nucleon and useful information to constrain systematic uncertainties related to the nuclear smearing.

The SAND STT provides different nuclear targets including CH_2 plastic and graphite targets. Modules equipped with graphite (pure C) plates are relevant to achieve a model independent subtraction of the C background from interactions measurements on the CH_2 targets, identifying the $\nu(\overline{\nu})$-H interactions. In order to obtain an effective selection of the $\nu(\overline{\nu})$-H interactions the kinematics of the event can be exploited. Since the hydrogen target is at rest, the neutrino CC events are predicted to be perfectly balanced in a plane transverse to the direction of the beam, hence, the muon and the hadron vectors are expected to be found in the same plane. On the contrary, neutrino interactions with other heavier nuclear targets are largely affected by initial and final nuclear smearing and they are expected to be characterized by a significant missing transverse momentum. A detailed study on the kinematic selection performances show that purities of 80-95% of the selected H samples can be achieved and, depending on the interaction process, the efficiencies of the kinematic selection would be in the 75-95 % range [27].

Therefore, taking advantage of the unique set of features provided by STT and LAr meniscus, SAND will be able to constrain the nuclear smearing for the ND beam spectrum. Considering the eq.(2.3.2) for the interaction rate at the ND, SAND will directly constrain the product of the cross section and the physics response on argon ($\sigma_{\nu(\overline{\nu})}\ R_{phys}$). Indeed, once the fluxes are precisely measured, the convolution of three terms $\sigma_\nu\ R_{phys}\ R_{det}$ is left to be unfolded. To constrain the product $\sigma_{\nu(\overline{\nu})}\ R_{phys}$, a comparison between (anti)neutrino interactions on Ar and H is necessary. For the hydrogen target $R_{phys} \equiv 1$ and the cross section can be accurately measured thanks to the large expected statistics. The unfolding of neutrino energy for events on H target depends only on the detector response R_{det} that is defined by the $\delta p/p$ calibrated to 0.2% from the K_0 mass peak. The similar geometries of the Ar target and the straw modules guarantee a similar detector response (acceptance) R_{det}. Hence, from the comparison between the CC samples in Ar and H, the product $\sigma_{\nu(\overline{\nu})}\ R_{phys}$ on argon can be constrained [27].

Precision measurements and nucleon structure investigation

SAND will be able to perform a precise measurement of the weak mixing angle ($\sin^2\theta_W$) in (anti)neutrino scattering at the DUNE energies. A measurement of $\sin^2\theta_W$ can be obtained by the ratio of NC and CC deep inelastic scattering (DIS) neutrino interactions $\mathcal{R}_\nu \equiv \sigma_{NC}/\sigma_{CC}$. Another independent measurement can be provided studying NC $\nu_\mu e$ elastic scattering and the value of $\sin^2\theta_W$ can be extracted from the ratio $\mathcal{R}_{\nu e} \equiv \sigma(\overline{\nu}_\mu e \to \overline{\nu}_\mu e)/\sigma(\nu_\mu e \to \nu_\mu e)$. These two channels will also provide the opportunity to test the running of $\sin^2\theta_W$ since they are characterized by substantially different momentum transfer scales. Other interesting channels to be analyzed are the coherent ρ production through the ratio $\mathcal{R}_\rho \equiv (\nu_\mu\mathcal{A} \to \nu_\mu\rho^0\mathcal{A})/(\nu_\mu\mathcal{A} \to \mu^-\rho^+\mathcal{A})$ and the NC elastic scattering off protons.

Due to the possibility to integrate various thin nuclear targets within the STT, SAND will also allow to inspect the nucleon structure disentangling nuclear effects. Using neutrino and antineutrino DIS, the parton distribution functions, cross sections, perturbative and non-perturbative corrections can be studied in a wide range of transverse momentum Q^2 and Bjorken x. SAND data will provide unique information of the nucleon structure, complementary to the current programs at colliders and fixed-target electron DIS experiments.

The SAND detector will investigate the isospin and the number of valence quarks of the target taking advantage of the presence of H and other nuclei (Ar, C) in STT. Using the large samples expected of $\nu(\overline{\nu})$-H interactions a precision test of the Adler sum rule, $S_A = 0.5\int_0^1 dx/x(F_2^{\overline{\nu}p} - F_2^{\nu p}) = I_p$, and the Groo-Llewellyn-Smith (GLS) sum rule, $S_{GLS} = 0.5\int_1^0 dx/x(xF_3^{\overline{\nu}p} + xF_3^{\nu p})$, can be performed. The Adler sum, in the quark-parton model, corresponds to the difference between the number of valence u and d quarks of the target. From the differential cross section on hydrogen can be determined the structure functions $F_2^{\overline{\nu}p}$ and $F_2^{\nu p}$ and the measure of the Adler sum as function of the momentum transfer Q^2 is obtained. The GLS sum, in the quark-parton model, gives the number of valence quarks in the nucleon. This sum rule can be used to obtain the strong coupling constant $\alpha_s(Q^2)$ since it receives perturbative and non perturbative QCD corrections. Moreover, SAND will allow to accurately determine the strange vector and axial-vector form factors which are important elements to improve the knowledge about the nucleon structure. In particular the measurement of the NC elastic scattering off protons, with hydrogen and other nuclear targets, can be used to accurately determine the strange axial-vector current [27].

Searches for new physics

In general, unexpected deviations from the SM predictions in the measurements performed by SAND will be the manifestation of new physics BSM. Furthermore, SAND will also allow to study possible BSM physics effects, for example the detector will offer the opportunity to test the low-energy anomaly of MiniBooNE experiment [41].

Possible oscillations into sterile neutrinos can be identified studying CC ratios $\mathcal{R}_{e\mu}(L/E) \equiv (\nu_e N \to e^- X)/(\nu_\mu N \to \mu^- X)$ and $\bar{\mathcal{R}}_{e\mu}(L/E) \equiv (\overline{\nu}_e N \to e^+ X)/(\overline{\nu}_\mu N \to \mu^+ X)$ and NC/CC ratios $\mathcal{R}_{\nu p}$ and $\mathcal{R}_{\overline{\nu} p}$ as function of the source-detector distance and neutrino energy ratio (L/E). Moreover, the excellent sensitivity to ν_τ appearance would allow to investigate the possibility of either oscillations with sterile neutrinos or NSI.

In addition, the unique set of features provided by SAND can significantly enhance the physics sensitivity of the ND complex in the search for heavy sterile neutrinos, light DM, dark photons, etc. [27].

Chapter 4

Event Reconstruction in the calorimeter and e.m. shower identification

The results presented in this chapter are based on a full simulation of the SAND detector performed using several software tools. The geometry of the detector is implemented using the *dunendggd* package [5]. The neutrino interactions are generated with GENIE [4] while the particle propagation and the related detector response are simulated using the *edep-sim* package [6]. In addition, the signal digitization and the event reconstruction are performed through C++ based algorithms.

4.1 Event simulation chain

In this section the software simulation components are described in detail.

The SAND geometry

The *dunendggd* package is a tool developed in order to build proposal geometries for the DUNE ND. It is based on the General Geometry Description (*gegede*) which is a module that allows to generate the description of constructive geometries in *gdml* files, with applications in GEANT4 and ROOT.

The geometry used in this work of thesis is modeled to reproduce the KLOE yoke, magnet, its electromagnetic calorimeter and an inner tracking system based on the STT technology and an active LAr target, as already described in section 3.4. In figure 4.1 the SAND detector geometry is shown.

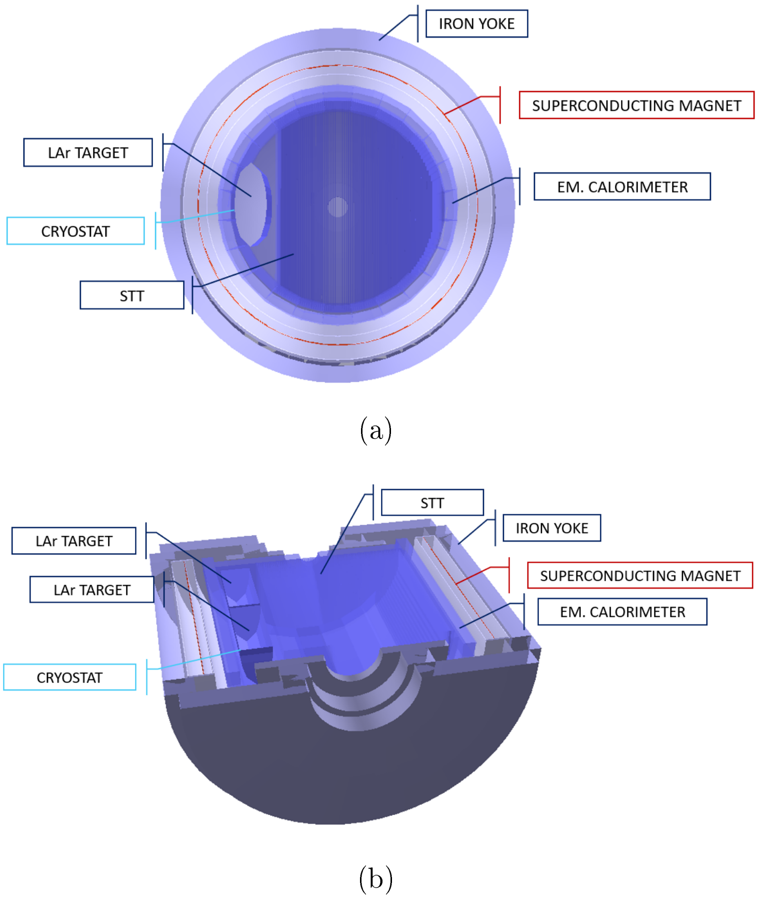

(a)

(b)

Figure 4.1: Vertical (a) and horizontal (b) cross section views of the SAND geometry implemented in the simulations. The neutrino beam enters the SAND detector from left.

The coordinates system is chosen such that the center position of SAND is (0.00, -2384.73, 23910.00) in mm, the x axis pointing along the cylindrical volume axis, the y axis vertically towards the top of the detector, while the z axis is the horizontal projection of the beam direction.

The magnet geometry is represented by an external iron yoke and a copper coil is inserted between the inner and outer aluminium walls of the cryostat. The internal volume of the magnet is a cylinder 3.38 m height with a radius of 2.0 m.

The simulated ECAL is approximated by 209 polystyrene scintillator slabs (0.07 cm thick) interleaved with 209 lead slabs (0.04 cm thick). The ECAL barrel consists of 24 trapezoidal modules (4.3 m long, 23 cm thick, with the major base of 59 cm and the minor one of 52 cm). The ECAL endcaps are approximated as cylindrical modules of 2 m radius and 23 cm thickness.

The tracking system is composed by STT modules of different configurations: tracking modules with no target, C target modules and C_6H_6 target modules. As described in section 3.3, they are arranged in the inner volume considering that a certain distance from the LAr cryostats must be left for the instrumentation, the closest module close to the cryostat is a tracking module with six straw layers and a C target module is placed at the center of the volume.

The LAr active target is configured to be contained in two cryostats, 6 cm apart from each other, located in the upstream part of the inner volume.

Neutrino events generation

The GENIE software is a neutrino interaction event generator, developed in C++ by a collaboration of physicists from several neutrino experiments. It represents a tool for the experimental physics community that is currently used by a large number of experiments in the neutrino field [4].

The neutrino event generation in SAND is performed via a GENIE-based tool. To generate the events, the program integrates various information necessary for the input of GENIE: (a) the detector geometry, described before, defined in a *gdml* file; (b) the neutrino cross sections with different target nuclei pre-calculated and saved in a *xml* file; (c) details about the beam, as the neutrino beam inclination, spectra and fluxes (the latter are delivered as 1-dimensional ROOT histograms).

The GENIE output file provides the event details regarding the simulated processes.

Particles propagation and detector response

Edep-sim is a wrapper of the Geant4 toolkit [42]. It provides a detailed model of the energy deposits due to ionization and scintillation. *Edep-sim* uses the output retrived from GENIE to simulate the particle transportation. The output of simulations is stored in ROOT file format containing a TGeoManager object, named *EDepSimGeometry*, and a ROOT tree, called *EDepSimEvents*, in which the event data is saved. The tree contains a *TG4Event* object, corresponding to a simulated neutrino event and including all the information of the primary particles. The *TG4Event* class is characterized by the following fields [43]:

- *EventId*, the number of the event;
- *RunId*, the number of the run;
- *Primaries*, a branch containing the information about the primary particles produced in the neutrino interaction;

- *Trajectories*, a branch holding the trajectories of all particles simulated in the event. Several details are specified for a Trajectory object: the identifiers of the track and its parent, the pdg code of the particle producing the trajectory, the initial momentum and the set of the points produced along the track. To each point the particle momentum and position 4-vectors are associated;
- *SegmentDetectors*, a branch containing a map between the hits occurred in the event and the sensitive detector sections in which they are recorded.

4.1.1 Digitization

The digitization simulates the digital signal that would be obtained by the DAQ system. In this thesis, the *edep-sim* output is converted into detector digits in order to be used for the subsequent event reconstruction. The signal digitization is realized for both the ECAL and the STT and the output of the digitization is stored in a ROOT tree with two branches containing the calorimeter and STT digits.

ECAL digitization

The ECAL digitization involves the reproduction of the calorimeter segmentation and the signal formation on the photo sensors.

To reproduce the ECAL readout, the digitization is implemented by segmenting in depth each barrel module in 5 layers, each divided in 12 cells; while, the endcaps modules are segmented in 5 layers and each is then partitioned into 90 cells. Each cell is uniquely distinguished by an identifier characterized by five numbers. The first two from left indicate to which module the cell belongs: the two endcap modules are labelled with 30 and 40, the barrel modules are numerated from 00 to 23 starting from the top and proceeding clockwise. The central number of the identifier corresponds to the number of the layer in which the cell lays down and these are numerated from 0 to 4 starting from the inner layer out. The last two numbers of the identifier define the number of the cell in the layer: for a barrel module, they range from 00 to 11 beginning from left, while, for the endcaps they range from 00 to 89. In figure 4.2 is reported a schematic representation of one barrel module segmentation.

For each cell, the light produced in the fibers is read out on both sides by two PMTs. The PMT response, i.e. the number of photo-electrons produced by a hit, is simulated taking into account the light attenuation due to the fiber and the energy deposit conversion into photo-electrons. Thus, the digitization proceedes by analyzing the information about the hits produced in the ECAL active layers (scintillator slabs), acquired from the output of *edep-sim*. Each hit is associated

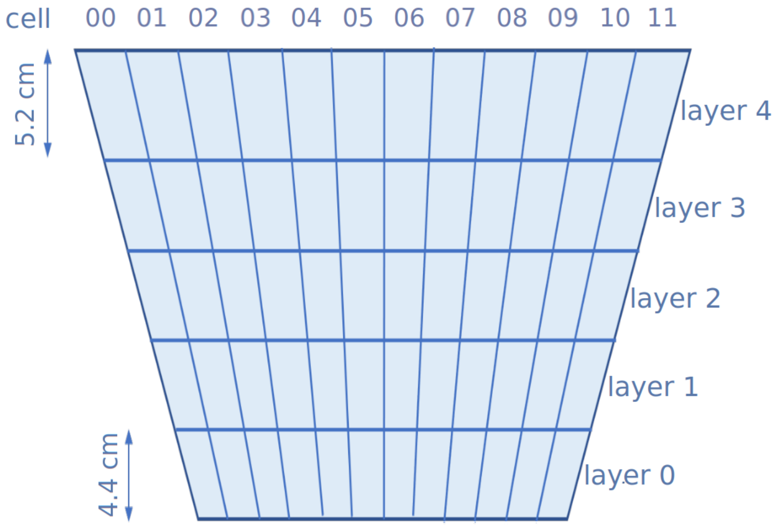

Figure 4.2: Schematic representation of one barrel module segmentation. The module is divided in 5 layers, each 4.4 cm deep, except for the outermost, which is 5.2 cm deep. Each plane is subdivided in the transverse direction to the fibers into 12 cells.

with the corresponding cell position and the deposited energy dE of the crossing particle, these are used to determine the number of photo-electrons produced on a photo sensor. Considering the photo sensor on side B, the number of photo-electrons N_{pe} is obtained from a Poisson distribution having a mean value μ_{pe} given by

$$\mu_{pe} = dE \cdot A_l \cdot Epe \tag{4.1.1}$$

where A_l is the attenuation factor in the fiber and Epe is the conversion factor of energy into the number of photo-electrons. The attenuation factor is defined as

$$A_l = p_1 \cdot \exp\Big(- \frac{d_B}{alt_1} \Big) + (1 - p_1) \cdot \Big(- \frac{d_B}{alt_2} \Big), \tag{4.1.2}$$

where d_B is the distance between the hit position and the photocatode on side B, p_1 is equal to 0.35, alt_1 is 50 cm and alt_2 assumes different values depending on the layer number l: for $l = 0$, 1 it is equal to 430 cm, 380 cm for $l = 2$ and 330 cm for $l = 3$, 4. The conversion factor is set to $Epe = 18.5$ so that the simulations reproduce the value obtained by the KLOE collaboration of a light yield of about 1 photo-electron per MeV deposit for a MIP crossing the barrel module at the centre [2].

Once the number of photo-electrons is found, the ADC signal S^B on side B of the cell is given by

$$S^B = N_{pe} \cdot peADC, \tag{4.1.3}$$

where the factor $peADC = 4$ converts the number of photo-electrons into ADC counts.

The arrival time of the photon at the photo sensor is given by

$$t_{pe} = t_{cross} + t_{decay} + d_B \cdot u_{ph} + \text{Gauss}(1\text{ ns}), \tag{4.1.4}$$

where t_{cross} is the time associated to the particle crossing the cell, t_{decay} is the scintillation decay time, $d_B \cdot u_{ph}$ is the time of the signal propagation through the cell given by the product of the distance d_B between the hit and the photo sensor and the inverse of the velocity of the photons in the scintillating fibers u_{ph} and Gauss(1 ns) is a gaussian smearing corresponding to the photo sensor time uncertainty. The value of t_{decay} is obtained applying the same formula used by the KLOE collaboration:

$$t_{decay} = t_{scint}\Big(\frac{1}{r_{ph}(1)} - 1\Big)^{t_{scex}}; \tag{4.1.5}$$

where $r_{ph}(1)$ corresponds to a random number generated between 0 and 1, $t_{scint} = 3.08$ ns and $t_{scex} = 0.588$. These values were tuned by the KLOE collaboration to reproduce the measured preformances of the ECAL.

The TDC value is then computed as the 15% of constant fraction.

In the output file of the digitization, the calorimeter digits are defined by the following fields:

- the cell identifier;
- the position coordinates of the cell center;
- the length of the cell (distance from one side to the other);
- the distinct labels of the module, layer and cell;
- the two sets of photo-signals recorded by the photo sensors.

Moreover, the fields that characterize each photo-signal are

- the side in which the photo-signal is produced;
- the ADC value;
- the TDC value;
- the collection of photo-electrons (each defined by their arrival time and the index of the hit that produced them).

STT digitization

The STT modules are distinguished from each other using an identifier that increases from the upstream to the downstream side. The active elements of each STT module correspond to the straw tubes layers. These layers are configured with horizontal (XX) or vertical (YY) straw tubes.

In this context, the digitization consists in forming groups of hits produced in the same straw tube due to the crossing of a particle and associating to each group a position, a time and an energy deposit. Depending on whether the tube is horizontal or vertical the y and z or x and z position coordinates are associated to the digit. The time is calculated as the average between the first hit starting time and the last hit end time. The energy is given by the sum of the energy deposits by each individual hit in the same tube.

In the output file of the digitization, the STT digits are defined by the following fields:

- the name of the volume where the energy deposit occurs;
- the identifier of the straw tube;
- the position coordinates of the digit;
- the time coordinate of the digit;
- the energy deposit;
- a flag indicating if the straw tube is horizontal or vertical;
- the indices set of the hits that contributed to the digit.

4.1.2 Event reconstruction using Monte Carlo truth information

At the time of this work of thesis, the event reconstruction implemented in a C++ code exploits both digitization and MC truth information and it cannot be applied to real data. Reconstruction on STT and ECAL is performed separately by two algorithms, the first one for track searches in the STT and the second one for cluster searches in the ECAL.

This section briefly describes these MC truth-based reconstruction algorithms.

STT reconstruction

The track reconstruction performs pattern recognition exploiting MC truth, assembling the digits produced by the same particle into a track. Once the track finding is completed, a fit is performed and parameters are inferred. The track fitting is based on the assumption that the magnetic field along the x axis is uniform, while energy loss are not taken into account; therefore, a particle trajectory can be described by a cylindrical helix given by a linear motion along the x direction and a rotation in the z-y plane. The parametric equation of the helix, expressed as function of the path length along the helix s, is used to fit the tracks of charged particles. The parametric equation is defined as

$$\begin{cases} z(s) = z_0 + R\big[\cos\big(\Phi_0 + \frac{hs\cos\lambda}{R}\big) - \cos\Phi_0\big] \\ y(s) = y_0 + R\big[\sin\big(\Phi_0 + \frac{hs\cos\lambda}{R}\big) - \sin\Phi_0\big] \\ x(s) = x_0 + s\sin\lambda \end{cases} , \tag{4.1.6}$$

where x_0, y_0 and z_0 are the starting point coordinates at $s = 0$, R is the radius of the helix, Φ_0 is the azimuth angle of the starting point with respect to the helix axis, $h = \pm$ defines the sense of rotation in the z-y plane and λ is the *dip angle* defined as the angle between the directions of the total momentum and transverse momentum P_T of the particle, $\tan\lambda = P_L/P_T$ (P_L is the longitudinal momentum).

The helix projected to the z-y plane (see figure 4.3) can described by a circle defined as

$$(z - z_0 + R\cos\Phi_0)^2 + (y - y_0 R\sin\Phi_0)^2 = (z - z_c)^2 + (y - y_c)^2 = R^2, \tag{4.1.7}$$

where y_c and z_c are the coordinates of the circumference center. The horizontal straws deliver the true z and y coordinates that can be used to derive, from the circular fit, the values of the radius R and the circle center coordinates y_c and z_c. Then, to compute the value of the *dip angle* the curved track is approximated to a parabola. This is a simple and fast approximation valid if $s/R \lessapprox 1$ (i.e. when the track is reconstructed in a region of small size compared to the radius R). Applying a first order Taylor expansion in s/R, the parametric equation in the parabolic approximation becomes

$$\begin{cases} z(s) = z_0 - hs\cos\lambda\sin\Phi_0 - \frac{1}{2}\frac{s^2\cos^2\lambda}{R}\cos\Phi_0 \\ y(s) = y_0 - hs\cos\lambda\cos\Phi_0 - \frac{1}{2}\frac{s^2\cos^2\lambda}{R}\sin\Phi_0 \\ x(s) = x_0 + s\sin\lambda \end{cases} . \tag{4.1.8}$$

Then, performing a coordinate transformation from the z-y plane to ρ-y'

$$\begin{cases} \rho = z\cos\big(\frac{\pi}{2} - \Phi_0\big) + y\sin\big(\frac{\pi}{2} - \Phi_0\big) \\ y' = -z\sin\big(\frac{\pi}{2} - \Phi_0\big) + y\cos\big(\frac{\pi}{2} - \Phi_0\big) \end{cases} \tag{4.1.9}$$

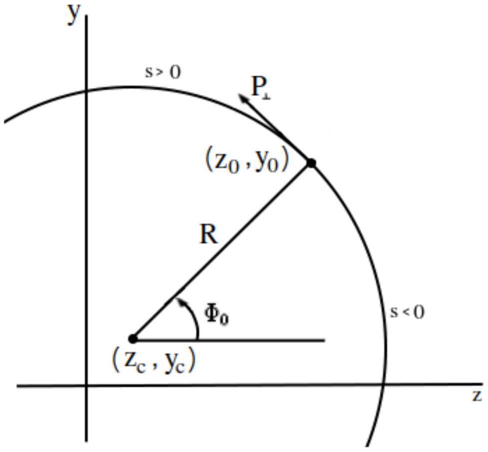

Figure 4.3: Projection on the z-y plane of the helix that describes the trajectory of a charged particle in uniform magnetic field parallel to the x axis. The projection is a circle shown assuming a positive sense of rotation (h=+1).

the equation of motion in the x-y' plane becomes

$$\begin{cases} x = x_0 + \rho\,\tan\lambda \\ y' = d_0 - \frac{h}{2R}\rho^2 \end{cases} , \tag{4.1.10}$$

where d_0 is the impact parameter defined as the distance in the x-y plane between the starting point and the reference frame origin. Then, using the x and z coordinates delivered by the vertical straws and the values of R, y_c and z_c inferred from the circular fit, the coordinate y is derived as

$$y = y_c + h\sqrt{R^2 - (z - z_c)}. \tag{4.1.11}$$

ρ and y' are computed from eq.(4.1.9), knowing that

$$\begin{cases} \cos(\frac{\pi}{2} - \Phi_0) = \frac{h(y_0 - y_c)}{R} \\ \sin(\frac{\pi}{2} - \Phi_0) = -\frac{h(z_0 - z_c)}{R} \end{cases} . \tag{4.1.12}$$

Thus, the *dip angle* can be extrapolated from a linear fit using eq.(4.1.10).

In the output of the reconstruction based on MC, the STT tracks are characterized by the following fields:

- the index of the track;
- the position and time coordinates of the track starting point (x_0, y_0, z_0, t_0);

- the parameters provided by the circular fit (the circumference center z_c and y_c, the circle radius R, the direction of the trajectory h);
- the parameters provided by the linear fit (the intercept a and the slope b);
- two flags indicating if the linear and the circular fits have been well performed (ret_ln and ret_cr respectively) and two variables indicating a rough quality measurement of the linear and circular fits ($chi2\_ln$ and $chi2\_cr$ respectively);
- the two sets of the horizontal and vertical digits belonging to the track.

ECAL reconstruction

The reconstruction algorithm analyzes the hits produced on each fired cell of the calorimeter and to each one it associates the trajectory ID of the particle that have produced more photo-electrons on the cell photo sensors. This step is performed exploiting the MC truth. Then, these particles are identified as the parent particles of the clusters produced in the ECAL. Therefore, taking advantage of the association done between the fired cells and the trajectory IDs, the cells are grouped into clusters. Only those cells that have photosignals produced on both sides are added to a cluster. Then, for each cluster, position and time coordinates are evaluated as the energy-weighted averages over the contributing cells. Also position variances are calculated. Moreover, the energy associated to each cluster correspond to the sum of the energy collected by the cells. For each ECAL layer over which a cluster spans, an energy-weighted position is found and then a linear track model is performed on the position points to obtain the cluster direction vector.

4.2 A new ECAL cluster reconstruction

In this work of thesis a new clustering algorithm based only on digitized data and not exploiting at all Monte Carlo truth has been developed and studied for the first time. The algorithm is developed in C++ and integrated in the SAND simulation framework. It is inspired by the reconstruction procedure already developed in the KLOE experiment, but it is adapted and tuned for the SAND detector in the DUNE experiment. The dedicated algorithm has been developed in order to group together neighboring hit cells and reconstruct clusters in the ECAL that will be associated to a particular physical object, a track or a shower.

The input of the clustering algorithm is retrieved from the output of the digitization. Thus, a hit in the calorimeter is associated to a cell and may produce signals on one or both the photo sensors placed at the ends of the given cell, depending on the energy deposit and the hit position inside the fiber.

The procedure selects the fired cells of the calorimeter in the event, i.e. those cells with at least one photon detected by one of the two readout channels. Then, the algorithm divides the fired cells into two different sets: the *complete* cells, which have photons produced at both sides; the *incomplete* cells, which have a side without any photo-signal. Next, the algorithm groups neighboring fired cells into pre-clusters. Only *complete* cells are included in the pre-clusters search and the subsequent steps, while the *incomplete* ones will be considered only at a later stage.

Pre-cluster search

A recursive procedure starts from one hit cell, that represents the seed of the pre-cluster, and checks for other fired cells among the adjacent ones that surround it (even diagonally). If neighboring hit cells are found, they are added to the pre-cluster and the procedure is reiterated over them. The routine continues until no adjacent fired cells can be grouped anymore. Once a pre-cluster is complete, this routine is then reiterated starting from another complete cell up to completion of all the active cells associated to the event.

Pre-clusters are defined by the following quantities:

- the energy, given by the sum of the cell pulse heights weighted by the respective cell calibration factor;
- the time and the position coordinates of the centroid; calculated as energy-weighted averages over the contributing cells;
- the position variances.

After preclustering, several additional operations such as clusters splitting and merging are applied to improve the performances of the algorithm.

Pre-clusters splitting

A splitting procedure is implemented in order to separate pre-clusters that might be produced by the overlap of particles trajectories and result as a single group of cells. The splitting procedure compute the time variance of each cells group and in case of a large discrepancy (> 5 ns) the pre-cluster is divided into quadrants forming new pre-clusters and for each the parameters are computed again.

Pre-clusters merging

The merging procedure is implemented to merge groups of cells that might be originated from the same shower or track. This routine compares two close pre-clusters and if their spatial distance is smaller than 40 cm and their time difference is smaller than 2.5 ns, the two groups of cells are merged together and the parameters associated to the whole group are updated.

Cluster direction

The formed clusters are analyzed and fit to a direction with an apex origin. For each ECAL layer on which the cluster broadens, a weighted average cluster position is calculated. Then, the direction vector is computed by performing a linear regression over the points found for each layer.

Recovering of *incomplete* cells

The recovery of the *incomplete* cells is performed in order to improve and update the cluster energy. The *incomplete* cells can be recovered and assigned to a cluster by a comparison between the cell position and the closest cluster centroid.

Consider the reference frame in which the origin is in the center of the SAND volume, the x axis points along the solenoid axis and the orthogonal z-y plane have the y axis vertical, see figure 4.4. In the barrel, the recovering is based on the angular distance $|\Delta\Phi|$ between the two angular positions computed in the z-y plane and *incomplete* cells are added to the cluster if $|\Delta\Phi| < 3°$. Similarly, in the endcaps, the recovering is performed if the angular distance is $|\Delta\theta| < 3°$, where the angular positions are calculated in the x-y plane.

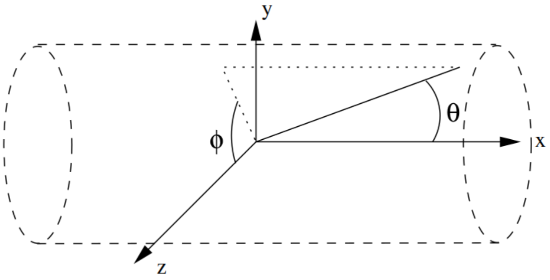

Figure 4.4: SAND reference frame with origin at the center of the detector.

Output of the clustering algorithm

The clustering algorithm produces a new output file and the corresponding output data model, recorded in a ROOT tree, is defined as a list of clusters reconstructed for each event. The fields assigned to each cluster are

- the cluster energy;
- the position coordinates of the centroid
- the position variances;
- the average time of the cluster;
- the direction versor (described by the three Cartesian coordinates);
- the set of cells belonging to the cluster.

4.3 Track/shower discrimination

This section concerns the evaluation of the performance of the clustering algorithm for the discrimination between electromagnetic (e.m.) showers and muon tracks in the ECAL, obtained by means of a multivariate analysis. In particular, a multivariate analysis is realized to perform a classification of the clusters reconstructed by the clustering algorithm and study the capabilities in e.m. showers and muon tracks discrimination. The multivariate analysis is implemented using the Toolkit for Multivariate Analysis (TMVA) software package [44].

The following classification analysis consists of two separated phases: the training phase, where the multivariate methods are trained and validated, and the application phase, where the selected optimal methods are applied to the classification problem in neutrino interactions simulated in the whole SAND detector.

4.3.1 Training with dedicated particle beams

A specific dataset is used to train and validate the classification models implemented in the multivariate analysis. This dataset is obtained by a simulation based on GEANT4 and *edep-sim* developed in order to have clear events without particle overlapping in the ECAL. Particle guns of electrons and muons with a fixed source position and direction are settled in order to analyze events of particles that enter the calorimeter having a negligible energy loss in the STT. They are originated within the SAND detector, near the top of the tracking system, 1 cm from the calorimeter, as it is shown in figure 4.5. The particle gun is directed upwards, towards the ECAL. The whole dataset is formed by $4.1 \cdot 10^5$ events of electrons and $4.1 \cdot 10^5$ events of muons. Moreover, the energies of these particles follow the energy spectra of electrons and muons that enter the SAND calorimeter from ν_μ events for a neutrino beam produced in FHC mode. The expected energy distributions are reported in figure 4.6.

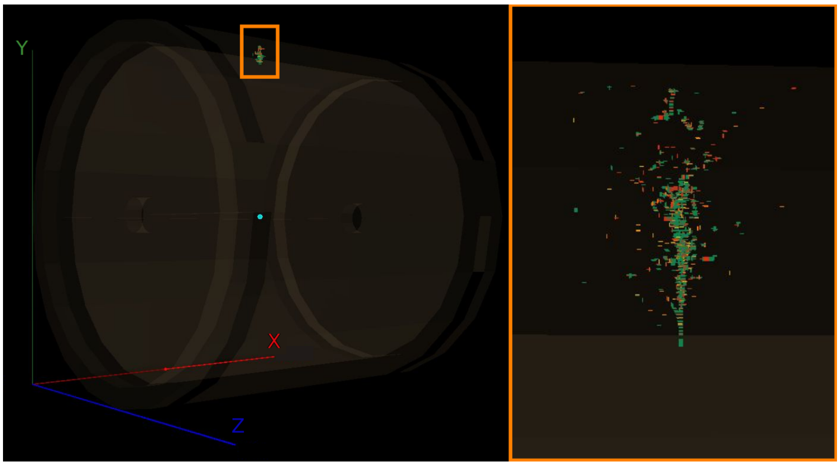

Figure 4.5: Event display of an electron of 1 GeV simulated with GEANT4 and *edep-sim*. The electron is originated 1 cm from the ECAL and it is directed upwards. In the display only the calorimeter volume is shown (shaded).

Multivariate analysis implementation

The training dataset is processed by the clustering algorithm to reconstruct clusters (see section 4.2) produced by a muon or an electron propagating in the ECAL. Then, a multivariate analysis is implemented in order to perform a classification of the clusters dataset.

The TMVA toolkit provides a machine learning environment, integrated using ROOT, for the processing, evaluation and application of multivariate classification and regression techniques [45].

The classification problem concerns the discrimination of e.m. showers from muon tracks. Electron clusters are defined as signal and muon ones as background. The training and validation datasets are obtained by randomly splitting the total preliminary sample, a 50% is used for the training and a 50% for the validation. The event weights are set to 1.0 for both signal and background. Three classification methods have been processed: a Fisher (linear) classifier, an artificial Neural Network (NN) and a Boosted Decision Tree (BDT).

The Fisher method performs a linear discriminant analysis. It finds the linear combination of the input variables, with zero linear correlations, which maximises the separation between the mean values of the signal and the background distributions. The classification decision is based on the value of the linear combination of the input variables. In other words, the Fisher discriminant method performs the event selection in a transformed variable hyperspace by determining an axis for which the signal and background data are most separated when projected upon this axis.

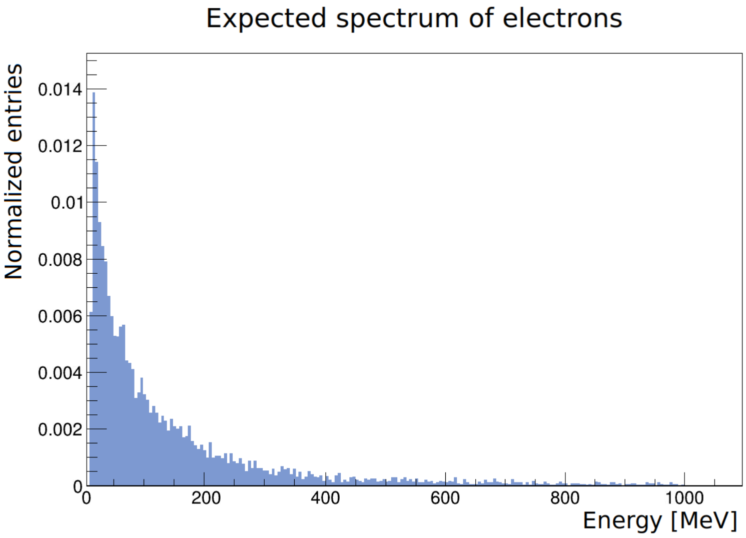

(a)

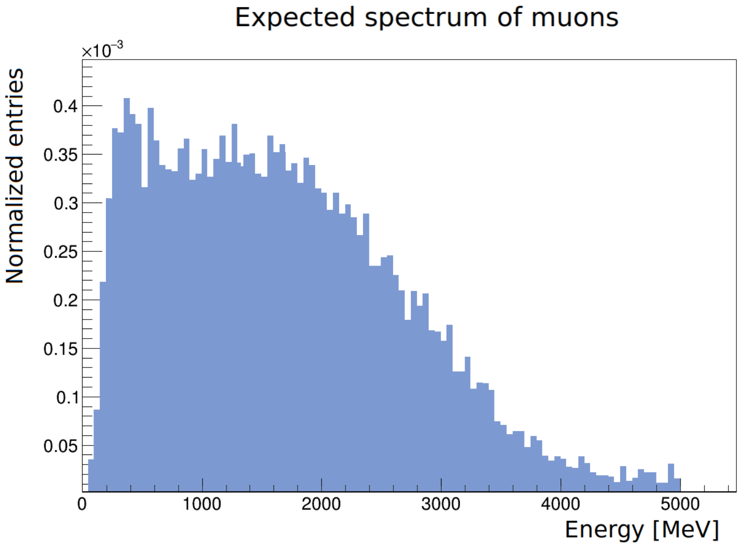

(b)

Figure 4.6: Spectra of electrons (a) and muons (b) originated by neutrino interaction or by secondary interactions that enter the SAND electromagnetic calorimeter. The energy spectra are obtained from an analysis performed on a ν_μ beam in FHC mode simulation.

The NN is implemented as a feedforward multi-layer perceptron (MLP): the neurons are organized in layers and only direct connections from a given layer to the following one are allowed, see figure 4.7. The input variables are scaled in order to have similar ranges. This helps the training process to converge more quickly

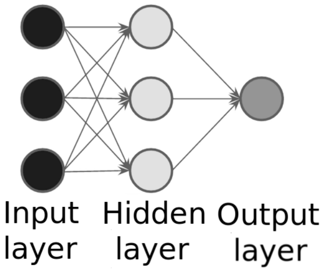

Figure 4.7: Example of a multi-layer perceptron with one hidden layer. The NN trained in this analysis has an input layer with ten neurons, one hidden layer with fourteen neurons and one output layer.

and the model to learn appropriate weights for each feature, avoiding to pay too much attention to the features having wider ranges. Thus, the input variables are normalized to the interval [-1, 1]. The NN architecture is characterized by one hidden layer with fourteen units. For each neuron of the NN the output is calculated using the hyperbolic tangent (*tanh*) activation function, which takes input values and produces output values in the range between -1 and 1. To update the weights and optimise the classification performace the back propagation algorithm is used. The model is trained on 500 epochs, during which overtraining tests are performed. The overtraining validation is provided by a comparison between the results obtained on the training and the independent validation samples. The test frequency is set to five tests at each epoch.

The BDT consists in an ensemble of decision trees and it performs the event classification relying on the majority vote of the individual trees. An individual decision tree takes decisions at each node using one discriminant variable at a time performing a binary splitting of the data. A sequence of decisions are taken ending up into a final node in which the classification into signal or background is performed. The decision rules and data classification are inferred from the data features of the training sample. The AdaBoost method is employed to train the trees: in succession the decision trees are trained on the same original training dataset but weights of misclassified events in the previous tree are updated and increased for the training of the following tree. The BDT is characterized by a collection of 850 trees with a maximum depth allowed equal to 4. A grid of 20 points in the variables ranges is used to find the optimal value in node splitting and the Gini index is used as criterion to measure the quality of the split.

The classification of electron-like clusters or muon-like clusters is based on cluster-shape features passed as input variables. These variables have been chosen in order to take advantage of the differences in the characteristic energy deposit profiles and other aspects of the cluster development. Muons travelling through

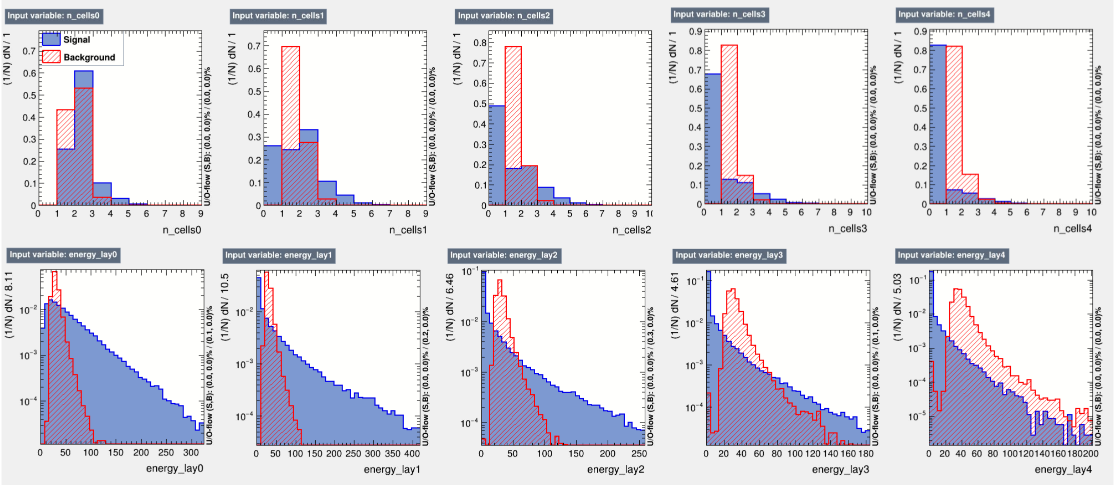

Figure 4.8: Distributions of the cells number per layer and the visible energy deposited per layer (in logaritmic scale). The signal distributions are in blue, the background ones are in red. From left to right there are the distributions associated to the ECAL layers from the internal to the external one.

a dense material lose their energy (up to 100 GeV or higher) primarily through ionization and δ-rays. These processes account for energy losses of typically only 1-2 MeV $g^{-1}cm^{2}$ along the muon trajectory. The energy losses of electrons at energies above 100 MeV are dominated by radiative processes due to the Coulomb interaction with the electric fields produced by the atomic nuclei of the medium. The radiated photons (with energy >5-10 MeV) may create an electron-positron pair; these particles may in turn lose energy radiating photons and, continuing with this multiplication mechanisms, the result is the development of an e.m. shower. However, at lower energies ionization processes and radiative processes are in competition as the main energy loss mechanism for electrons, and also photons are more likely to undergo to different interactions (Compton or photoelectric interactions). As the shower develops, the average energy of the particles in the shower decreases, other processes start dominating the energy loss mechanisms of electrons, positrons and photons and no further multiplication in the shower takes place [46].

To identify whether an electron or muon caused the signals in the ECAL, it is taken into account that these particles deposit energy differently in each plane as they pass through the calorimeter: the energy deposit for electrons is expected to be greater in the plane of first interaction, while, muons are expected to lose energy almost uniformly in all layers [39]. The input variables chosen for this analysis are ten: five of them correspond to the visible energy of a cluster deposited in each layer of the calorimeter (in total there are 5 layers); while, the other five variables

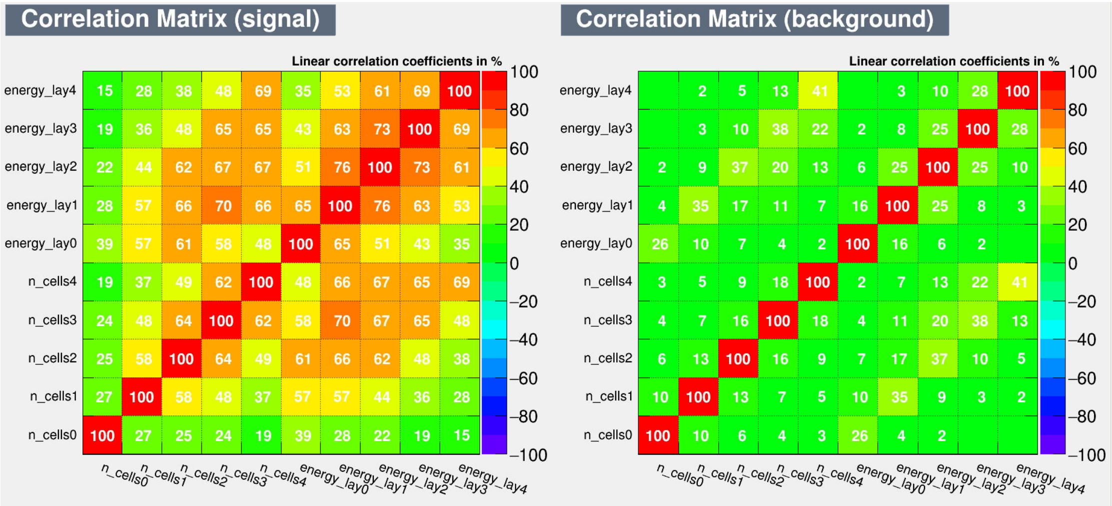

Correlation Matrix (signal)

Linear correlation coefficients in %

	n_cells0	n_cells1	n_cells2	n_cells3	n_cells4	energy_lay0	energy_lay1	energy_lay2	energy_lay3	energy_lay4
energy_lay4	15	28	38	48	69	35	53	61	69	100
energy_lay3	19	36	48	65	65	43	63	73	100	69
energy_lay2	22	44	62	67	67	51	76	100	73	61
energy_lay1	28	57	66	70	66	65	100	76	63	53
energy_lay0	39	57	61	58	48	100	65	51	43	35
n_cells4	19	37	49	62	100	48	66	67	65	69
n_cells3	24	48	64	100	62	58	70	67	65	48
n_cells2	25	58	100	64	49	61	66	62	48	38
n_cells1	27	100	58	48	37	57	57	44	36	28
n_cells0	100	27	25	24	19	39	28	22	19	15

Correlation Matrix (background)

Linear correlation coefficients in %

	n_cells0	n_cells1	n_cells2	n_cells3	n_cells4	energy_lay0	energy_lay1	energy_lay2	energy_lay3	energy_lay4
energy_lay4		2	5	13	41		3	10	28	100
energy_lay3		3	10	38	22	2	8	25	100	28
energy_lay2	2	9	37	20	13	6	25	100	25	10
energy_lay1	4	35	17	11	7	16	100	25	8	3
energy_lay0	26	10	7	4	2	100	16	6	2	
n_cells4	3	5	9	18	100	2	7	13	22	41
n_cells3	4	7	16	100	18	4	11	20	38	13
n_cells2	6	13	100	16	9	7	17	37	10	5
n_cells1	10	100	13	7	5	10	35	9	3	2
n_cells0	100	10	6	4	3	26	4	2		

Figure 4.9: Correlation matrices for signal (electrons) on the left and background (muons) on the right.

correspond to the number of cells of a cluster fired in each ECAL layer. These variables allow to have information about the longitudinal and lateral development of the cluster and may allow to discriminate between electron and muon events.

The input variables distributions are reported in figure 4.8. The signal distributions are in blue, the background ones are in red. In figure 4.9 the correlation matrices for signal and background are also reported.

A preliminary cut is applied on the dataset, in order to select events with just one cluster reconstructed; therefore, the whole signal dataset is characterized by 139954 events of which 69977 are used fo the training. The background dataset is formed by 161904 events of which 80952 are used for the training.

In figure 4.10 the signal and background distributions for the trained classifiers are reported.

Once the classification methods are trained and validated, the Receiver Operating Characteristic plot (ROC curve) is produced: it shows the background (muons) rejection (false positive rate) against the signal (electrons) efficiency (true positive rate). It can be used to compare the performances of the different classifiers in order to select the optimal method. As shown in figure 4.11, all the classifiers have optimal performances, and since the BDT and the NN are outstanding, both will be used in the subsequent steps of the analysis. Indeed, the area under the ROC curve is 1.000 for the MLP and BDT, and 0.990 for Fisher.

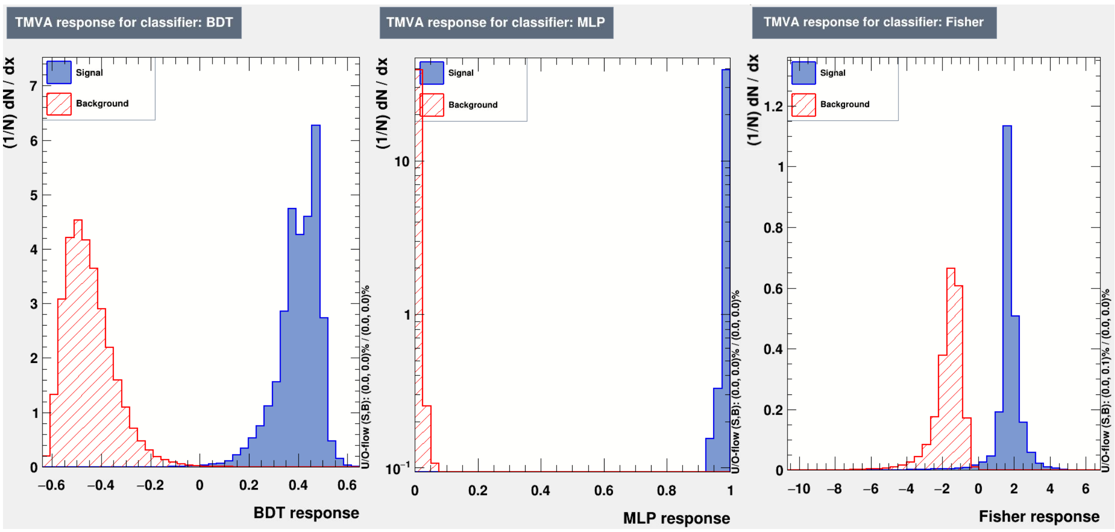

Figure 4.10: Signal and background distributions for the three classifiers: the Fisher method (left), the MLP (center) and the BDT (right). The MLP response is in logaritmic scale.

4.3.2 Application to neutrino interactions

Although the results of the classificaton methods are very good with the dedicated particle guns, their performance is tested with simulated neutrino interactions in the SAND detector. This requires the production of a neutrino events sample and a dedicated algorithm running on the MC truth able to select reconstructed clusters originated by electrons or muons. This algorithm represents a challenging step because of the overlap of hits from different tracks which makes it hard to clearly associate a single parent to some clusters. The trained models used to classify cluster events are taken from the previous study with the dedicated guns.

This work focuses on a preliminary study of the calorimeter capabilities to discriminate, as a stand-alone detector, between eletrons and muons produced in neutrino events considering the case of a neutrino beam in FHC mode. To this purpose two files are produced: one contains $5 \cdot 10^4$ ν_μ events for the dominant component of the beam and the other contains $5 \cdot 10^4$ ν_e events, due to a contamination of the beam, used to study e.m. showers (and eventually muon tracks from decays of secondaries). Therefore, ν_μ and ν_e events have been separately generated, digitized and reconstructed following the simulation and reconstruction chain described in sections 4.1 and 4.2. Then, these events are examined by a back-tracing algorithm that exploiting the MC truth selects clusters associated to an electron or a muon entering the ECAL.

For the application of the classificators, the events will be properly weighted

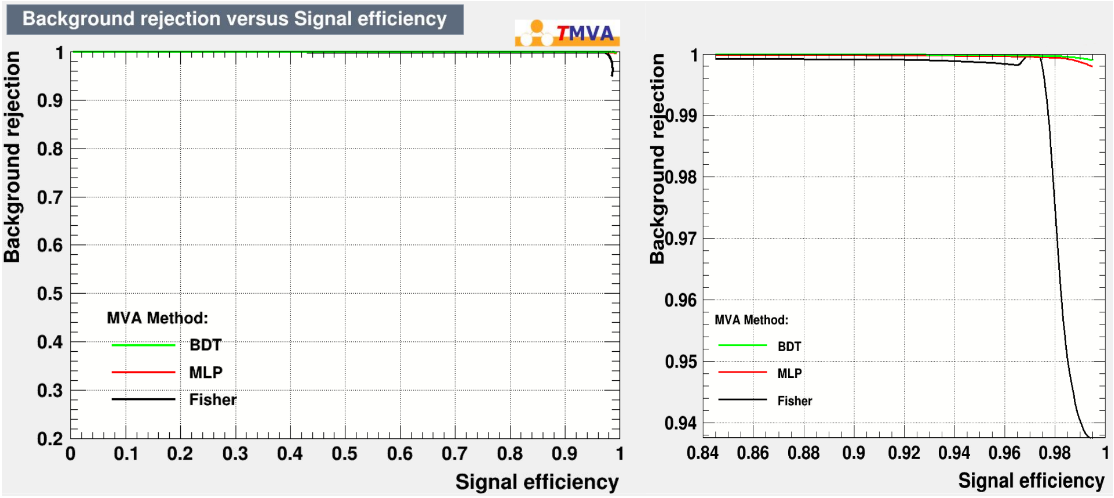

Figure 4.11: ROC curves of the Fisher classifier (black), the MLP (red) and BDT (green). A zoom of the upper right part of the ROC curve is shown on the right.

to reproduce the expected proportion between ν_μ and ν_e event rates at SAND for a neutrino beam produced in FHC mode.

Back-tracing algorithm

The back-tracing algorithm is developed to analyze neutrino events in order to encode the Monte Carlo information to associate a track parent to the cluster required for the final evaluation of the classification performance in discriminating e.m. showers from muons.

The back-tracing algorithm is developed in C++ and the input is retrieved from the output of *edep-sim*, the digitization, the reconstruction based on MC and the reconstruction performed by the new clustering algorithm.

In the following, the term "tracks" refers to the track elements reconstructed by the STT reconstruction algorithm described in section 4.1.2; while, "trajectory" refers to the true MC path of a particle propagating in the detector.

The back-tracing algorithm considers the clusters reconstructed by the new clustering algorithm (see section 4.2). The goal is to investigate whether a cluster may be associated to a single parent particle trajectory. This association would allow to identify the parent particle of the cluster and retrieve the particle energy related to the last hit in the STT before interacting in the calorimeter. Firstly, according to the data structure mentioned in section 4.1.1, the list of all the hits associated to each cluster is obtained by analyzing the photo-signals produced on each side of the cells belonging to the cluster. At this step, as many trajectories are considered as the hits associated to the clusters. Then, knowing the hits indices, the trajectories' IDs of the particles that produced the hits are obtained from the output of *edep-sim*. Using MC information, it's possible to know the parent trajectory ID for each particle simulated in the event. Therefore, from the list of trajectories, those that have a direct or distant ancestor that is already in the list are removed. Subsequently, a scan-back is performed on the points of the trajectories not discarded and for each point a geometric check is done to see if it is located within the ECAL. The purpose is to verify if a particle comes from outside the calorimeter or it has been originated inside it. If the trajectory is found to come from outside, the information regarding the particle and the last point, before it enters the ECAL, are associated to the cluster under examination. Thus, the cluster properties and the further information about the parent particles, if any found, are recorded in a *Cluster_kloe_algo* object. Notice that more than one particle or none can be identified to be a parent of the cluster that comes from outside the ECAL. Moreover, for each cluster additional quantities are computed and recorded in the *Cluster_kloe_algo* object: the visible energy deposited and the number of cells fired, for each ECAL layer.

New structures have been created for the output.
A *Cluster_kloe_algo* is defined by:

- the position and time coordinates of the cluster centroid;
- the cluster energy;
- the direction vector (described by the three Cartesian coordinates);
- the position variances;
- the number of the cluster parent particles that come from outside the ECAL;
- the set of parent *Particle* objects;

A *Particle* is characterized by:

- the ID of the trajectory;
- the ID of the parent particle trajectory;
- the name of the particle;
- the pdg code of the particle;
- the initial momentum of the particle;
- the last point, if found, before the particle enters the ECAL (defined by its position, the particle momentum and the information about the process occurred);

- a flag indicating if the particle comes from outside the calorimeter.

The output is saved in a ROOT tree. In a branch, *kloe_algo_clusters*, the sets of *Cluster_kloe_algo* objects are hold. Moreover, for each event some flags are saved, these indicate if the event has to be discarded or not for the analysis. One flag denotes if no hits have been produced in the ECAL during the event; another one specifies if the number of points of a trajectory exceedes buffer limit (in this case the event is rejected too); and the last flag is used to check if the cluster position is reconstructed inside the ECAL.

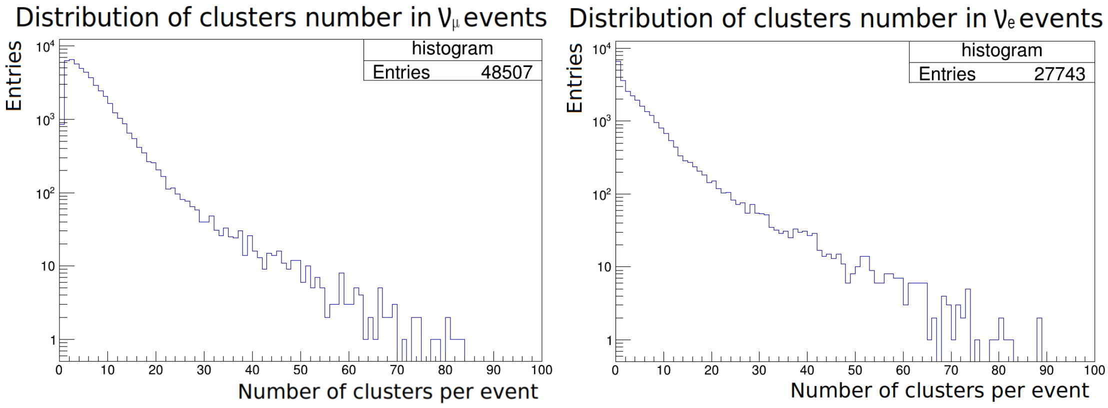

(a) (b)

Figure 4.12: Distributions of the number of reconstructed clusters in ν_μ events (a) and in ν_e events (b).

Classification performances

The $5 \cdot 10^5$ ν_μ and $5 \cdot 10^5$ ν_e events have been analyzed separately using the back-tracing algorithm. A first cut is applied in order to select those events in which a correct reconstruction of the trajectories has been performed: 490 ν_μ events out of $5 \cdot 10^5$ have been rejected. Then, another cut is applied to discard those events in which no interactions have occurred in the calorimeter. According to this cut, 48017 ν_μ events out of 49510 and 27743 ν_e events out of $5 \cdot 10^5$ have been kept ($\sim 45\%$ of ν_e events are found to have no hits in the ECAL). For these selected events, the total number of clusters reconstructed in the ECAL by the new clustering algorithm are computed. However, the 0.8 % of the total number of clusters in ν_μ events and the 2.2% of the total number of clusters in ν_e events are discarded given that the detection of uncorrelated signals on the same cell has caused an inconsistent result and the position of the cluster has been reconstructed outside the calorimeter. Therefore, the selected clusters result to be 296455 for the whole set of ν_μ events and 154794 for the ν_e ones. In figure 4.12 the distributions

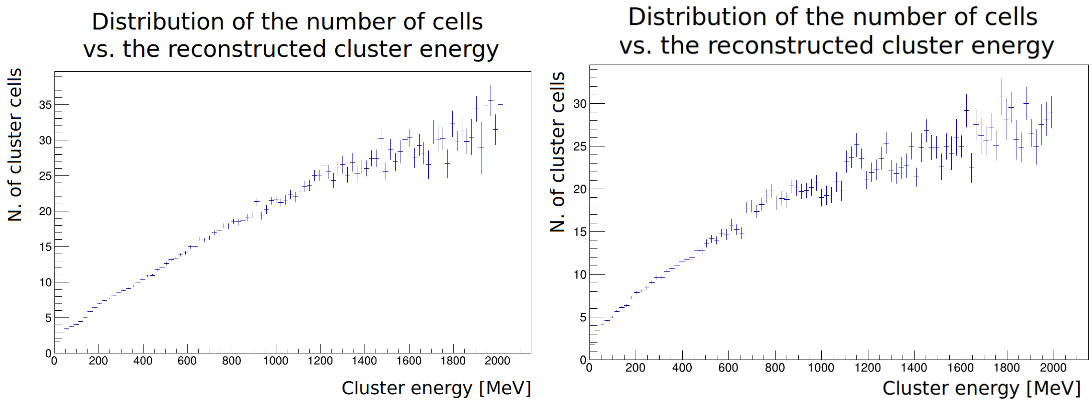

(a) (b)

Figure 4.13: Distributions of the average number of cluster cells as function of the reconstructed cluster energy. The distributions are shown up to $E < 2000$ MeV in order to better analyze the cut applied to remove low-energy clusters. Distributions are shown for clusters from ν_μ events (a) and from ν_e events (b).

of the number of clusters per event reconstructed in the calorimeter by the new clustering algorithm are reported.

Then, a further cut is applied to remove low-energy clusters: only clusters with reconstructed energy above 100 MeV are taken, leaving with 93874 clusters for ν_μ events and 21563 for the ν_e ones. As shown in figure 4.13, using this cut the clusters discarded have $\leq$4 cells in ν_μ events and $\leq$5 cells in ν_e events. In this case the information provided by the ECAL is not enough to efficiently discriminate e.m. shower from muons. It is considered that for these clusters a combined analysis with the tracking system is necessary to perform particle identification.

In figure 4.14 the distributions of the number of parent particles of a cluster are reported. It can be observed that with the developed MC association algorithm it is not possible to identify one parent particle for all the reconstructed clusters. Some of these are given by particles originated inside the ECAL and correspond to splitted parts of clusters for which no parent particle has been identified to come from outside the calorimeter. In other cases, clusters are found to have more parents and, therefore, they are given by the superposition of particle trajectories. Also, in the case of trajectory overlap, particle identification can exploit a combined analysis that integrates the information from the tracking device with the calorimeter information. The work of this thesis is limited to the study of the identification performances of the ECAL as a stand-alone detector in showers and muon tracks discrimination. For this reason, the analysis has been limited to clusters to which the back-tracing algorithm has associated a single parent particle using MC information. In the case of ν_μ events, clusters with a single parent parti-

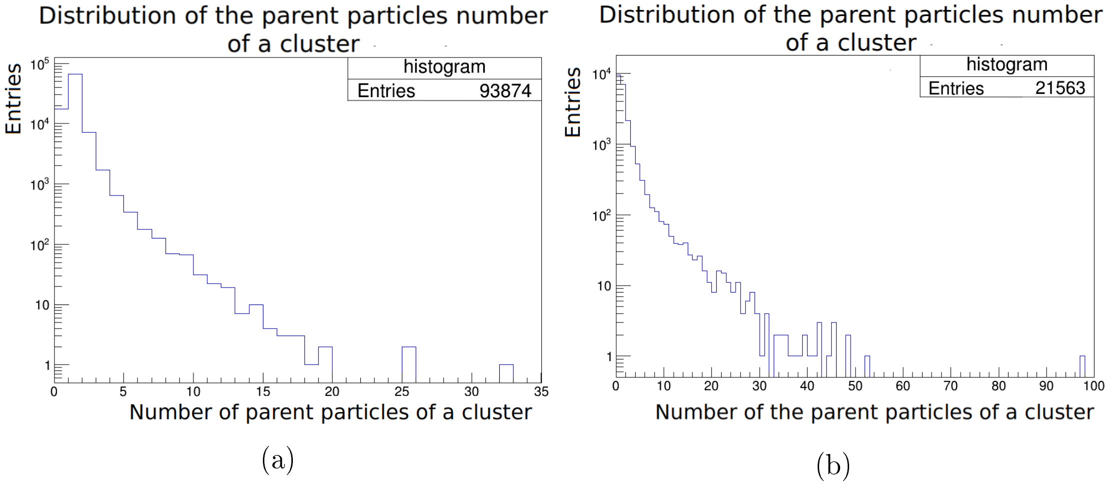

(a)

(b)

Figure 4.14: Distributions of the number of the particles which enter the ECAL and are identified by the back-tracing algorithm as the parents of a cluster. Distributions are shown for reconstructed clusters in ν_μ events (a) and in ν_e events (b).

cle are 66097, corresponding to the majority ($\sim 70\%$) of those reconstructed with more than 100 MeV. Instead, applying this cut in the case of ν_e events, 7083 clusters are selected and many are discrded due to the fact that the electron produced in a CC neutrino interaction has started the shower before entering the ECAL, and for the study of these clusters a combined analysis between the tracker and the calorimeter is needed.

The preparation of the cluster sample is completed by keeping those clusters which are found to be produced by an electron or a muon. Thus, from ν_μ events 33352 clusters produced by a muon and 1715 clusters by an electron are selected. From ν_e events 36 clusters are generated by a muon and 1545 by an electron. A weight w_{ν_μ} is associated to clusters from ν_μ events to account for those events rejected, with the first cut applied, because in the MC simulation the number of points of a trajectory has exceded the buffer limit. This weight corresponds to the fraction of events not discarded. Moreover, a weight w_{ν_e} is given to clusters obtained from ν_e events in order to account for the different probability of observing a ν_e interaction event with respect to a ν_μ one, considering that the analysis is based on the study of a ν_μ-dominated beam produced in FHC mode. This weight is given by the ratio between the expected ν_e CC+NC event rate integrated over the whole spectrum and the expected ν_μ CC+NC event rate integrated over the whole spectrum. The value obtained is equal to 0.015 ± 0.002. After assigning these weights to the clusters from ν_μ and ν_e events, the two cluster samples, kept separated until now, are joined together and used for the application of the trained classificators.

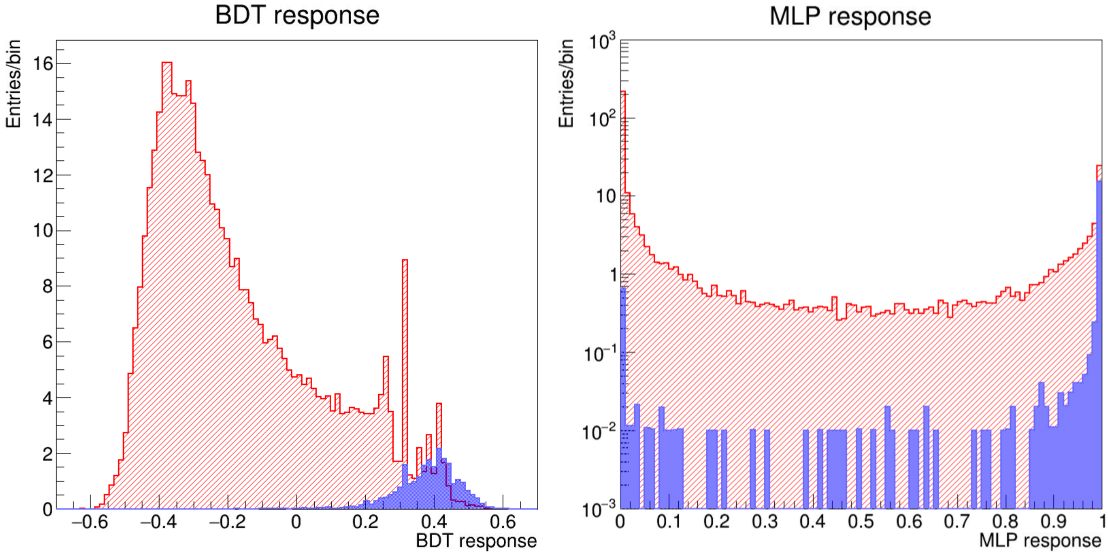

Figure 4.15: BDT (left) and MLP (right) responses. Signal (electrons) and background (muons) distributions for the clusters sample are shown in blue and red respectively. The MLP output is in logaritmic scale. The weight accounting for the contamination of ν_e interactions in a FHC ν_μ-dominated beam over the entire beam spectrum is applied to clusters obtained from ν_e events.

From the MVA application of the trained methods on the clusters sample, the BDT and MLP response distributions are obtained and reported in figure 4.15.

Furthermore, signal and background efficiencies, background rejection, purity and the signal efficiency times the signal purity versus the cut on the classifiers outputs for the expected numbers of signal (clusters associated to electrons) and background (clusters associated to muons) events are shown in figures 4.16 and 4.17.

The purity of a sample of clusters, selected as candidate clusters produced by an electron by requiring the classifier output to be $t > t_{cut}$, is computed as

$$\text{Purity} = \frac{S}{S+B} = \frac{\epsilon_s P(S)}{\epsilon_s P(S) + \epsilon_b P(B)} = \frac{\epsilon_s}{\epsilon_s + \epsilon_b \frac{P(B)}{P(S)}}, \tag{4.3.1}$$

where S and B are respectively the number of clusters produced by an electron and a muon such that the classifier output is $t > t_{cut}$, ϵ_s is the signal efficiency, ϵ_b is the background efficiency and $P(S)$ and $P(B)$ are the expected signal and background yields. For this computation, the ratio $P(B)/P(S)$ corresponds to the ratio between the muon sample and the electron sample obtained from ν_μ and ν_e

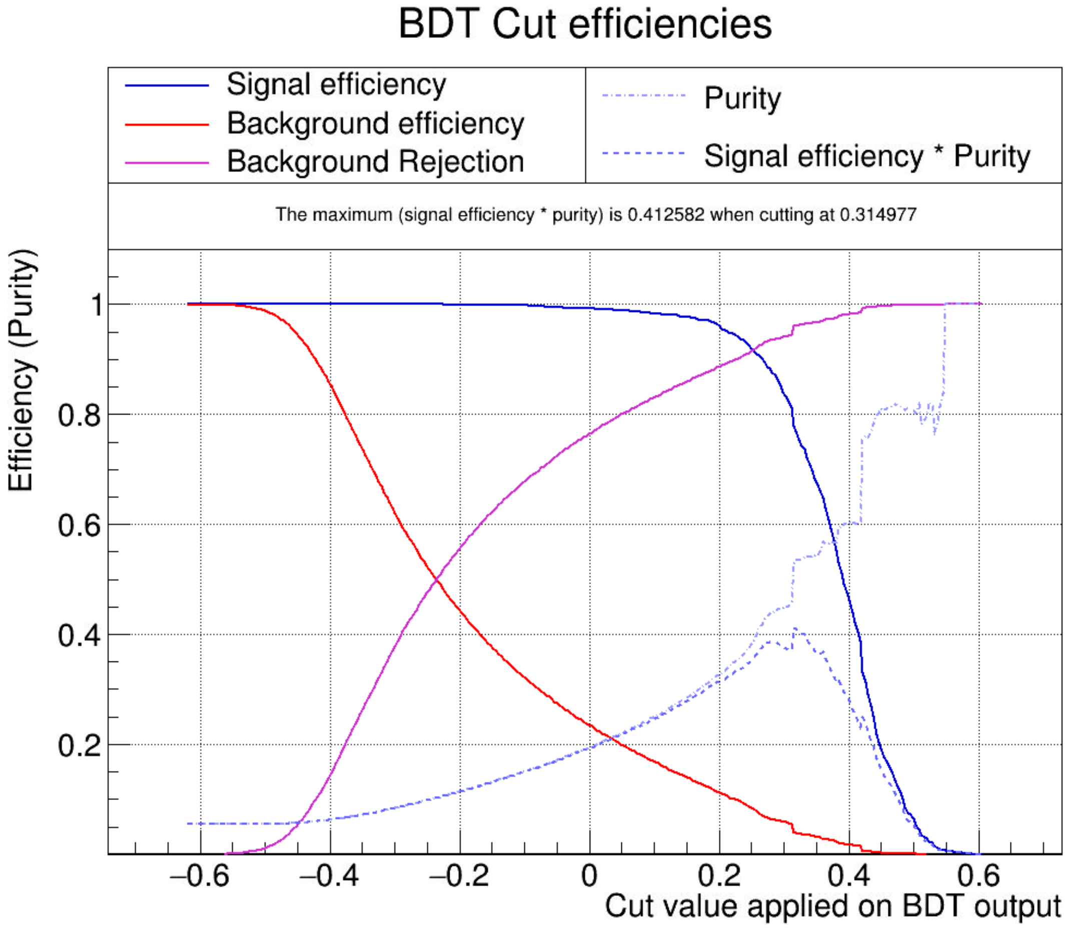

Figure 4.16: Signal (e.m. shower) and background (muon) efficiencies, background rejection, purity and the product of signal efficiency and purity versus the cut for the BDT output.

interaction events selected requiring that the cluster energy has to be > 100 MeV and the number of parent particles has to be equal to one. The ratio $P(B)/P(S)$ is computed as

$$P(B)/P(S) = \frac{n_\mu^{\nu_\mu}\, w_{\nu_\mu} + n_\mu^{\nu_e}\, w_{\nu_e}}{n_e^{\nu_\mu}\, w_{\nu_\mu} + n_e^{\nu_e}\, w_{\nu_e}}\,, \tag{4.3.2}$$

where $n_\mu^{\nu_\mu}$ is the average number of muon clusters in a selected ν_μ event, w_{ν_μ} is the weight that accounts for the ν_μ events discarded due to problems had during event simulation associated to the buffer limit of the number of trajectories points, $n_\mu^{\nu_e}$ is the average number of muon clusters in a ν_e event multiplied by the weight w_{ν_e} that accounts for the contamination of ν_e interactions in a FHC ν_μ-dominated beam, $n_e^{\nu_\mu}$ is the average number of electron clusters in a ν_μ event and $n_e^{\nu_e}$ is the

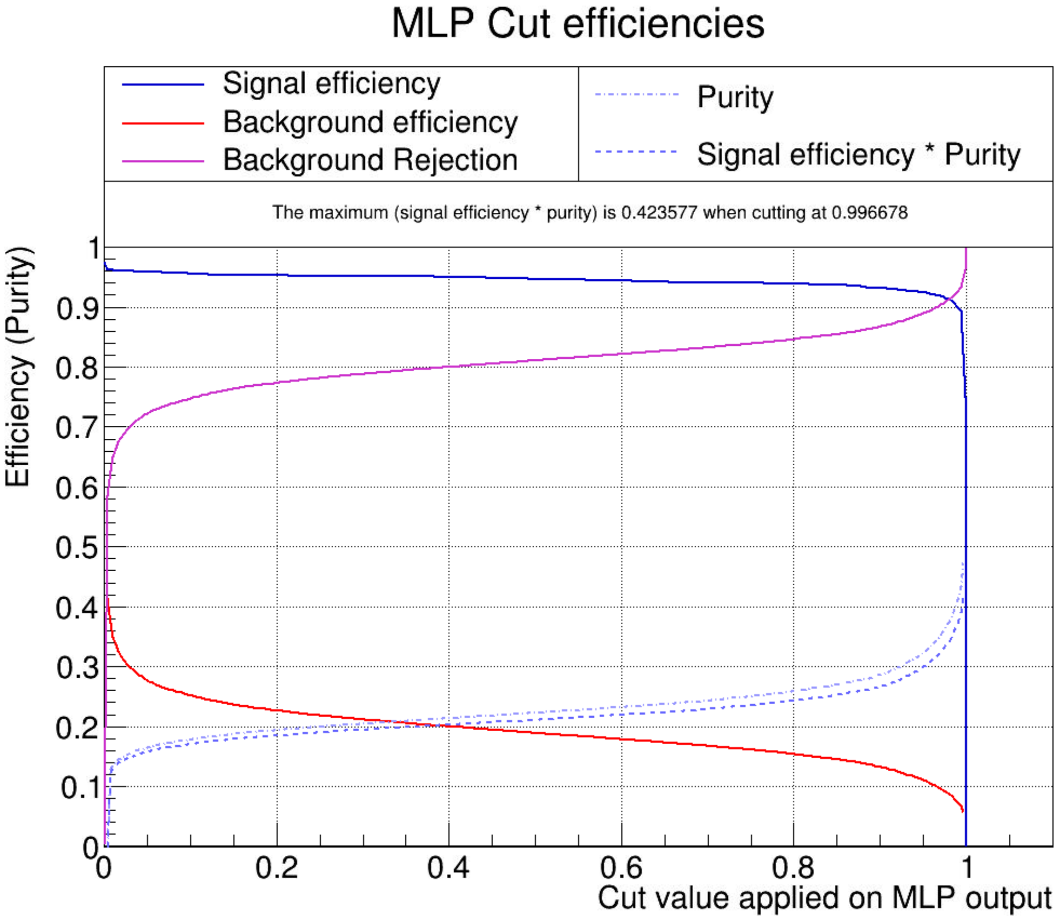

Figure 4.17: Signal (e.m. shower) and background (muon) efficiencies, background rejection, purity and the product of signal efficiency and purity versus the cut for the MLP output.

average number of electron clusters in a ν_e event.

The optimal cut is chosen to maximize the product between the signal efficiency and the purity. For the BDT, when cutting at 0.315 the signal efficiency times the purity is maximized at 0.413. The corresponding signal efficiency is equal to 0.779, the background rejection correspond to 0.960 and the purity is 0.530. For the MLP classificator, it is not possible to find an optimal cut since the figure of merit doesn't show a clear maximum. As it can be seen in figure 4.17, the signal efficiency times the purity increases as it approaches the right limit of the variable output range.

Moreover, the ROC curve (background rejection versus signal efficiency) obtained when cutting on the classifiers outputs is reported in figure 4.18.

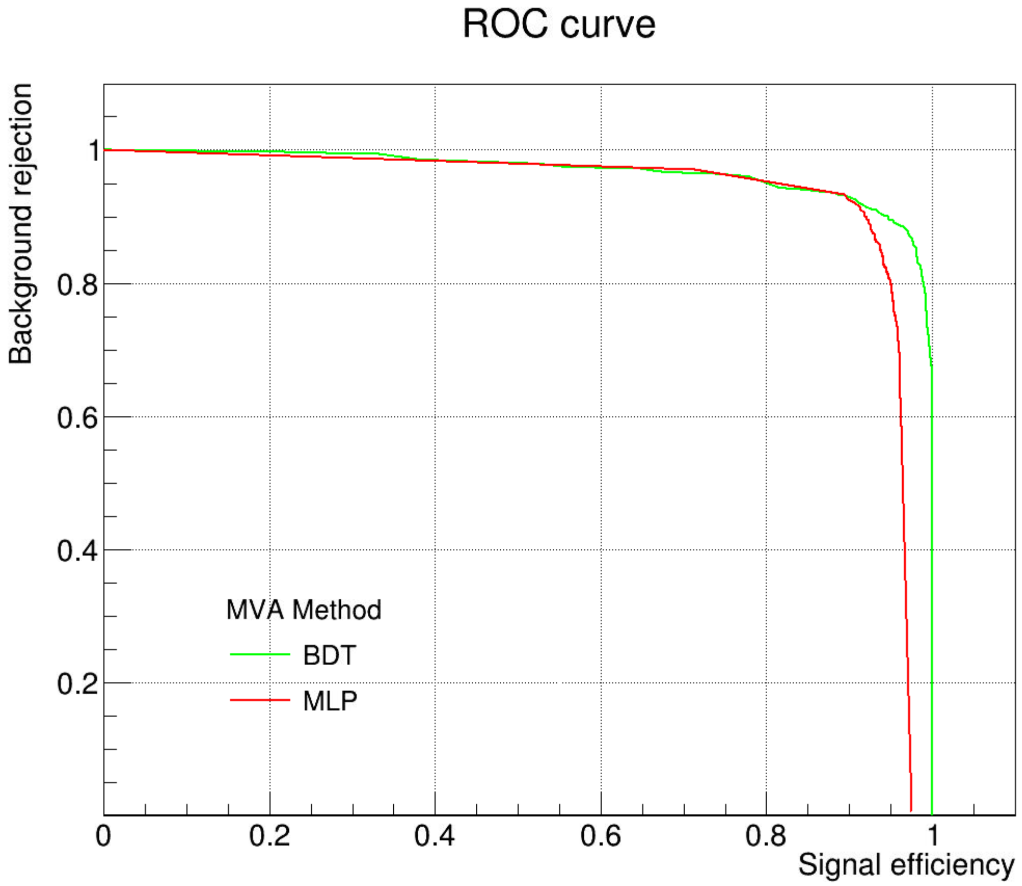

Figure 4.18: ROC curve from the clusters sample obtained by applying the cut on the BDT (green) and MLP (red) outputs.

Conclusions

An important step in our understanding of neutrino physics will be the next generation long baseline experiments, like the DUNE experiment. The main purpose of this experiment is to measure with unprecedented precision the parameters governing neutrino oscillations, with a particular priority to the CP violation term in the lepton sector and the determination of the neutrino mass ordering. The design of DUNE consists of (a) a high intensity wide-band (anti)neutrino beam, (b) a Near Detector (ND) complex located 575 m downstream the neutrino source, and (c) a deep underground Far Detector (FD) at Sanford Laboratory in South Dakota, at a distance of ∼1300 km. The ND complex will be optimized to measure and monitor the (anti)neutrino fluxes and to constrain systematic uncertainties. The design of the ND complex consists of three detectors: (a) a modular LArTPC, (b) a magnetized Gas Argon TPC, (c) the SAND detector which operates for a continuous on-axis beam monitoring. The SAND detector plays a crucial role for the ND since it is the only component permanently on-axis, while the TPCs can be moved sideways to perform off-axis measurements. The SAND design consists of a solenoidal superconducting magnet and of an electromagnetic calorimeter that will be reused from the KLOE experiment. The ECAL is a fine-grain sampling calorimeter, made of lead layers and scintillating fibers and it is composed of a barrel and two endcaps that provide a 4π coverage. In the SAND inner magnetic volume there will be a tracking system based on straw tube planes interleaved with thin carbon and hydrocarbon layers. In upstream position inside the magnetic volume an active LAr target is also conceived.

This work regards the study of the electromagnetic calorimeter performances, in particular an analysis on the ECAL capabilities to perform e.m. showers and muon tracks discrimination as a stand-alone detector is realized.

A new clustering algorithm has been developed to reconstruct the events in the calorimeter not exploiting at all Monte Carlo truth. This algorithm is inspired by the reconstruction procedure already implemented in the KLOE experiment, but it is renewed in order to be integrated and applied to the SAND simulation framework. The clustering algorithm is used to group neighboring hit cells into clusters, that will be associated to a particular physical object, a track or a shower.

Merging and splitting operations are also applied to improve the performances of the algorithm. The energy associated to a cluster is obtained by the sum of the energies given by all contributing cells. The position and time are determined as the energy weighted averages over the cells assigned to the cluster.

In this work, a preliminary validation of the clustering algorithm is operated by implementing a multivariate analysis realized to study the discrimination performances between e.m. showers and muon tracks using only calorimeter data. Three classifiers (a MLP, a BDT and one based on the Fisher method) are trained using a dedicated sample obtained by simulating particle guns of electrons and muons originated close to the ECAL. The classification is performed on the clusters produced by electrons, identified as signal, and by muons, defined as background. Very good performances are achieved by these classification methods. Indeed, the area under the ROC curve is 1.000 for the MLP and BDT, and 0.990 for Fisher.

Having outstanding performances, the trained BDT and MLP are used for the final step of this analysis in which events of neutrino interactions are simulated and the performances of the ECAL, as a stand-alone detector, for a discrimination between showering and muon particles are evaluated in terms of signal efficiency times purity. The case of ν_μ-dominated beam produced in FHC mode is considered for the simulation of neutrino events. Exploiting Monte Carlo truth, a sample of clusters produced in neutrino interaction events, by a muon or an e.m. shower, is selected. Some complications are given by the presence of many low-energy clusters composed by few cells and trajectories overlaps that make difficult to uniquely associate to each cluster the particle that have originated it. In these cases particle identification would benefit from a combined analysis with the tracking system. However, a preliminary study of neutrino events is performed on the clusters to which it is possible to identify a single particle that have produced them.

The trained classificators are applied on the selected cluster sample and signal efficiencies, background rejection and purity are computed as function of the cut applied on the classificators outputs. The product of signal efficiency times the signal purity is used as figure of merit for the evaluation of the optimal cut. For the MLP, it is not possible to find an optimal cut since the figure of merit doesn't show a clear maximum. For the BDT, the optimal cut is found at 0.315 according to a maximal value of the product between the signal efficiency and the purity equal to 0.413, the signal efficiency is 0.779, the background rejection is 0.960 and the purity is 0.530.

Different improvements can be performed to pursue the work of this thesis on particle identification performances of the SAND calorimeter. In fact, this analysis can be applied also to the case of antineutrino interaction events considering a $\overline{\nu}_\mu$-dominated beam produced in RHC mode. The study of the ECAL capabilities as a stand-alone detector can be extended, in terms of multi-class classification, to the identification of neutrons, pions, in addition to e.m. showers and muons. Moreover, particle identification will be widely improved by the realization of a classification algorithm which can combine data from all subdetectors (LAr target, STT tracker and calorimeter).

Bibliography

[1] B. Abi et al. *Deep Underground Neutrino Experiment (DUNE), Far Detector Technical Design Report, Volume I: Introduction to DUNE.* 2020. arXiv: `2002.02967 [physics.ins-det]`.

[2] M Adinolfi et al. *The KLOE electromagnetic calorimeter.* 2002.

[3] A. Abed Abud et al. *Deep Underground Neutrino Experiment (DUNE) Near Detector Conceptual Design Report.* 2021.

[4] M. Alam et al. "GENIE Production Release 2.10.0". In: (2015). arXiv: `1512.06882 [hep-ph]`.

[5] *Dune-ND-GGD.* URL: `https://github.com/gyang9/dunendggd`.

[6] *edep-sim : An Energy Deposition Simulation.* URL: `https://github.com/ClarkMcGrew/edep-sim`.

[7] M. Goldhaber, L. Grodzins, and A. W. Sunyar. *Helicity of Neutrinos.* Feb. 1958. DOI: `10.1103/PhysRev.109.1015`.

[8] C. Giunti and C. W. Kim. *Fundamentals of Neutrino Physics and Astrophysics.* Oxford University Press, 2007. ISBN: 978–0–19–850871–7 (Hbk).

[9] C. Quigg. *Gauge Theories of the Strong, Weak and Electromagnetic Interactions.* second edition. Princeton University Press, 2013. ISBN: 978-0-691-13548-9.

[10] S. Bilenky. *Introduction to the Physics of Massive and Mixed Neutrinos.* 2nd ed. Springer, 2010. DOI: `10.1007/978-3-642-14043-3`.

[11] The ALEPH Collaboration et al. *Precision electroweak measurements on the Z resonance.* May 2006. DOI: `10.1016/j.physrep.2005.12.006`.

[12] P.A. Zyla et al. *Review of Particle Physics.* Vol. 2020. 8. 2020, p. 083C01. DOI: `10.1093/ptep/ptaa104`.

[13] D. Vignaud. *The Gallium Solar Neutrino Experiment Gallex.* 1986.

[14] J. N. Abdurashitov et al. “Solar neutrino flux measurements by the Soviet-American gallium experiment (SAGE) for half the 22-year solar cycle”. In: *Journal of Experimental and Theoretical Physics* 95.2 (Aug. 2002). ISSN: 1090-6509. DOI: `10.1134/1.1506424`.

[15] G. Fantini et al. *The formalism of neutrino oscillations: an introduction.* 2020. eprint: `1802.05781` (hep-ph).

[16] F. Capozzi et al. “neutrino masses and mixings: Status of known and unknown 3 neutrino paramenters”. In: *Nuclear Physics B* 908 (2016). ISSN: 0550-3213.

[17] M. Wurm. “Measuring the Neutrino Mass Ordering in JUNO”. Sept. 2017.

[18] M. Spurio. *Probes of Multimessenger Astrophysics.* second edition. Springer, 2018.

[19] G. Giacomelli and A. Margiotta. *MACRO results on atmospheric neutrinos.* 2005. arXiv: `0504029 [hep-ex]`.

[20] M. Sanchez et al. “Measurement of the L/E distributions of atmospheric ν in Soudan 2 and their interpretation as neutrino oscillations”. In: *Physical Review D* 68.11 (Dec. 2003). ISSN: 1089-4918. DOI: `10.1103/physrevd.68.113004`.

[21] N. Agafonova and et al. “Discovery of τNeutrino Appearance in the CNGS Neutrino Beam with the OPERA Experiment”. In: *Physical Review Letters* 115.12 (Sept. 2015). ISSN: 1079-7114. DOI: `10.1103/physrevlett.115.121802`.

[22] D. G. Michael and et al. “Observation of Muon Neutrino Disappearance with the MINOS Detectors in the NuMI Neutrino Beam”. In: *Physical Review Letters* 97.19 (Nov. 2006). ISSN: 1079-7114. DOI: `10.1103/physrevlett.97.191801`.

[23] A. Gando et al. “Constraints on θ_{13} from a three-flavor oscillation analysis of reactor antineutrinos at KamLAND”. In: *Physical Review D* 83.5 (Mar. 2011). ISSN: 1550-2368. DOI: `10.1103/physrevd.83.052002`.

[24] Jun Cao and Kam-Biu Luk. “An overview of the Daya Bay reactor neutrino experiment”. In: *Nuclear Physics B* 908 (July 2016), pp. 62–73. ISSN: 0550-3213. DOI: `10.1016/j.nuclphysb.2016.04.034`.

[25] C. Adams et al. *The Long-Baseline Neutrino Experiment. Exploring Fundamental Symmetries of the Universe.* 2014. arXiv: `1307.7335 [hep-ex]`.

[26] B. Abi et al. *Deep Underground Neutrino Experiment (DUNE), Far Detector Technical Design Report, Volume II: DUNE Physics.* 2020. arXiv: `2002.03005 [hep-ex]`.

[27] G. Adamov et al. *A Proposal to Enhance the DUNE Near-Detector Complex.* May 14, 2021.

[28] V. Papadimitriou et al. *Design Of The LBNF Beamline.* 2017. arXiv: `1704.04471 [physics.acc-ph]`.

[29] DUNE Collaboration, B. Abi, et al. *Long-baseline neutrino oscillation physics potential of the DUNE experiment.* 2020. arXiv: `2006.16043 [hep-ex]`.

[30] GEANT4 Collaboration, S. Agostinelli, et al. *GEANT4–a simulation toolkit.* 2003. DOI: `10.1016/S0168-9002(03)01368-8`.

[31] *Proto-DUNE at CERN.* URL: `https://ep-news.web.cern.ch/proto-dune-cern-new-technologies-new-discoveries`.

[32] B. Abi and et al. "First results on ProtoDUNE-SP liquid argon time projection chamber performance from a beam test at the CERN Neutrino Platform". In: *Journal of Instrumentation* 15.12 (Dec. 2020). ISSN: 1748-0221. DOI: `10.1088/1748-0221/15/12/p12004`.

[33] B. Abi and et al. "Neutrino interaction classification with a convolutional neural network in the DUNE far detector". In: *Physical Review D* 102.9 (Nov. 2020). ISSN: 2470-0029. DOI: `10.1103/physrevd.102.092003`.

[34] Stephen P. Martin. "A Supersymmetry Primer". In: *Advanced Series on Directions in High Energy Physics* (July 1998). ISSN: 1793-1339. DOI: `10.1142/9789812839657_0001`.

[35] K. Abe et al. "Search for proton decay via $p \to \nu K^+$ using 260 kiloton·year data of Super-Kamiokande". In: *Physical Review D* 90.7 (Oct. 2014). ISSN: 1550-2368. DOI: `10.1103/physrevd.90.072005`.

[36] *KLOE-2.* URL: `http://w3.lnf.infn.it/ricerca/fisica-delle-particelle/kloe-2/`.

[37] J. Lee-Franzini, A. Antonelli, et al. *The KLOE electromagnetic calorimeter.* 1995.

[38] F. Ambrosino and et al. "Data handling, reconstruction, and simulation for the KLOE experiment". In: *Nuclear Instruments and Methods in Physics Research Section A: Accelerators, Spectrometers, Detectors and Associated Equipment* 534.3 (Dec. 2004), pp. 403–433. ISSN: 0168-9002. DOI: `10.1016/j.nima.2004.06.155`.

[39] F Ambrosino et al. *Calibration and performances of the KLOE calorimeter.* 2009.

[40] V. Pia, N. Mauri, and M. Pozzato. "Study of a novel VUV-imaging system in liquid argon for neutrino oscillation experiments". AMS Tesi di Laurea, 2019.

[41] S. N. Gninenko. “MiniBooNE Anomaly and Heavy Neutrino Decay”. In: *Physical Review Letters* 103.24 (Dec. 2009). ISSN: 1079-7114. DOI: `10.1103/physrevlett.103.241802`.

[42] *GEANT4-Physics Processes.* URL: `https://geant4-userdoc.web.cern.ch/UsersGuides/ForApplicationDeveloper/html/TrackingAndPhysics/physicsProcess.html#overview`.

[43] *Edep-sim output.* URL: `https://indico.cern.ch/event/687511/contributions/2822503/attachments/1574001/2484800/Edep-sim_output.pdf#search=edep-sim%20output`.

[44] *TMVA.* URL: `https://root.cern/manual/tmva/`.

[45] K. Albertsson et al. *TMVA 4 - Toolkit for Multivariate Data Analysis with ROOT: Users Guide.* Tech. rep. May 2020. arXiv: `physics/0703039`.

[46] M. Livan and R. Wigmans. *Calorimetry for Collider Physics, an Introduction.* 2019.